Declaration

Name: Athanasios Pappas

Email: thanasis_pappas@hotmail.com

Title of the Msc   Calibration of the numerical material behaviour of multi-leaf
Dissertation: stone masonry walls based on experimental results.

Supervisor: Prof. Maria Rosa Valluzzi

Co-supervisor: Ing. Bruno Q. Silva

Year: 2012

I hereby declare that all information in this document has been obtained and presented in accordance with academic rules and ethical conduct. I also declare that, as required by these rules and conduct, I have fully cited and referenced all material and results that are not original to this work.

I hereby declare that the MSc Consortium responsible for the Advanced Masters in Structural Analysis of Monuments and Historical Constructions is allowed to store and make available electronically the present MSc Dissertation.

University: University of Padova

Date: August 2011

Signature: Athanasios Pappas
                   _____

Erasmus Mundus Programme

ADVANCED MASTERS IN STRUCTURAL ANALYSIS OF MONUMENTS AND HISTORICAL CONSTRUCTIONS

Acknowledgments

I would like to express my appreciation for all the people who contributed and helped me during the length of this master program. I would like to thank the professor of the coordinating University of Minho, Paulo B. Lourenço as well as the professor of the University of Catalunya, Pere F. Roca, where I followed the courses and the professor of the University of Padova, Claudio Modena where I carried out my thesis. Special thanks also to my thesis supervisor professor Maria Rosa Valluzzi for the assistance and for trusting me to work with her. I could not omit the excellent and continuous collaboration, help and guidance that were offered to me by my co-supervisor Ing.Bruno Q. Silva for which I am really grateful.

I need to mention my appreciation for the Consortium scholarship, financed by the SAHC Consortium itself, which was given to me and helped me in my decision to follow the program.

I also need to thank my colleague and friend Ing. Evina Pigouni for the countless work hours that we spent together. Finally, I would like to thank all the colleagues and friends of the SAHC group, including the Omar group, whom it has been a real pleasure to meet and work with.

Athanasios Pappas

\

Erasmus Mundus Programme

ADVANCED MASTERS IN STRUCTURAL ANALYSIS OF MONUMENTS AND HISTORICAL CONSTRUCTIONS

Abstract

This research deals with the numerical simulation of stone masonry walls.

The numerical material behaviour of stone masonry is calibrated based on experimental results of simple compression tests on single-leaf and three-leaf stone masonry walls in original and injected condition (1:1 and 2:3 scale) using a non linear continuous damage model implemented in the software Cast3m (DM2S). The calibrated behaviour curves for the compression tests are then applied on the simulation of a shear-compression test in order to assess the viability of its direct application on the simulation of those structural elements when they are subjected to this type of action. The stone masonry walls are simulated considering an homogeneous isotropic material capable of taking into account the joint behaviour of stone, mortar and consolidation material and also the interaction between the internal and external leaves.

The obtained numerical material can reproduce the behaviour of the real stone masonry walls under monotonic and cyclic compression in a satisfactory way. Regarding the shear-compression test simulation, the direct application of the numerical curves resulted from the compression tests do not provide good results due to the variability of the properties of each type of walls. Thus, the numerical material curves had to be adjusted to fit the shear-compression test. This final adjustment provided a good fit on in terms of envelope (initial stiffness, maximum resistance and post peak behaviour) and also in terms of energy dissipation when the non linearity is not so high, presenting the model limitations in this field. The calibrated numerical material properties are intended to be used for structural analysis of real case studies like the San Domenico church of L'Aquila for which the finite element model has been created.

Erasmus Mundus Programme

ADVANCED MASTERS IN STRUCTURAL ANALYSIS OF MONUMENTS AND HISTORICAL CONSTRUCTIONS

ADVANCED MASTERS IN STRUCTURAL ANALYSIS OF MONUMENTS AND HISTORICAL CONSTRUCTIONS

Sommario

Questa tesi tratta della simulazione numerica di pannelli murari in pietra.

Dal punto di vista numerico, il comprtamento della muratura in pietra è stato calibrato sulla base di prove a compressione monoassiale su campioni a paramento singolo e tre paramenti, in condizioni originali e iniettate (scala 1:1 e 2:3) usando un modello di danno continuo implementato nel software Cast3m (DM2S). Le curve di comportamento calibrate per le prove a compressione sono state utilizzate per la simulazione delle prove a taglio-compressone, per valutare l'affilità della sua applicazione diretta nella simulazione di questa tipologia di elemento strutturale sottoposta a questo tipo di azione. La simulazione dei pannelli in muratura è stata effetuata considerando un materiale omogeneo e isotropo capace di tener conto del comportamento congiunto di pietra, malta, iniezione e le interazioni tra paramento interno ed esterno.

Il materiale numerico ottenuto dalle prove a compressione dei pannelli murari sottoposti a carico monotono e ciclico, è in grado di riprodurre in modo soddisfacente il comportamento delle pareti in muratura vera e propria. Per quanto riguarda la simulazione della prova a taglio-compressione, l'applicazione diretta delle curve numeriche derivanti dalla prova a compressione non fornisce buoni risultati a causa della variabilità di ogni tipo di parete; per questo motivo si è reso necessario adeguare le curve numeriche alla prova di taglio-compressione. Quest' ultima regolazione ha fornito buoni risultati in termini di inviluppo (rigidezza iniziale, resistenza massima e comportamento post-picco) e anche riguardo la dissipazione di energia nel caso in cui la non linearità presenti valori non elevati, situazione quest' ultima che rappresenta i limiti del modello in questo campo. Le proprietà del materiale numerico calibrato sono destinate ad essere utilizzate per l'analisi strutturale di casi studio reali, come quello della chiesa di San Domenic presso L'Aquila per il quale è stato creato questo modello ad elementi finiti.

viii

Contents

Introduction

One of the most common wall typologies appearing in old structures is the multi-leaf stone masonry ones which is subject of study of various research programs [Egermann (1993); Valluzzi *et al.* (2001); Vintzileou and Tassios (1995); Vintzileou and Miltiadou (2008)]. The strengthening technique of grout injection with compatible materials like hydraulic lime based grouts is considered to be one of the most efficient methods for repairing or strengthening structures of historical importance against earthquakes. For the study of the behaviour of three-leaf walls in unstrengthened and strengthened with grout injection conditions an experimental campaign started in 2010 by the University of Padova. Three-leaf stone masonry walls in 1:1 and 2:3 scale and single leaf walls in 1:1 scale were built according to the traditional building techniques and a number of them were strengthened using natural hydraulic lime-based grout. The experimental tests include monotonic and cyclic compression tests and cyclic shear-compression test.

The result of the experimental tests on the masonry walls are used for the calibration of finite element numerical models using the Cast3m software. For this scope, a continuous damage model is implemented. The procedure of numerical analysis of a material like the stone masonry with high anisotropy and complex inelastic behaviour is a demanding procedure. The stone masonry walls are simulated using a homogenous and isotropic material capable of taking into account the joint behaviour of stone, mortar and consolidation material, but also the internal and external leaves and giving numerical results close to experimentally obtained ones. The numerical behaviour of all the walls, unstrengthened, injected and single-leaf is calibrated both for the case of the monotonic and the cyclic compression test. A numerical calibration of the behaviour of an injected wall in 2:3 scale for a shear-compression test is also carried out.

The numerically calibrated composite material can find use in application on real structures built with similar stone masonry walls. Such a structure is the San Domenico church in L'Aquila (Abruzzo) which was damaged by the 9th of April 2009

1

intense earthquake. A numerical finite element model of the structure was created for this scope. The numerical model, after its calibration with the use of the results of previous non destructive and minimum destructive tests that are available, can be implemented for acquiring a better knowledge of the structural behaviour and pathologies of San Domenico church and for studying the effectiveness of future strengthening techniques.

Chapter 1

Survey on multi-leaf walls and grout injections

1.1 Introduction

Despite the fact that the stone multi-leaf masonry walls are very commonly appearing in old structures, their behaviour under vertical and horizontal load is quite complex and still under study. Numerous experimental campaigns have taken place trying to shed light on this domain [Tomaževic and Sheppard (1982); Egermann (1993); Valluzzi (2000); Valluzzi *et al.* (2001); Vintzileou and Tassios (1995); Vintzileou and Miltiadou (2008)] . Taking as granted the fact that masonry structures are quite vulnerable in case of earthquake, the study of an intervention technique able to strengthen them is necessary. This work mainly focuses on the grout injection technique which is often an object of investigations of various researchers.

1.2 Failure Modes of multi-leaf walls

The failure modes in multi-leaf masonry walls can be mainly categorised into failures due to the detachment of the leaves, the global or local overturning and the local expulsions of the material (Figure 1.1).

Figure 1.1: Failure modes of multi-leaf stone masonry walls [Modena *et al.* (2011)].

3

In the case of three-leaf walls, the inner core is confined by the external leaves, thus it will be able to reach higher values of compressive strength. On the contrary, the external leaves will fail in lower values comparing to the values of the tests on individual leaves. This takes place due to the horizontal load perpendicular to their plane that they receive due the expansion of the confined internal core [Egermann (1993), Vintzileou and Tassios (1995)]. Moreover, when the internal core yields, the already limited amount of the vertical load that it was carrying will be transferred to the stiffer elements which are the external leaves (Figure 1.2).
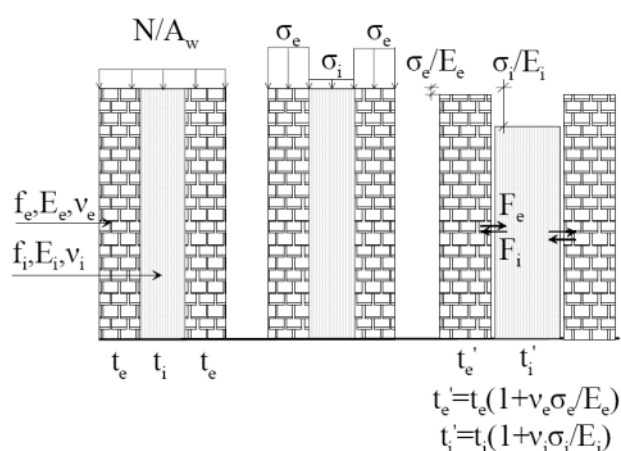

Figure 1.2: Stresses and deformations in three-leaf walls under compression, [Vintzileou (2007)].

 At the same moment, the contact and connection, if there are any, between the internal and external parts will be lost due to the tensile stresses vertical to this surface. The presence of grout, mortar or an interlocking between the stones of the different leaves would significantly help in order to increase the tensile capacity interface between the internal and external leaves. Finally, the external leaves, being separated and thus more slender, will appear an out of plain failure mode because of the buckling effect caused by the combination of high vertical load and horizontal out of plain load [Vintzileou (2007)]. The crack pattern has mainly vertical direction, both in the façade and in the cross section. Nevertheless, the crack width magnitude at the cross section, where it is obvious the separation of the core for the external layers, is substantially higher than the one of the façade (Figure 1.3). The route of the cracks, via the stones or not, depends from the characteristic strength of the stones and the

4

mortar. In the usual unrepaired or repaired with compatible materials traditional masonry walls the mortar has smaller compressive strength than the stones. Hence, the cracks will mainly pass through the mortar matrix and not via the stone blocks.
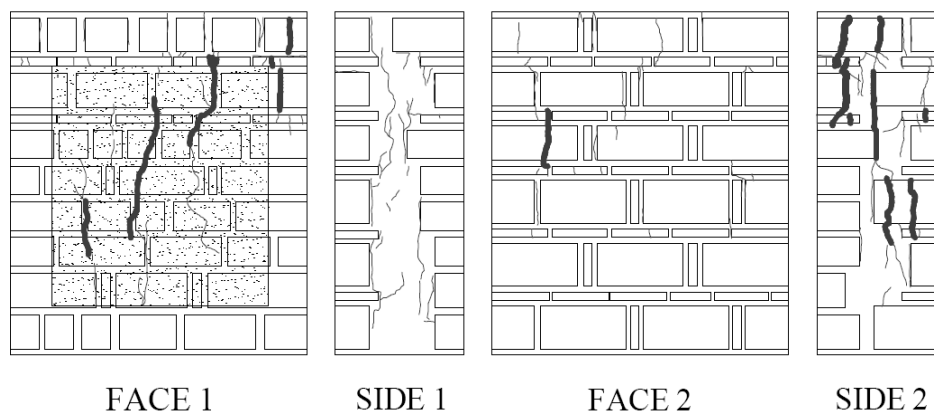

FACE 1   SIDE 1   FACE 2   SIDE 2

Figure 1.3: Crack pattern caused by compression in three-leaf walls. [Vintzileou and Miltiadou *(2008)*]

1.3 Grout injection technique

This intervention technique can be described as the injection of grout in the voids of the masonry with a further aim to consolidate it and to improve the structural behaviour both under vertical and horizontal forces. The technique can be used when there is a certain amount of voids in the wall sufficiently connected among them in order the grout to be able to insert and to bind the materials together. An ideal area of application is the multi-leaf masonry walls where it is necessary to connect the different layers of the wall and which also appear high amount of voids in the dry rubble stones inner core.

The choice of the grout depends on the masonry typology and on its material properties. The grout material must be chemically compatible with the masonry materials in order to avoid degradation by chemical reactions [Vintzileou (2007)]. Also, mechanical compatibility must be guaranteed choosing a grout with compressive strength, Poisson's ratio and Young's modulus of elasticity close to the ones of the original mortar. The compressive strength must be high enough in order the application to be effective but not higher than the strength of the stone blocks for

5

avoiding the crack propagation through the stones. It is necessary the grout to have sufficient penetrability and viscosity in order to be able to insert the connected voids and to remain there consolidating the wall [Valluzzi (2001)]. Another parameter to be eliminated is the solubility to the water which would set the risk of washing off with the rain. Also, the grout needs to keep a constant volume not influenced by the humidity and to be permeable from the humidity in order water not to be concentrated in the masonry body during the thermal cycles. The grouts can be divided into organic and inorganic.

Organic

The organic grouts are consisted of synthetic resins (e.g. epoxy resins) and they can achieve very high values of strength and also minimum setting time. Their fluidity can also reach high levels and their adherence to the original materials is considered to be very effective [Valluzzi (2001)]. Nevertheless, the mechanical behaviour of the organic resins is not compatible with the traditional material met on masonry walls making them not the best choice for injection of traditional structures.

Inorganic

The inorganic grouts consist of water, aggregates (only if it is necessary to reduce the shrinkage is case of large holes) and usually lime or cement or a combination of the two. Additives like retardants, accelerators, fluidifiers or aeratics can be added. Such function can have the silica fume, the pozzolan, the clay and the crushed pottery. The correct amount of water and the correct size of the aggregates are of great importance in order to achieve sufficient fluidity and penetrability for filling the voids and the cracks of the wall [Collepardi (1991)]. Special care must be taken for the use of cement based grout in masonry with historical importance. Potential chemical reactions between the cement and the original materials may take place causing irreversible deterioration. Moreover, the cement, being a material with high strength and stiffness, can modify the stiffness and the overall behaviour of the original structure in a negative way. Also, the strength of the cement grouts is usually higher than the strength of the stones causing the already mentioned above problem of crack propagation via the stones.

6

1.4 Application method

The stages of the intervention include the preparation of the surface of the wall, the drilling and flushing, the injection and the final cleaning restorating the initial appearance.

The preparation of the surface of the wall is done with the removal of the old and not sufficiently connected to the stone bodies mortar. This can be achieved either with water in low or high pressure or with hot air between 150-200 C under a pressure between 5-10atm [Valluzzi (2000)]. It has to be paid attention though on the temperature and pressure in order not to cause damage on the structure. Once cleaned, the joints and the cracks had to be repointed with new mortar compatible with the original in terms of mechanical, chemical and appearance properties. The sealing will help in order the injected grout to travel through the voids and not to be expelled directly for the joints and the cracks.

The next phase includes the drilling of the walls which takes place within the mortar joints and it is recommended to have a slight downward angle. The density of the holes depends on the characteristics of the wall with a value between 2-10 holes/m^2 to be recommended. The holes can be done based on a triangular of rectangular grid. By assuming a circular diffusion effect of the injections though, the triangular grid gives better results in terms of grout diffusion for the same density of holes as it is presented in the Figure 1.4. Holes can be also opened on the other side of the wall if it not causing problems to existing artistic decorations. Those will work as control points to check if the application of the techniques is proceeding correctly. The depth of the drilling must necessarily reach at least the inner core which is the area with the most voids and the diameter of the holes is recommended to be between 20-60mm depending on the type of the stone masonry. Various materials of injection nozzles like metallic or synthetic are available. The more preferable are the synthetic transparent materials which allow a better control of the work.
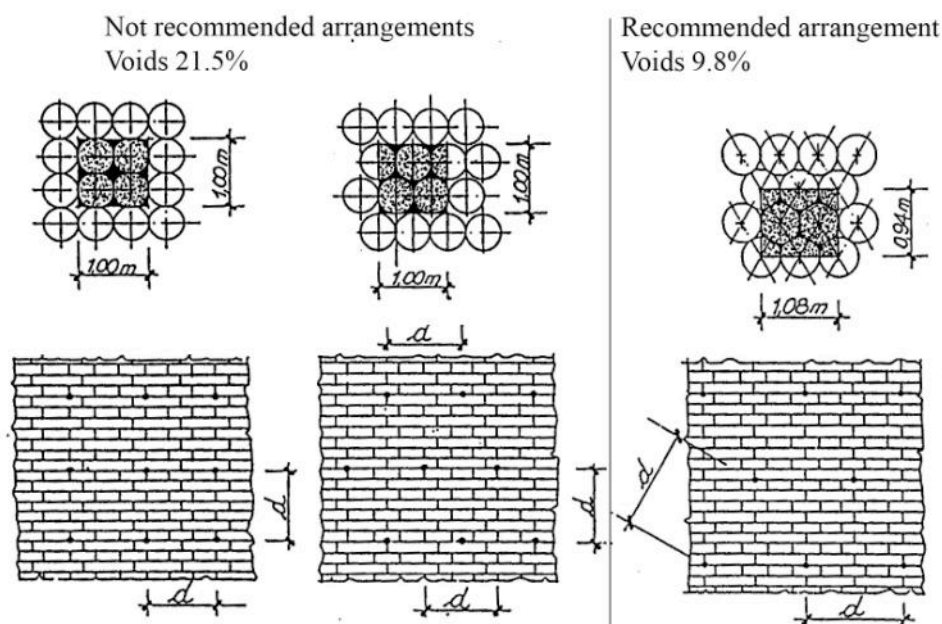
Figure 1.4: Possible arrangements of the holes, [Caleca and de Vecchi (1990)].

It is advisable the internal surfaces to be cleaned of the dust by flushing with water. The procedure must start from the top using as little water as necessary for the flushing of the dust and the debris downward. In this way the masonry will be both clean and saturated with water. The saturation will eliminate the risk of the fast absorption of the water by the dry materials of the wall which would cause a segregation of the grout negative effects on its characteristics. Nevertheless, the possible triggering of deterioration phenomena due to the water diffusion should be taken into account if this kind of preparation is used.

There are three different techniques of injection and the choice of the appropriate depends on the special characteristics of the structure.

Gravity injections

The grout is injected from holes on the top of the wall. It finds use only in severely deteriorated walls with high amount of voids. The grout is filling the voids only due to the gravity forces (Figure 1.5a). The process can be checked with the appropriate control holes.

<u>Depressive injections</u>

This method is used only with very fluid grouts like the synthetic resins and for very small size of cracks. The injections take place in the inferior holes and sub pressure is created to the holes above forcing the grout to move upward. The technique is applicable mainly in smaller substructures mainly removable like architectural elements or statues.

<u>Pressure injections</u>

The technique is applied with the use of the appropriate equipment for the creation of pressure. The grout is inserted from the holes on the bottom starting laterally and moving towards the center of the wall. Then one row of holes is injected the process continues in the row above (Figure 1.5a). The injection at one hole stops when the grouts exits from another injection hole or a control point. Every nozzle needs to be sealed after its use. The pressure is desirable to remain constant during the operation if this is possible. For week walls like the three-leaf walls it is recommended the pressure to be kept lower than 1atm.
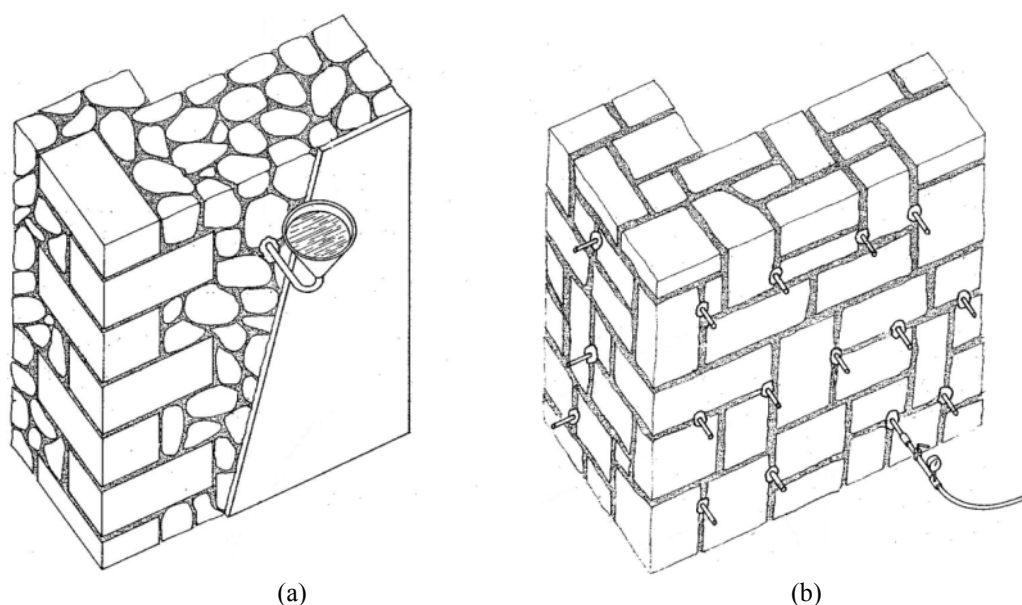

(a)   (b)
Figure 1.5: Injection techniques: (a) gravity injection; (b) pressure injection, [Caleca and de Vecchi (1990)].

9

1.5 Literature survey on compression test campaigns of multi-leaf walls

This literature survey is focused on compression tests of mainly tree-leaf and two-leaf masonry stone walls. Since the decade of 1980 various such campaigns were realised usually as a part of broader experimental tests, including also shear-compression tests and dynamic tests. The scope of the researches was to obtain a better understanding of the behaviour of multi-leaf masonry walls and also to study the effects of possible intervention techniques like the grout injection method. A brief description of some of the most important experimental campaigns is following. The experimental results of each campaign are presented in the Table 1.1.

A. [Tomaževič and Sheppard (1982)]: Walls corresponding to different traditional building techniques were built. After the testing of in their original state, they were injected with a mixture of 90% Portland cement and 10% pozzolan then they were tested again. The Young's modulus and the strength values before the injection vary between the different building techniques. Generally, the compressive strength increased significantly in all of the cases. Nevertheless, the effects of the injections vary depending on the building technique but in all of the cases the strengthening is noticeable.

B. [Tomaževič (1992)]: In this project, two layered rubble stone masonry walls with thick joints were tested. Although this campaign was mainly focused on shear tests, two panels were strengthened and tested under compressive load. The compressive strength is appeared to be highly increased if it compared to the unstrengthened walls of Tomaževič and Sheppard [(1982)].

C. [Egermann (1991), (1993)]: In an attempt for obtaining better understanding of the three-leaf walls under compression, multiple small size unstrengthened wall specimens were created and tested. In the specimens the thickness and the stiffness of the outer skins were held constant while for the infill different thickness and stiffness values were tested. The results were used for the identification of the two main phases

10

in the behaviour of the walls. The first phase includes linearly increasing with the vertical load deformations and the zero damages to the outer skins. In the second phase the bond between the leaves is lost and the lateral deformations start to increase. The yielding of the infill introduces horizontal loading to the outer skins causing their bending in combination with the high compressive load. Finally, the fact that the infill appears cracks testifies that it partially contributes in the resistance of the multi-leaf wall.

D. [Bettio *et al.* (1993), Modena and Bettio (1994)]: In this experimental campaign double-leaf walls were tested for the deeper understanding of the effects of grouting and jacketing strengthening techniques. Different types of grout mainly based on hydraulic lime and quicklime or hydraulic lime containing crushed bricks and cementitious additives. At the last ones it was paid attention in order not to contain sulphates which can cause chemical reactions with the other constituents of the walls. Different values of the Young's modulus of elasticity were calculated depending of different stress levels. In the Table 1.1 are presented the values corresponding to stress values between 25% and 50% of the maximum compressive strength. Finally it was fount the grout injection was possible to increase around 50% the compressive strength.

E. [Vintzileou and Tassios (1995)]: The a group of six (1-6) three-leaf walls were loaded in compression until the ultimate load capacity and then unloaded in order to be strengthened with injections and to be tested later. There were used two different grouts of portland-type cement. Two more (7-8) walls were strengthened with the same technique but without any former application of load. The purpose of this was to compare between the effects of preventive intervention and a post damage intervention. Moreover, two of the walls (1,3) had transversal leaves in order to guarantee a better interlocking. The experiments concluded the increase of the strength may vary between 50% and 200%. The reason for the enhanced behaviour was the homogenization between the leaves because of the injections. Moreover, the cement grout injections made the wall much more stiffer leading to failure strains of lower values than the original ones.

G. [Valluzzi (2000), Valluzi et al. (2001)]: In this extended experimental work, three-leaf walls were tested for strengthening with grout injections, repointing and transversal tying. Only lime-based grout and admixtures were used in order to have a compatible to the traditional materials strengthening technique which would guarantee the durability of the intervention. It was found that the maximum resistance in compression due to the injection strengthening could increase even more than 50% and also the brittle mechanism of failure was avoided. Moreover, due to the compatibility of the lime-based grout, the modulus of elasticity remained at the same order of magnitude but with significant reduction of the transversal dilatation. The improvement of the overall behaviour is even higher if the injections are companied with repointing and transversal tying.

H. [Toumbakari (2002)]: This work contains the strengthening of three-leaf panels with injections with different types of reduced Portland cement grouts. Most of the walls were tested before and after the intervention. It was found that the main factor that affects the behaviour of the wall was the shear bond between the grout and the blocks of masonry. For those types of grouts, the transversal connection was lost at a level between 60-70% of the ultimate strength.

I. [Oliveira and Lourenço (2006)]: Multiple three-leaf walls were tested before and after the strengthening with the combination of lime-based grout injection and GFRP transversal bars anchored along the thickness of the external leaves. The compression experiments have shown that the ultimate strength in compression was increased by an average of 71%. In addition to this, the intervention altered the typical failure mode for three-leaf walls from out-of-plane movement of the external leaves to the formation of a dominant vertical cracking pattern. This was possible because of the GFRP bars which resulted in the creation of horizontal plastic hinges.

G. [Binda *et al.* (2006)]: The purpose of this extended experimental campaign was to analyse the knowledge into the load-transfer mechanisms in multi-leaf masonry walls. A total of 12 three-leaf walls were built with two different types of collar joint and two types of stones. The results have shown a difference in the failure mode between the two different types of collars with the straight one to exhibit a more brittle failure.

K. [Vintzileou and Miltiadou-Fezans (2008)]: It is studied the effect of ternary grouts (mixes of cement, pozzolan and hydrated lime) and hydraulic lime-based grouts in the compression strengths of three-leaf walls especially with the existence of frescoes and mosaics which have to be protected. It was found that due to the homogenization that the grouts with lower or no cement content offer, despite their lower mechanical properties comparing to the high cement ones, the overall behaviour of the wall is significantly enhanced. Moreover, hydraulic lime-based mortars avoid the risk of compatibility problems and efflorescence effects which is possible to take place when cement is inserted in the historical construction.

L. [Corradi *et al.* (2008)]: This project contains in-situ experiments taken place in three-leaf wall cut from load bearing walls with the use of diamond wires in order the samples to be kept intact. The walls were tested before and after the grout injection and deep repointing strengthening. The aim of the compression tests was to find the Young's modulus of elasticity and the Poisson's ratio, therefore the failure point under compression was intentionally not reached.

M. [Galasco *et al.* (2009a)]: The researchers focused on the study of double-leaf masonry panels. The compression tests on the walls was a part of the broader work which also included dynamic tests of masonry structures on shaking table. The compression load was imposed in subsequent cycles with increasing load levels.

N. [Mazzon (2010)]: This campaign included experiments on shaking table of two stone masonry structures in 2:3 scale along with tests of stand-alone masonry panels. The scaled structures were not tested until the collapse, thus it was possible some selected parts to be cut and to be tested in quasi-static experiments. Some of those specimens were tested in the damaged condition and some were repaired with lime-based grout injection. Intact masonry panels were also injected trying to captive in this way the behaviour of the strengthened walls without any appearance of damage prior to the intervention. In the Table 1.1 are presented the results of the repaired and the strengthened specimens for the compression tests.

Table 1.1: Results of compression tests of previous experimental campaigns

Project	Panel	Dimensions [cm]	Layers [cm]	$f_{wc,0}$ [N/mm^2]	$f_{wc,s}$ [N/mm^2]	$E_{wc,0}$ [N/mm^2]	$E_{wc,s}$ [N/mm^2]	$\varepsilon_{wc,0}$ [‰]	$\varepsilon_{wc,s}$ [‰]
A. [Tomaževiè and Sheppard (1982)]	CAT I	100x60x265		0.46		220			
		100x60x265		0.54	0.95	190	840		
	CAT II	100x50x247		0.31	2.00		2020		
		102x50x260		0.37	2.00	310	2780		
		100x51x254		0.37	2.02	480	3035		
	CAT III	105x57x255		0.82	2.77	3550	3275		
		105x55x250		0.71	1.90	2870	2610		
	CAT IV	125x55x182			3.69		8070		
		125x55x182			4.33		9230		
		125x55x182			3.86		5670		
		125x55x182			3.72		7860		
B. [Tomaževiè (1992)]	V-1	100x50x120			4.24		2100		
	V-2	100x50x120			3.18		1385		
C. [Egermann (1991), (1993)]	1F3	31x15x40	3/9/3	1.8		1480			
	2F3	31x15x40	3/9/3	2.1		2860			
	3F3	31x15x40	3/9/3	2.4		2160			
	1K3	31x15x40	3/9/3	2					
	2K3	31x15x40	3/9/3	2.3					
	3K3	31x15x40	3/9/3	2.7					
	1B3	31x15x40	3/9/3	7		20100			
	2B3	31x15x40	3/9/3	11		20090			
	3B3	31x15x40	3/9/3	10.7		18590			
	1Z1	31x9x40	3/9/3	3		4770			
	2Z1	31x9x40	3/9/3	3.9		4810			
	1Z3	31x9x40	3/9/3	2.4		3420			
	2Z3	31x9x40	3/9/3	3.4		4810			
	1Z5	31x9x40	3/15/3	1.8		4740			
	2Z5	31x9x40	3/15/3	3.1		4810			
	1F1	31x9x40	3/3/3	3.5		2640			
	2F3	31x9x40	3/9/3	2.4		2640			
	3F5	31x9x40	3/15/3	2.2		2640			
D. [Bettio *et al.* (1993), Modena and Bettio (1994)]	C1 A				1.5		130		
	C1 B						190		
	C2 A				1.46		240		
	C2 B						500		
	C3 A				1.71		430		
	C3 B						450		
	C4 A			0.7	1.15	60	370		
	C4 B					240	500		
E. [Vintzileou and Tassios (1995)]	1	60x40x120	18/14/18	2.1	3.1	7000	6250	1.04	0.6
	2	60x40x120	18/14/18	1.3		2706			
	3	60x40x120	18/14/18	2.4	4.3	5000	5971	1.41	1.1
	4	60x40x120	18/14/18	1.6		4442		0.8	
	5	60x40x120	18/14/18	1.7	4.2	5670	7778	2.8	1.2
	6	60x40x120	18/14/18	1.35	4.05	5625	8438	0.58	1
	7	60x40x120	18/14/18		3.7		15413		0.9
	8	60x40x120	18/14/18		3		3333		0.9

Project	Panel	Dimensions [cm]	Layers [cm]	$f_{wc,0}$ [N/mm^2]	$f_{wc,s}$ [N/mm^2]	$E_{wc,0}$ [N/mm^2]	$E_{wc,s}$ [N/mm^2]	$\varepsilon_{wc,0}$ [‰]	$\varepsilon_{wc,s}$ [‰]
	1			2.02		3670			
	2			2.1	3.3	4400	4500		
	3			2.6	3.5	5900	4000		
	4			2.7	3.3	5200	1900		
	5I1	80x50x180	18/14/18	1.45	2.49	2390	2273	3.63	7.26
	6I1	80x50x180	18/14/18	1.95	2.49	2029	3093	4.57	5.71
	13I1	80x50x180	18/14/18		2.54		3992		9.91
	14I1R	80x50x181	18/14/18		2.14		1620		8.21
	1I2	80x50x180	18/14/18	1.97	2.57	1450	3449		6.25
	8I2	80x50x180	18/14/18	1.91	1.82	1559	2367	6.21	7.2
	16I2	80x50x180	18/14/18		2.48		1223	6.22	10.7
	SC1	60x40x120	13/14/13	2.02	3.25	720	1622	1.42	3.55
	SC2	60x40x120	13/14/13	2.09	3.36	1139	1559	1.65	2.33
	SC3	60x40x120	13/14/13	2.65	3.51	1375	1188	1.73	2.45
	SC4	60x40x120	13/14/13	2.71	3.29	1443	1015	2.11	3.49
	1W1	60x30x110	10/10/10	2.4					
	1W2	60x30x110	10/10/10	1.7					
	2W1	60x30x110	10/10/10	1.4					
	2W2	60x30x110	10/10/10	-	3.3				
	2W3	60x30x110	10/10/10	-	2..6				
	2W4	60x30x110	10/10/10		3.5				
	NS3	31x51x79	17/17/17	5.8		1770		3.5	
	SS33	31x51x79	17/17/17	>15.1		2940		>5.2	
	NO3	31x51x79	17/17/17	6.4		2085		4.1	
	SO3	31x51x79	17/17/17	>15.1		2725		>5.9	
	1	100x45x120	19/12/14	1.82	3	1000	1200		1.76
	2	100x45x120	19/12/14	1.74	3.75	1440	1550	1.6	2.5
	3								

16

Chapter 2

Numerical analysis methods

2.1 Introduction

The importance of studying numerically the masonry structures behaviour is significant, especially if it is taken into account the high risk of human loses or damages to architectural heritage monuments caused by seismic events. The masonry, having high anisotropy and complex inelastic behaviour, makes its numerical analysis a very demanding procedure. Various techniques are available, such as the limit analysis, the discrete element and the finite element method. The ability of a method to reproduce the structure's behaviour in a realistic way and the computational demands can be important criteria for the choice of the method. Different approaches are available, with linear elastic or non-linear inelastic material behaviour, at a micro or macro level, with different ways of damage representation and with damage models obeying different constitutive laws.

2.2 Kinematic model analysis

According to [Giuffrè (1991)], the estimation of the seismic vulnerability can be achieved via the decomposition into rigid blocks and then the application of kinematic limit analysis. The decomposed rigid blocks are called macro-elements, that present homogeneous constructive characteristics and behaviour. The division into macro-elements can be done taking into consideration the mutual bond between the different structural parts of the building, the geometrical borders, the poor connections, the different restraints or materials, the existing cracks or the potentially expected cracks

17

[Giuffrè (1993a,b); Doglioni (1994)] (Figure 2.1). The primary hypotheses of the kinematic approach, which were later revised, were: (1) the absence of sliding between the blocks, (2) the absence of tension and (3) the infinite compressive strength of the masonry. In order to estimate the overall seismic behaviour of a structure it is necessary to proceed to all the possible analyses considering all the possibly expected kinematic failure mechanisms. Via the extent data survey of past earthquakes it was possible to be formed damage abacuses of the most expected failure mechanisms for the different types of structures. Every kinematic mechanism will give a different coefficient α_o which is the mean response acceleration for the ultimate limit state for which the equilibrium is lost. Through the classification of all the mechanisms it is possible to identify the most critical ones which will be the mechanisms leading to failure with the lowest values of the seismic coefficient α_o. The kinematic mechanisms can be divided into out-of-plane and in-plane mechanisms with the first ones usually characterized by lower coefficients α_o [Borri *et al.* (1999a,b)].
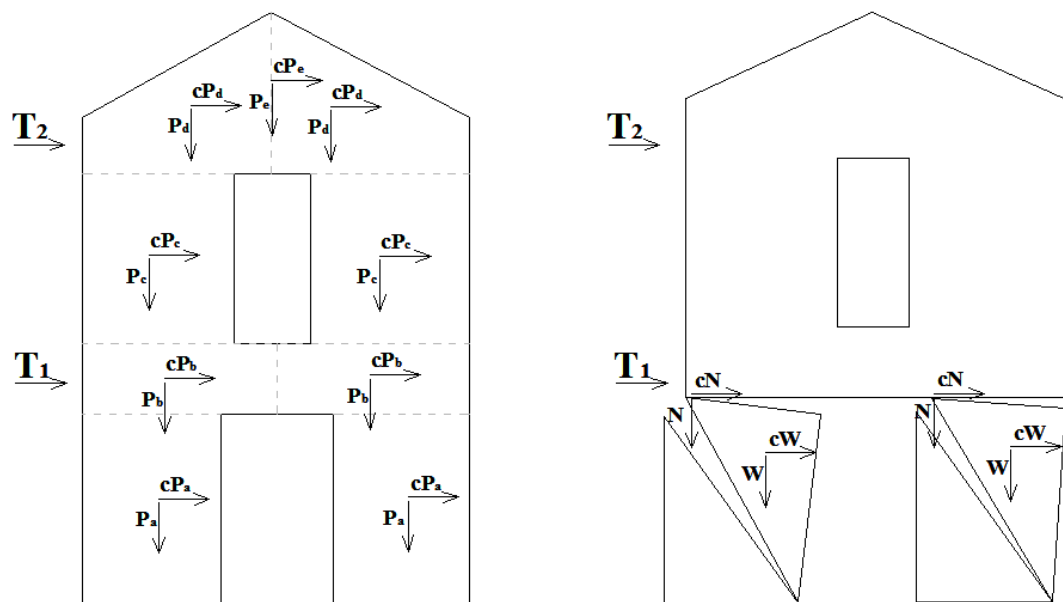
Figure 2.1: Formation of a kinematic chain for in-plain behaviour.

Out-of-plane mechanisms

They are activated by the horizontal seismic actions perpendicular to the plane of the macro-elements and can result in the partial or total overturning of the walls [Giuffrè (1993a)]. This type of damage can also be defined as "First Damage Mode". The main damage patterns connected to the out-of-plane mechanisms are the shedding of the external leaf and the vertical cracks at the corners of the structure (Figure 2.2). Those vertical cracks testify the creation of a hinge in that area. Into the equilibrium equation, stabilizing forces other than the self weight can also be possible forces by the connections, diaphragms or ties.

In-plane mechanisms

They are the results of horizontal forces imposed in the plane of the macro-elements. The cracks connected to such mechanisms appear to be inclined and they often have an "X" pattern. The occured triangular sections produced by the shear cracks can appear high instability leading to collapse by the activation of out-of-plane mechanisms. The damage type caused by in-plane mechanisms can be called "Second Mode of Damage". Forces by the connections, the diaphragms or strengthening ties can be taken into account as stabilizing factors in the kinematic limit analysis.
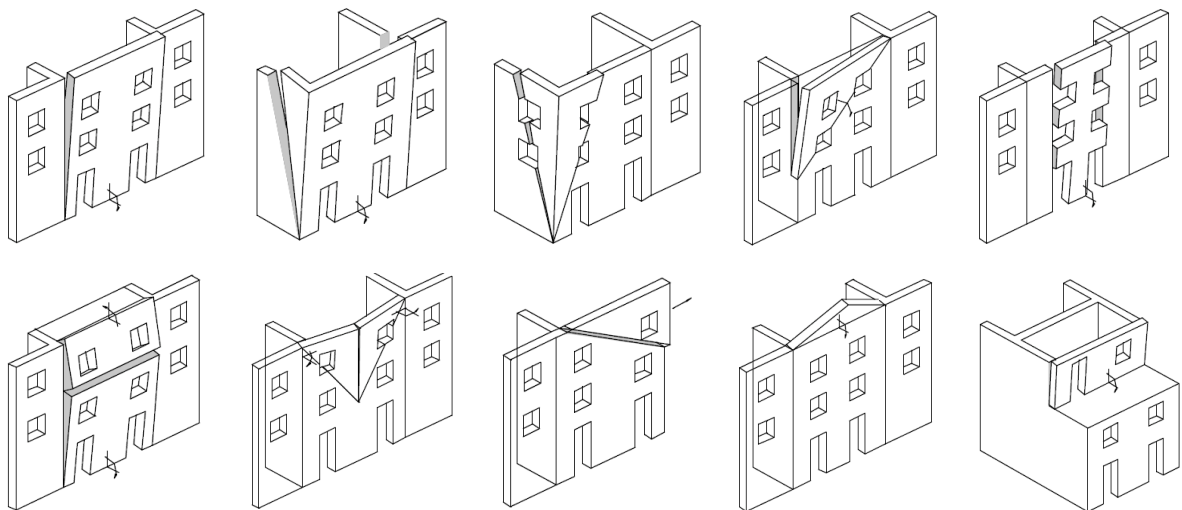
Figure 2.2: Out of plane failure mechanisms for buildings embedded within urban texture, based on [D'Ayala and Speranza, (2002a)].

Since the first proposal of Giuffrè, the technique of the limit analysis has upgraded. [Fajhar (1999); Lagomarsino *et al.* (2003); Lagomarsino (2006)] managed to combine the limit analysis with the capacity spectrum method leading to a method that was able to be used for the designing of strengthening and to be adopted by seismic codes (Italian codes OPCM 3274 [PCM (2003)]; OPCM 341/2005 [PCM (2005)]).

Moreover, the kinematic analysis method has undergone some improvements by [Ochsendorf (2002), De Luca *et al.* (2004), Block (2005), Block *et al.* (2006), Roca *et al.* (2007)] based on graphic oriented techniques using both kinematic and static approaches. The new revised hypotheses of the method are: (1) the absence of tension between the blocks, (2) the shear failure at the joints is perfectly plastic, (3) the creation of a hinge at a point is the result of a compressive load independent from the rotation.

Another interesting approach has been done by [Orduña and Lourenço (2003, 2005a, 2005b)] who proposed a complete limit analysis formulation for rigid block assemblages for 3D problems. In their model which takes into account non-associative flow rules, the no-tension frictional interfaces are adopted along with a proposal for the torsion failure mode (Figure 2.3). The high validation and correlation between the numerical and experimental results justify the importance of this method.
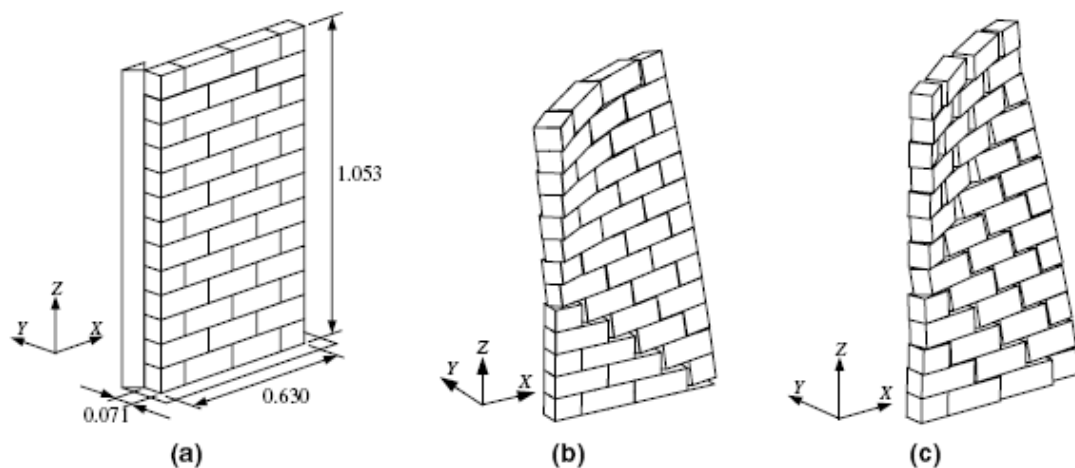
Figure 2.3: Out-of-plane loaded wall, supported at one edge: (a) model; (b) FEM failure mechanism (α=0.210); limit analysis failure mechanism (α=2.160) [Orduña and Lourenço (2005b)].

20

2.3 Structural element method

In the structural element models the exact geometry of the structure is represented by individual macro-elements such as walls, columns, beams, arches and vaults with the homogeneous material behaviour. The macro-elements can by two-dimensional or one-dimensional. In both of the cases there is the assumption of no tensile strength while for the two-dimensional elements the stiffness changes with the compression strength. The no tensile strength assumption can be simulated either with the change of the geometry of the elements to remove the tensile strain area [D'Asdia *et al.* (1994)] or by modifying the strength inside the two-dimensional macro-element [Braga *et al.* (1990)]. Due to the regard of linear elastic behaviour, the maximum compression stress must be controlled. The model fails when the limit equilibrium is achieved of when the maximum compression strength is reached.

It is possible to develop one-dimensional elements able to appear shear deformation. There are two main categories regarding how the stiffness elements which can be either varying [Braga *et al.* (1982)] or constant with elastic behaviour followed by plastic deformation [Tomaževic (1978)]. In the last approach, Tomaževic proposed the POR model for the analysis of masonry structures. This model simulates the structure giving it a 'box behaviour' emphasizing in this way in the in-plane mechanisms. The main limitations of the POR model were (a) the consideration of the masonry walls as the only deformation and collapse elements ignoring the possible failure of the interaction strut elements; (b) the assumption of the shear failure with diagonal cracking as the only possible failure mechanism of the masonry walls ignoring the out-of-plane and sliding failure. The second limitation was easily overcome with the introduction of additional failure criteria [Tomaževic and Weiss (1990)] but the first one was not able to be addressed due to the fundamental idea of the method regarding the assembled model.

A method proposed by Brencich *et al.* [(1998)] modeling the entire walls and panels as two nodes macro-elements, reducing in this way the considerably the computational demands. As a result of the reduced computational cost, this method

21

can be used for the modeling of cyclic behaviour and dynamic analysis. With the use of those elements, the overturning, the damage and the shear mechanisms can be taken into account.
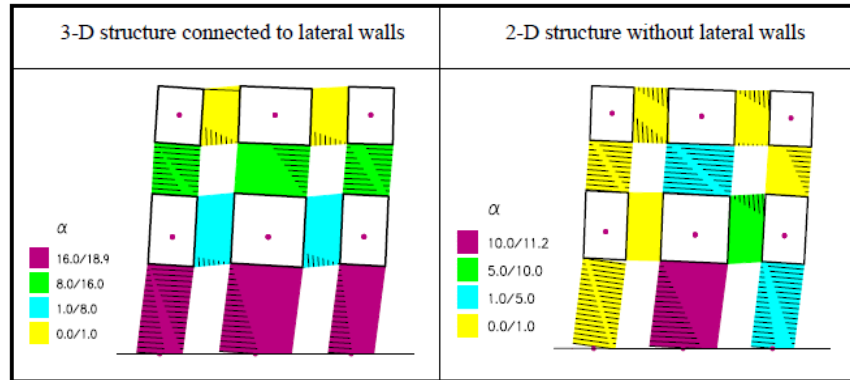

Figure 2.4: Analysis with macro-blocks of a façade wall, damage distribution under monotonic loading at the end of the monotonic load history, [Brencich *et al.* (1998)].

Molins *et al.* [(1998)] proposed a method for the analysis of masonry skeletal structures using a set of partial models for the description of the non-linear response of masonry taking into account the cracking in tension and the yielding or crushing in compression. The method was was enhanced by Roca *et al.* [(2005)] in order to analyse 3D systems including masonry load bearing walls.

Figure 2.5: Multiple system: (a) Wire representation of the inner and exterior walls; (b) representation of floor slabs as a grillage; (c) predicted deformed shape amplified for the earthquake acting transverse to the main façade, [Roca *et al.* (2005)].

Another model, called rigid body spring model, has been developed by Casolo and Peña [(2007)] for in-plane dynamic analysis of masonry walls. The model consists of quadrilateral rigid elements connected among them with two normal springs and one shear spring at each side. Hysteretic laws were implemented for the axial and shear deformation between the elements.

22

2.4 Discrete element method

The discrete element method (DEM) developed by [Cundall (1971)] in the field of rock mechanics and then it was extended to the masonry buildings. According to Cundall, the "discrete element" applies to a computer approach only if (1) it allows finite displacement and rotations of discrete blocks, including the complete detachment and (2) it can recognize new contacts between blocks automatically as the analysis progresses. The discrete element method is based on discontinuous mechanics and treats the model as discontinuous materials with the ability to appear progressive failure, crack propagation and large displacements and rotations between the blocks. By the automatic rounding of the corners of the blocks it is possible to avoid the problem of the interlocking blocks which makes the DEM a very convenient tool for analysis of masonry structures [Azevedo (2001)].

There is the possibility to simulate the blocks as (1) "deformable blocks", using a mesh of finite elements within the block or as (2) "rigid blocks". The contact surface between two blocks can be simulated as (1) "soft contact" in which the tension is obtained from the relative displacement between the blocks and a slight overlap in compression is allowed [Pagnoni (1994); Lemos (1998); Sincraian (2001)], as (2) "rigid contact" [Jean (1995); Acary *et al.* (1998)] or (3) using springs on the surface blocks [Casolo (2004a)].

Various types of structures can be studied with different types of discrete element analysis in 2D or 3D. There is the possibility for static or dynamic analysis of load bearing walls [Pagnoni (1994), Baggio and Trovalusci (1995), stone bridges [Lemos (1995); Bicanic *et al.* (2001); Alexandris *et al.* (2008)] (Figure 2.7), columns and architraves [Papastamatiou and Psycharis (1993); Psycharis *et al.* (2003)] (Figure 2.6) or arch and pillar [Pagnoni (1994); Pagnoni and Vanzi (1995); Lemos (1998)].

An approach in order to transfer the essential texture information from micro-scale to macro-scale has been done by [Casolo (2004b)] who modeled multi-leaf walls as rigid blocks of larger size than the original blocks connected among each other with springs. The parameters for this kind of analysis were calibrated via the study of the

23

behaviour of the original texture of the structure. This technique is promising because it reduces the high computational cost that all the discrete element analyses require. Developing the same idea, [Casolo and Peña (2007)] were able to model with rigid elements the in-plane dynamic behaviour of irregular masonry walls taking into account the material deterioration and the hysteretic energy dissipation.
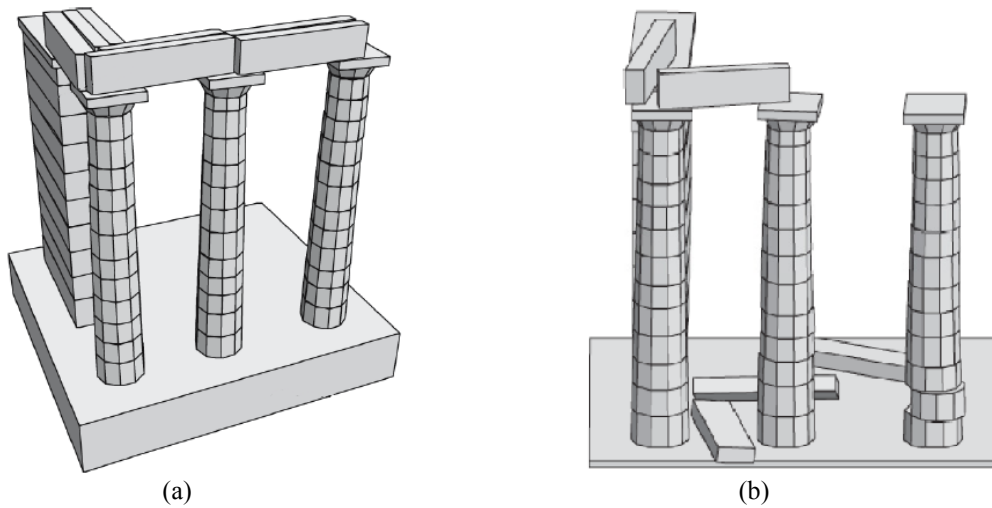

(a)   (b)

Figure 2.6: Rigid block discrete element model of the Parthenon column-architrave structure, (a) permanent deformations after seismic analysis; (b) final position of the column-architrave model without reinforcement for a simulated earthquake [Psycharis *et al.* (2003)].
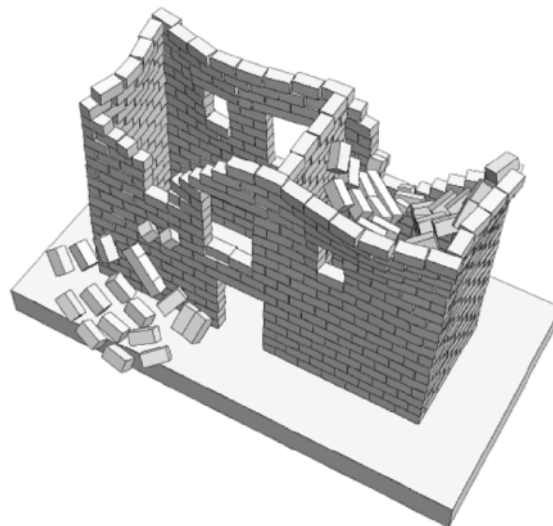
Figure 2.7: Collapse of a two-story house under seismic loading [Alexandris *et al.* (2004)].

24

2.5 Finite element method

The finite element method (FEM) is the dominant approach for the analysis of structures. It is a powerful tool which is able to simulate complex structures with linear or non-linear material properties either at a micro or macro scale. Nevertheless, the choice of the type of the analysis and the properties is firmly connected to the type of the structure that is wished to be simulated and to the computational ability which is available.

The linear elastic analysis is broadly used mainly because of its simplicity and low computational cost. It can be adequately used for materials like steel or reinforced concrete in stress levels where they appear no damages but it is not adequate for masonry structures. The reason for this is the high complexity of the masonry which, in addition to its anisotropy, behaves in a different way under compression and tension. Moreover, the fact that the tensile capacity of the masonry structures is close to zero may make such a linear analysis inaccurate even under low stress level. Also, masonry structures like arches and vaults, through the opening of cracks, create different sub-systems which no longer obey to the initial conditions and thus cannot be simulated. However, a linear analysis can take place giving results which can be used for the general understanding of the behaviour of a complex masonry structure under dynamic or quasi-static loads (Figure 2.8). Using the preliminary results of a linear analysis it is possible to be leaded to a more detailed model either fully non-linear or a hybrid where the most complex and vulnerable areas will have non-linear properties.

25
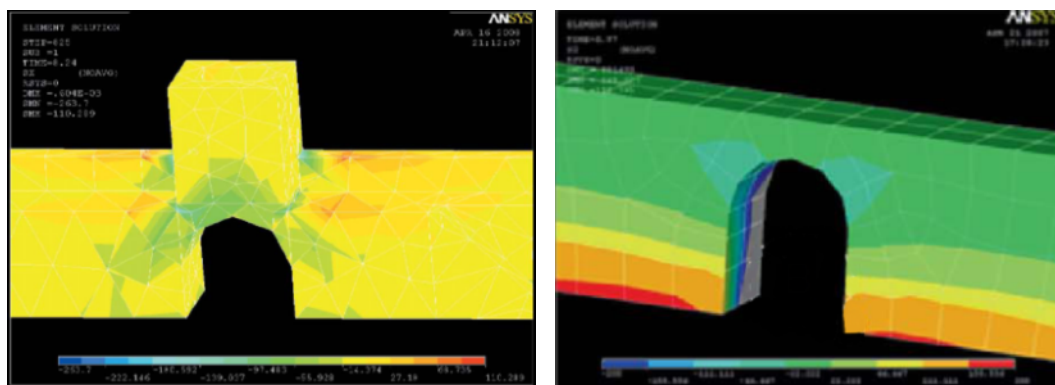
Figure 2.8: Vertical normal stresses (s_z) with time for two critical sections of the Thessaloniki wall under dynamic excitation [Stylianidis and Sextos (2009)].

Despite the well known restrictions that a linear analysis has, it has been used among others for the simulation of the Tower of Pisa [Macchi *et al.* (1993)], the Colosseum of Rome [Croci (1995)], the church of Hagia Sofia [Croci *et al.* (1997)] and the Thessaloniki fortification wall [Stylianidis and Sextos (2009)] and various other simulations with interesting results.

The non-linear analysis can be characterized by four types of non-linearity: (1) material non-linearity; (2) geometric non-linearity when the difference between the deformed and undeformed configurations is significant; (3) non-linear displacement boundary conditions; (4) non-linear applied forces or tractions. In the majority of the finite element analyses for masonry structures the most crucial types of non-linearity to be taken into account are the geometric (e.g. slender piers, deformable vaults) and the material non-linearity. In order to simulate the different behaviour of the material under tension and compression it is possible to implement various elasto-plastic constitutive laws or plasticity criteria.

Regarding the micro or macro scale of the modelling with discontinuous or continuous elements there can be done the discrimination between micro-modelling, macro-modelling or hybrids of the two.

Micro-modelling

The micro-models can successfully simulate objects consisted of multiple materials and subjected to heterogeneous state of stress or strain. Despite the high accuracy that can be achieved, such an analysis has the disadvantage of the huge computational cost that is demanded, thus it has to be limited in small structures or specimens (Figure 2.9). The material properties can be either elastic or inelastic. For application in masonry structures it is essential to know the behaviour of each of the materials, stones or mortar, and of their interface. The properties for the calibration of those model characteristics can be obtained by proper experiments on the original or similar structural elements or structures.
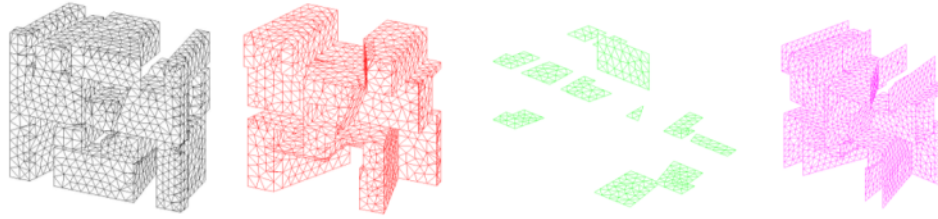
26

Figure 2.9: Basic components of a micro-model of Azores wall [Silva (2008b)].

There are two different ways to simulate the discontinuity between the mortar joints and the units (stones or bricks). The first is the detailed micro-modelling in which both the units and the mortar are simulated as continuum elements either with elastic or inelastic properties. The interface between the units and stones is represented as discontinuous elements giving the model the ability to appear local slip or crack phenomena. According to the second approach, the simplified micro-modelling, the units are represented by continuum elements but with expanded size including the half thickness of the mortar which will not be simulated directly. Instead of the mortar and the interface between mortar and units an artificial joint will be inserted (Figure 2.10). Thus, the properties of the mortar and of the interface between mortar and units are included in the properties given to the joint. Potential fracture and sliding can take place along the joint. The simplified micro-modelling is deprived of some accuracy because of the omission of the Poisson's effect of the mortar, [Lourenço (1996)].
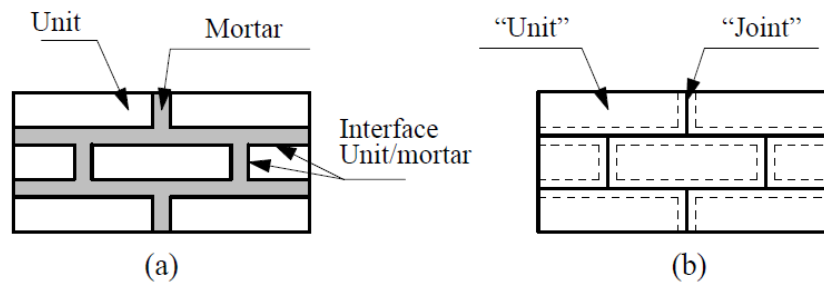
Figure 2.10: Micro-modelling strategies for masonry structures: (a) detailed micro-modelling; (b) simplified micro-modelling [Lourenço (1996)].

Macro-modelling

Due to its simplicity and the lesser calculation requirements, this approach is the mostly used for the analysis of solid walls with large dimensions. The macro-modelling treats the structure's body as homogeneous and continuous materials with either elastic or inelastic properties obeying to isotropic of orthotropic constitutive

27

laws. The size of the used finite elements can significantly affect the accuracy of the results leading to non acceptable solutions for very coarse meshes. The behaviour of the units, of the mortar and of the interface between mortar and units are incorporated in the properties of the homogeneous material. The macro-model properties can be calibrated via experimental tests of appropriate size samples from which the results will be extrapolated and included to the behaviour of the continuous material. Nevertheless, the experiments are a costly procedure which is not possible to take place for every different finite element model that needs to be calibrated. Hence, various researchers have tried to establish homogenisation techniques in order to establish constitutive relations for the strains and stresses, of the composite bodies based on the constitutive relations of the individual components. In this way, knowing the geometrical and mechanical properties of each of the components individually it is possible to predict the behaviour of the composite body. Regarding the homogenisation technique, [Lourenço [(1996)] proposed a matrix formulation which allows a clear numerical implementation. In this technique the masonry is assumed to be a layered material simplifying significantly the complexity of the problem.

2.5.1 Damage propagation

The material damage and degradation caused by the imposed loads during the analysis can be simulated with appropriate damage models. There can be done discrimination between discrete crack models and smeared crack models. They were introduced by Ngo and Scordelis [(1967)] and Rashid [(1968)] respectively for the study of concrete fracture.

Discrete crack models

In the discrete crack models the fracture is introduced by the creation of a geometrical opening in the body of the structure. When the tensile failure criteria are achieved, the critical node splits into two nodes with no connection among them (Figure 2.11). Then the crack is able to propagate to the next node. One of the main disadvantages of this approach is the high dependency of the crack propagation, which is propagated

28

along the element boundaries, from the mesh characteristics. The effect of the mesh bias can be reduced by the implementation of high quality automatic re-meshing [de Borst *et al.* (2004)].
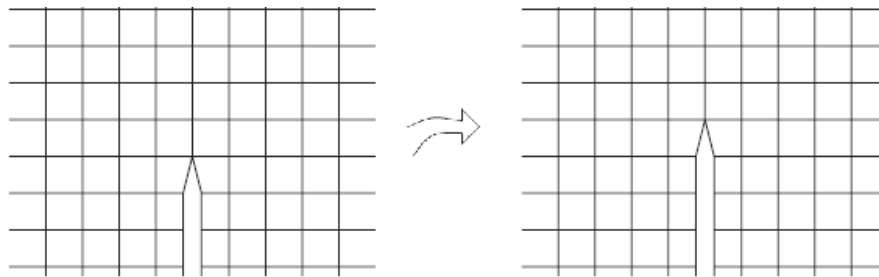

Figure 2.11: Crack propagation with discrete crack models [de Borst *et al.* (2004)].

In the work of Gambarotta and Lagomarsino [(1997)] it is proposed a discrete damage model for mortar joints which takes into account both the mortar damage and the decohesion in the mortar-brick interface (Figure 2.12). The sliding and the extension of the mortar joints which are non-linear phenomena are connected linearly to the mean stress and damage variable. The friction during the sliding gives the ability to the model to appear an hysteretic response of the joint under cyclic shearing strains.
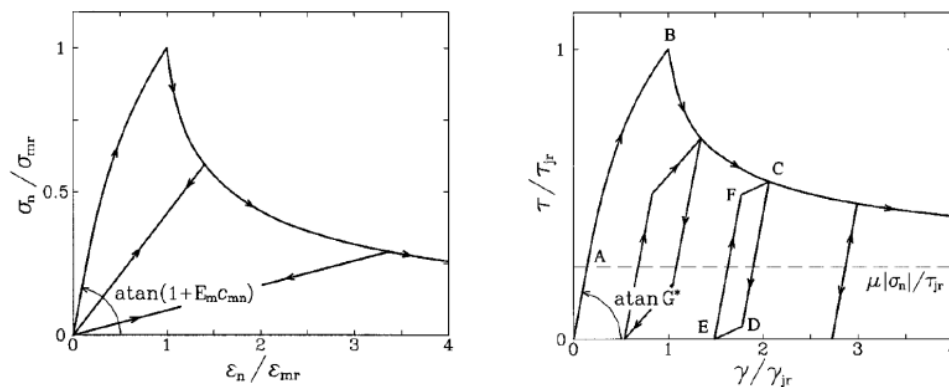
Figure 2.12: Response of the mortar joint model to: (a) tensile stresses; (b) shearing strain superimposed on constant compressive stress [Gambarotta and Lagomarsino (1997)].

Smeared crack models

The other approach, the smeared crack models which are mainly used in marco-modelling, is focused on the continuum mechanics domain. In those models the damage is presented as a scalar value which ranges between the intact elastic state and the complete collapse (Figure 2.13). The effect of the crack is smeared in the broader area of the integration point. The deterioration of the material is represented with the

29

reduction of the current stiffness and strength at the integration point when the combination of stresses satisfies a specified criterion [de Borst *et al.* (2004)]. Also, for the definition of the cracked stage, no interface elements are needed and there are no restrictions about the direction and location of the cracks. Different constitutive models, governed by different equations, have been built for the representation of the damage. They can be connected to the decomposed strains, to the total strains, to the plasticity of other damage formulations.
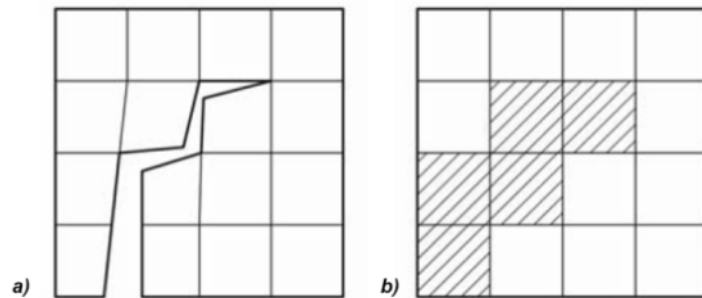
Figure 2.13: Modeling of fracture: (a) discrete crack model [Cervera *et al.* (2006)]; (b) smeared crack model [Rots (1992)]

Despite the fact that the smeared crack models are broadly used, the representation of the damaged material as a vast volume, which does not represent the reality of the damage in masonry structures, is the main drawback of the method. The vulnerable areas can be detected in an acceptable level but the local behaviour based on geometrical particularities is not possible to taken into account effectively (Figure 2.14). Nevertheless the method is considered to be able to capture the overall damage behaviour of large dimensions structures giving an idea about the global phenomena. [Silva (2008a)]. Thus, it can be said that it is an acceptable method of representing the damage in structures with large volumes but it requires deeper investigation if it is necessary to focus on smaller scale structures or on structures with high irregularity.
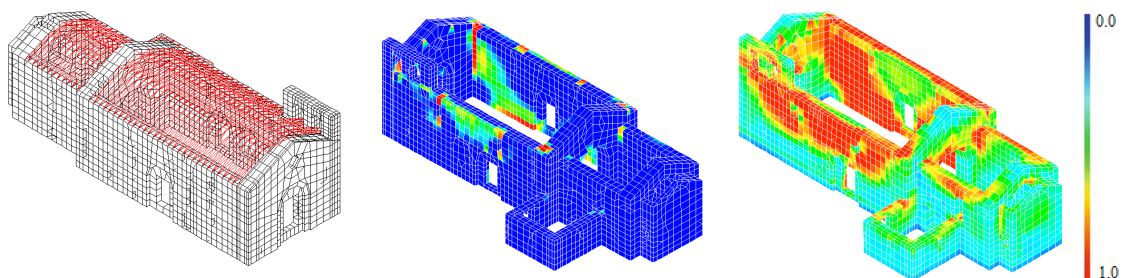
Figure 2.14: Smeared crack representation of the tensile damage in Gondar church [Silva (2008a)].

An early development has done by [Hillerborg *et al.* (1976)] with the formulation of a frictious crack model, which was an adaptation of previously formulated cohesive crack models already adopted in nonlinear fracture mechanics. According to it, the loss of cohesion in the forming crack should be related to the experimentally measurable fracture energy of the material. Later in the work of Bazant and Oh [(1983)] the same model was improved in order to be more compatible with most of the finite element codes.

A further development of the method has been done in the work of Saetta *et al.* [(2000)] where an orthotropic damage model for brittle failure of masonry for in-plane loading was built. This model uses four different damage parameters, one in compression and one in tension for the two natural axes. The innovation of the model is that it allows the stiffness recovery due to crack closure and it also introduces different inelastic behaviour along each of the natural axes. The evolution laws of the damage indexes are based on the proposal of Faria *et al.* [(1998)] for concrete structures. This damage approach was enhanced by Berto *et al.* [(2001)] with the addition of a shear factor which allows taking into account the friction effect along a crack and the possibility of considering irreversible strains. The model was validated comparing the results of the numerical analyses with former experimental work on biaxially loaded masonry panels.

An interesting modification was proposed by Clemente *et al.* [(2006)] to the smeared crack scalar damage models giving the ability to reproduce localized individual (discrete) cracks (Figure 2.15). This is achieved with the use of auxiliary tracking algorithms in order to trace the progress of the localization band through the finite element mesh. Thus, the cracks are simulated in a much more realistic way than in the smeared-crack models and it is possible to develop hinges and to follow kinematic mechanisms of collapse in accordance with the limit analysis.
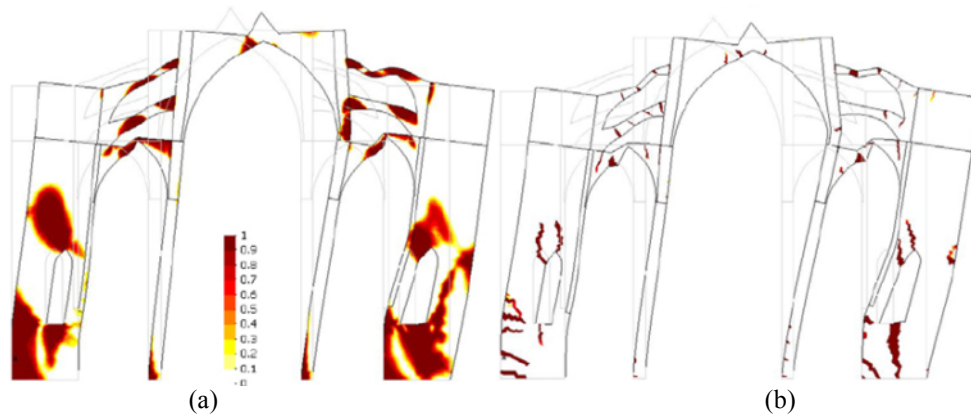
Figure 2.15: Seismic analysis of Mallorca Cathedral for and earthquake of 475 years return period. (a) Smeared damage approach; (b) localized damage approach [Clemente *et al.* (2006)].

The same model was developed even further by Pelá *et al.* [(2008); Pelá (2009)] with a modification in order to be able to take into account the orthotropy of the masonry which leads to even more realistic results. In Cervera *et al.* [(2010)a] with the use of new elements labelled as potential crack roots, the tracking algorithm detects the point where the crack is originated and then makes it to propagate perpendicularly to the trajectory of the first principal tensile stress in a more efficient way than previous approaches (Figure 2.16). Thus, it is possible to have a rather realistic formation of the damages without high computational effort. Moreover, it was proved that analysis results are mesh-bias independent ensuring the consistency of the method. This model was enhanced by Cervera *et al.* [(2010)b; (2010)c] in order to become more robust and to eliminate problems that encountered when with the modelling of the strain localization.
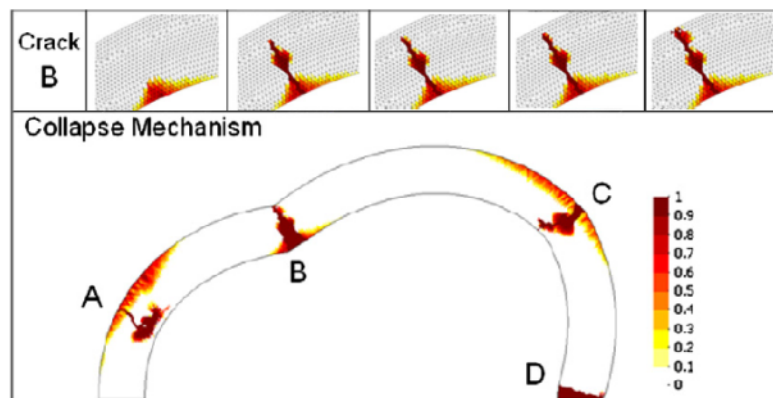
Figure 2.16: Smeared damage model (analysis under force control): crack growth at different stages of the calculus and final collapse mechanism (amplification of the mesh deformation: x 100) [Cervera *et al.* (2010)a].

2.6 Continuous damage model

The damage model which will be used was firstly developed by Faria and Oliver [(2003)] and later enhanced by Faria *et al.* [(1998)]. Although the initial development of the model was done the seismic analysis of massive concrete structures it is also sufficient for the analysis of masonry structures. The model is based on the continuum mechanics and with a strain-based formalism obtains a higher algorithmic efficiency. According to the authors, some of the main features that were selected to be modeled in order to have a realistic behaviour are the following: (1) the rather distinct stress-strain envelopes obtained under tension or under compression, with large differences in their peak strengths, (2) the stiffness recovery upon loading reversal, (3) the concrete strength enhancement discernible under 2D or 3D compressive tests, when compared to the 1D compressive strength, (4) the plastic deformations observable upon unloading after some compressive stress threshold has been attained. [Faria *et al.* [(1998)]. There was special care in order the model to keep the computational demands in a reasonable level because of the big size and the complexity of the structures that need to be analysed. The model was verified by comparing the numerical results with experimental results and with numerical results of other proposed methods. The description of the model is following.

2.6.1 Helmholtz free energy potential

The formula which gives the effective stress tensor is the following:

$$\overline{\sigma}(\varepsilon, \varepsilon^p) = \mathbf{D}_0 : (\varepsilon - \varepsilon^p) \quad (2.1)$$

Where,

$\mathbf{D}_0$ is 4th order symmetric tensor of the linear elasticity of the material.

ε is the strain tensor (rank two)

ε^p is the plastic strain tensor (rank two)

33

It is crucial to split the effective stress tensor $\overline{\sigma}$ tensile and compressive stresses ($\overline{\sigma}^+$, $\overline{\sigma}^-$). The aim of this is to make possible the distinction of the stress contributions and the later the creation of independent non-linear degradation mechanisms. With this way the opening and the closing of the cracks can be taken into account.

$$\overline{\sigma}^+ = \left\langle \overline{\sigma} \right\rangle = \sum_{i=1}^{3} \left\langle \overline{\sigma}_i \right\rangle \mathrm{p}_i \otimes \mathrm{p}_i \quad (2.2a)$$

$$\overline{\sigma}^- = \left\langle -\overline{\sigma} \right\rangle = \sum_{i=1}^{3} \left\langle -\overline{\sigma}_i \right\rangle \mathrm{p}_i \otimes \mathrm{p}_i = \overline{\sigma} - \overline{\sigma}^+ \quad (2.2b)$$

Where,

$\overline{\sigma}_i$ is the ith principal stress

p_i is the vector which corresponds to the principal direction, p_i $\left(\left\| p_i \right\| = 1 \right)$

$\otimes$ is the symbol which denotes the tensor product.

$\left\langle . \right\rangle$ are the Macauley brackets (ramp function) that are returning the enclosed value if it is positive or they are setting zero if the value is negative.

It is necessary to use a free energy potential with free and internal variables in order to establish a constitutive law. This can be done assuming a Helmholtz free energy potential with the form [Faria and Oliver (1993)]:

$$\psi(\varepsilon, \varepsilon^p, d^+, d^-) = (1 - d^+) \psi_0^+ (\varepsilon, \varepsilon^p) + (1 - d^-) \psi_0^- (\varepsilon, \varepsilon^p) \quad (2.3)$$

Where ψ_0^+ and ψ_0^- are the elastic free energies associated to the stress tensors:

$$\psi_0^+ (\overline{\sigma}(\varepsilon, \varepsilon^p)) = \frac{1}{2} \overline{\sigma}^+ : \mathbf{D}_0^{-1} : \overline{\sigma} \quad (2.4a)$$

$$\psi_0^- (\overline{\sigma}(\varepsilon, \varepsilon^p)) = \frac{1}{2} \overline{\sigma}^- : \mathbf{D}_0^{-1} : \overline{\sigma} \quad (2.4b)$$

Where $\mathbf{D}_0^{-1}$ is the inverse of the linear elasticity matrix defined according to

$$\mathbf{D}_{0ijkl}^{-1} = \mathbf{D}_{0klij}^{-1} = \frac{1}{E} \left[\frac{1+v}{2} (\delta_{ik}\delta_{jl} + \delta_{il}\delta_{jk}) - v\delta_{ij}\delta_{kl} \right] \quad (2.5)$$

34

Where,

E is the Young modulus of elasticity

v is the Poisson's ratio

δ is the Kronecker delta

It has to be mentioned that the defined Helmholtz free energy is not defined in exactly the same way with [Mazars and Pijaudier-Cabot (1989)] and [La Borderie *et al.* (1990)] where it is used the Cauchy stress tensors instead of the effective stress tensor $\overline{\sigma}$.

In the case that there is no damage and no plasticity to the material $(d^+ = d^- = 0, \varepsilon^p = 0)$ the free energy potential ψ is equal to the elastic free energy ψ_0 obeying with this way the fundamental thermodynamic rules. This behaviour can be described using the equations (m.1)-(m.4) and leading to the:

$$\psi_0 = \psi_0^+ + \psi_0^- = \frac{1}{2}(\overline{\sigma}^+ + \overline{\sigma}^-) : \mathbf{D}_0^{-1} : \overline{\sigma} = \frac{1}{2}\varepsilon : \mathbf{D}_0^{-1} : \varepsilon \geq 0 \quad (2.6)$$

As it is shown by Faria and Oliver (1993), the free energy can be split into positive and negative components:

$$\psi_0^+ \geq 0 \quad ; \quad \psi_0^- \geq 0 \quad (2.7)$$

If it is taken into account that the damage variables are:

$$0 \leq (d^+, d^-) \leq 1 \quad (2.8)$$

it can be proven that

$$\psi = (1-d^+)\psi_0^+ + (1-d^-)\psi_0^- \geq 0 \quad (2.9)$$

The thermodynamic forced associated to the damage variables can be found by deriving the thermodynamic potential:

$$-\frac{\partial \psi}{\partial d^+} = \psi_0^+ \quad ; \quad -\frac{\partial \psi}{\partial d^-} = \psi_0^- \quad (2.10)$$

Those formulas represent the elastic energy strain that is released during the growth of the correspondent damage variable as it is also referred by Chaboche (1977).

35

2.6.2 Damage criteria

In order to define the damage criteria and the way the material behaves under the loading cycles it is necessary to define the term of the equivalent stress which is a scalar positive quantity. This is analogous to the concept of the equivalent strain used by Simo and Ju (1988).

Also here, it is possible to split the stresses into the tensile equivalent component τ^+ and the compressive equivalent component τ^-:

$$\tau^+ = \sqrt{\overline{\sigma}^+ : \mathbf{D}_0^{-1} : \overline{\sigma}^+} \quad (2.11a)$$

$$\tau^- = \sqrt{\sqrt{3}(K\overline{\sigma}_{oct}^- + \overline{\tau}_{oct}^-)} \quad (2.11b)$$

Where,

$\overline{\sigma}_{oct}^- + \overline{\tau}_{oct}^-$ are the octahedral normal stress and the octahedral shear stress obtained from the tensor $\overline{\sigma}^-$.

K is a material property correlated to increment of the strength coming from biaxial and triaxial tests.

There are used two damage criteria g^+ and g^- for the tension and compression respectively:

$$g^+ = (\overline{\tau}^+, r^+) = (\overline{\tau}^+ - r^+) \leq 0 \quad (2.12a)$$

$$g^- = (\overline{\tau}^-, r^-) = (\overline{\tau}^- - r^-) \leq 0 \quad (2.12b)$$

The r^+ and r^- are the damage threshold variables which control the expansion of the damaged surfaces. It needs to be mentioned that before any application of load, the initial state of the material must be set setting the damage threshold variables to the values r_0^+ and r_0^- which correspond to the linear elastic domain.

The use of the eqns (2.11a) and (2.12a), if $(\overline{\sigma}_1, \overline{\sigma}_2, \overline{\sigma}_3) \leq 0$ the 3D effective stresses corresponding to the same norm, gives a quarter of an ellipsoid centered at the origin in the space of principal effective stresses. A representation in 2D can be shown in

36

Figure 2.17 when $\bar{\sigma}_2 = 0$ and $\tau^+ = r_0^+$. When considering the eqns (2.11b) and (2.12b), if $(\bar{\sigma}_1, \bar{\sigma}_2, \bar{\sigma}_3) \leq 0$ the 3D effective stresses resemble the Drucker-Pragger cone. A representation in 2D can be shown in Figure 2.17 when $\bar{\sigma}_2 = 0$ and $\tau^- = r_0^-$. A further calibration of the model can be achieved by altering the material property K.

In the Figure 2.17 is also shown that experimental the results from Kupfer *et al.* (1969) are similar with the ones that where predicted by the current model. Thus the overall agreement is considered to be acceptable not only for pure compression or tension but also for the combination of tension-compression.
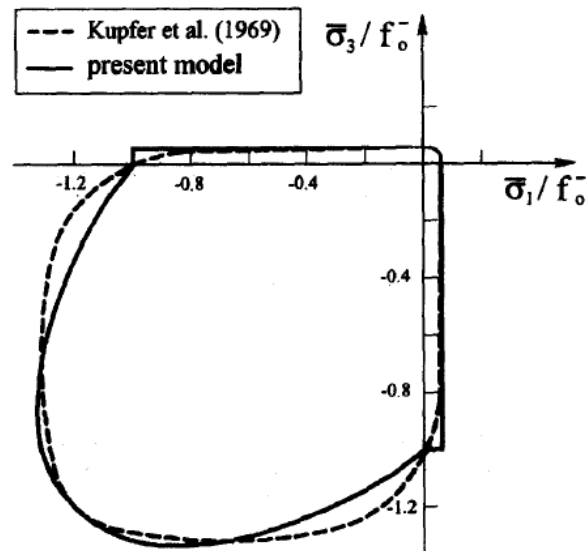
Figure 2.17: Comparison of the experimental results in the 2D elastic domain [Faria and Oliver (1993)].

37

2.6.3 Evolution laws for the damage variables

The damage variables can be found according to the following equations for tension and compression. The expansion of the equations and a deeper approach is fully described by Faria and Oliver (1993).

Tension:

$$\dot{d}^+ = \dot{\partial}^+ \frac{\partial G^+(\bar{\tau}^+)}{\partial \bar{\tau}^+} \quad (2.13)$$

$$\dot{r}^+ = \dot{\partial}^+ \quad (2.14)$$

Compression:

$$\dot{d}^- = \dot{\partial}^- \frac{\partial G^-(\bar{\tau}^-)}{\partial \bar{\tau}^-} \quad (2.15)$$

$$\dot{r}^- = \dot{\partial}^- \quad (2.16)$$

Where,

G^+ and G^- are monotonically increasing functions occurred from experimental results

∂^+ and ∂^- are damage consistency parameters.

The damage parameters for tension and compression expressed in compact form through the Kuhn-Trucker relations are the following:

Tension:

$$\dot{\partial}^+ \geq 0 \quad ; \quad g^+ \leq 0 \quad ; \quad \dot{\partial}^+ g^+ = 0 \quad (2.17)$$

Compression:

$$\dot{\partial}^- \geq 0 \quad ; \quad g^- \leq 0 \quad ; \quad \dot{\partial}^- g^- = 0 \quad (2.18)$$

The finally adopted laws of evolution are the ones which were introduced by Oliver *et al.* (1990) and Farria and Oliver (1993):

Tension:

$$d^+ = 1 - \frac{r_0^+}{\bar{\tau}^+} e^{\left(A^+ \left(1 - \frac{\bar{\tau}^+}{r_0^+} \right) \right)} \quad (2.19)$$

Where the parameter A^+ can be found as it is described by Oliver *et al.* (1990):

$$A^+ = \left(\frac{G_f E}{l_{ch} f_0^{+2}} - \frac{1}{2} \right)^{-1} \geq 0 \quad (2.20)$$

G_f is the fracture energy

E is the Young's modulus of elasticity

l_{ch} is the characteristic length which depends of the size (area or volume) of the finite elements which are used and it is introduced in order the mesh and the spatial discretisation to be taken into account. The tensile fracture energy G_f/l_{ch} is defined as the area retained under the stress-strain curve.

Compression:

$$d^- = 1 - \frac{r_0^-}{\bar{\tau}^-}(1 - B^-) - B^- e^{A^-\left(1 - \frac{\bar{\tau}^-}{r_0^-}\right)} \quad (2.21)$$

Where the A^- and B^- can be defined by imposing the σ-ε 1D curve to pass through two predefined points of a curve given by a uniaxial compressive test.

2.6.4 Evolution laws for the plastic strain tensor

According to Faria and Oliver (1993) the plastic strain tensor $\dot{\varepsilon}^p$ can be found from the following formula:

$$\dot{\varepsilon}^p = \beta E H(\dot{d}^-) \frac{\langle \bar{\sigma} : \dot{\varepsilon} \rangle}{\bar{\sigma} : \bar{\sigma}} \mathbf{D}_0^{-1} : \bar{\sigma} \quad (2.22)$$

The material parameter $\beta \geq 0$ is used in order to describe the rate intensity of the plastic deformation. If $\beta = 0$, then the model behaves in an elastic way in terms of damage. $H(\dot{d}^-)$ is the Heaviside step function for the compressive damage rate. With the use of the following definition

$$\mathbf{1}_{\bar{\sigma}} = \frac{\bar{\sigma}}{\sqrt{\bar{\sigma} : \bar{\sigma}}} \quad (2.23)$$

39

the eqn (2.19) can be compacted to the form:

$$\dot{\varepsilon}^p = \beta EH(\dot{d}^-)\langle \mathbf{1}_{\bar{\sigma}} : \dot{\varepsilon}\rangle \mathbf{D}_0^{-1} : \mathbf{1}_{\bar{\sigma}} \quad (2.24)$$

It needs to be said that the kinematic laws proposed for the irreversible strains contain some simplifications based on hypotheses which have been done in order the model to become functional for large scale seismic analyses which are very demanding processes. The proposed model does not have the ability to predict the irreversible strains caused by pure tension. This is from the eqn (2.24) that the plastic strain depends only from the compression variable d^- and not from the tension. Another limitation is that it is assumed that the plastic strain evolution has the same direction with the elastic strain tensor. This approaches the reality but it is still a simplification.

Finally, the current model, using the factor $H(d^-)$, is not possible to present plastic strains during damage unloading or before attaining the compressive damage thresholds. This for instance can be shown in a uniaxial compressive test where the model will give an unloading with straight lines with the current damaged modulus and not with the elastic modulus as in the classic plasticity theory. [Faria *et al*. (1998)]

2.6.5 Energy dissipation

Due to the second principle of thermodynamics any non-negative energy dissipation like the one that is produced by the loading process, leads to an irreversible process. This is expressed by the Clausius-Duheim inequality which can be written as:

$$\dot{\gamma} = -\dot{\psi} + \sigma : \dot{\varepsilon} \geq 0 \quad (2.25)$$

Through the use of the eqns (2.3) and (2.4) the previous can take the form:

$$\dot{\psi} = \frac{\partial \psi}{\partial \varepsilon} : \dot{\varepsilon}^p + \frac{\partial \psi}{\partial \varepsilon^p} : \dot{\varepsilon}^p + \frac{\partial \psi}{\partial d^+} d^+ + \frac{\partial \psi}{\partial d^-} d^- \quad (2.26)$$

By combining with the eqns (2.10) it can be taken the following equation for the dissipation:

$$\dot{\gamma} = (\sigma - \frac{\partial \psi}{\partial \varepsilon}) : \dot{\varepsilon}^p + \psi_0^+ d^+ + \psi_0^- d^- - \frac{\partial \psi}{\partial \varepsilon^p} : \dot{\varepsilon}^p \geq 0 \quad (2.27)$$

40

The ε is a free variable and in order to keep the generality, the expression within the parenthesis of the eqn (2.27) must cancel. Thus:

$$\sigma = \frac{\partial \psi}{\partial \varepsilon} \quad (2.28)$$

This is one of the Coleman's relations, necessary for attaining the constitutive law.

Decomposing the strain tensor ε into elastic and plastic components ε^e and ε^p respectively, the effective stress tensor can be expressed as:

$$\overline{\sigma}(\varepsilon^e) = \mathbf{D}_0 : (\varepsilon - \varepsilon^p) = \mathbf{D}_0 : (\varepsilon^e) \quad (2.29)$$

By replacing the eqn (2.29) to the eqns (2.4) the last take the form:

$$\psi_0^+(\varepsilon^e) = \frac{1}{2}\overline{\sigma}^+ : \varepsilon^e \quad (2.30a)$$

$$\psi_0^-(\varepsilon^e) = \frac{1}{2}\overline{\sigma}^- : \varepsilon^e \quad (2.30b)$$

Using the chain rule, the eqn (2.28) becomes:

$$\sigma = \frac{\partial \psi_0^+}{\partial \varepsilon^e} : \frac{\partial \varepsilon^e}{\partial \varepsilon} = \frac{\partial \psi}{\partial \varepsilon^e} \quad (2.31)$$

which, via the eqn (2.3) takes the form:

$$\sigma = (1-d^+)\frac{\partial \psi_0^+}{\partial \varepsilon^e} + (1-d^-)\frac{\partial \psi_0^-}{\partial \varepsilon^e} \quad (2.32)$$

Through the linear dependency between $\overline{\sigma}$ and ε^e linear which is expressed at the eqn (2.29) and by using the split stress of the eqn (2.2) it results in:

$$\overline{\sigma}^+(m\varepsilon^e) = m\overline{\sigma}^+(\varepsilon^e) \quad (2.32)$$

Where, m is an arbitrary scalar parameter.

The $\overline{\sigma}^+$ and $\overline{\sigma}^-$ are first degree homogeneous functions of ε^e and according to the Euler's theorem, it occurs that:

$$\sigma^+(\varepsilon^e) = \frac{\partial \overline{\sigma}^+}{\partial \varepsilon^e} : \varepsilon^e \quad ; \quad \sigma^-(\varepsilon^e) = \frac{\partial \overline{\sigma}^-}{\partial \varepsilon^e} : \varepsilon^e \quad (2.33)$$

Deriving the eqns (2.30) with respect to ε^e it gives:

$$\frac{\psi_0^+}{\partial \varepsilon^e} = \frac{1}{2}\frac{\partial \overline{\sigma}^+}{\partial \varepsilon^e} : \varepsilon^e + \frac{1}{2}\overline{\sigma}^+ \quad ; \quad \frac{\psi_0^-}{\partial \varepsilon^e} = \frac{1}{2}\frac{\partial \overline{\sigma}^-}{\partial \varepsilon^e} : \varepsilon^e + \frac{1}{2}\overline{\sigma}^- \quad (2.34)$$

41

Which, with the eqns (2.33) becomes for tension and compression respectively:

$$\frac{\psi_0^+}{\partial \varepsilon^e} = \overline{\sigma}^+ \quad ; \quad \frac{\psi_0^+}{\partial \varepsilon^e} = \overline{\sigma}^+ \quad (2.35)$$

A final form for the constitutive law is produced combining the eqns (2.32) and (2.35):

$$\sigma = (1-d^+)\overline{\sigma}^+ + (1-d^-)\overline{\sigma}^- \quad (2.36)$$

In order the Clausius-Duheim dissipation inequality to be applicable, it need to be ensured that $\dot{\gamma} \geq 0$. The the eqn (2.27), taking in mind the eqn (2.28) is being compacted in

$$\dot{\gamma} = \psi_0^+ d^+ + \psi_0^- d^- - \frac{\partial \psi}{\partial \varepsilon^p} : \dot{\varepsilon}^p \quad (2.37)$$

where the two first products are non-negative and it needs to be ensured that also the last component is non-negative.

The eqn (2.37) can be transformed with the use of the eqn (2.22) to the:

$$\dot{\varepsilon}^p = b\mathbf{D}_0^{-1} : \overline{\sigma} \quad (2.38)$$

Where, b is a non-negative scalar

$$b = \beta E H(\dot{d}^-) \frac{\langle \overline{\sigma} : \dot{\varepsilon} \rangle}{\overline{\sigma} : \overline{\sigma}} \geq 0 \quad (2.39)$$

Also,

$$\frac{\partial \psi}{\partial \varepsilon^p} = \frac{\partial \psi_0^+}{\partial \varepsilon^e} : \frac{\partial \varepsilon^e}{\partial \varepsilon} = -\frac{\partial \psi}{\partial \varepsilon^e} \quad (2.40)$$

By the eqns (2.39), (2.40), (2.36) and (2.31) it is produced:

$$-\frac{\partial \psi}{\partial \varepsilon^p} : \dot{\varepsilon}^p = b[(1-d^+)\overline{\sigma}^+ : \mathbf{D}_0^{-1} : \overline{\sigma}^+ + (1-d^-)\overline{\sigma}^- : \mathbf{D}_0^{-1} : \overline{\sigma}^-] \quad (2.40)$$

With the use of the eqns (2.3) and (2.4) the previous can transforms into:

$$-\frac{\partial \psi}{\partial \varepsilon^p} : \dot{\varepsilon}^p = 2b\psi \quad (2.40)$$

Hence, since both *b* and ψ are non-negative, the Clausius-Duheim dissipation inequality is well defined:

$$\dot{\gamma} = \psi_0^+ \dot{d}^+ + \psi_0^- \dot{d}^- + 2b\psi \geq 0 \quad (2.41)$$

42

2.6.6 Graphic representation of the constitutive laws

Tension

In a uniaxial case of pure tension the constitutive law of the eqn (2.36) changes to:

$$\sigma = (1-d^+)\bar{\sigma} = (1-d^+)E\varepsilon \quad (2.41)$$

which is graphically represented in the Figure 2.18.
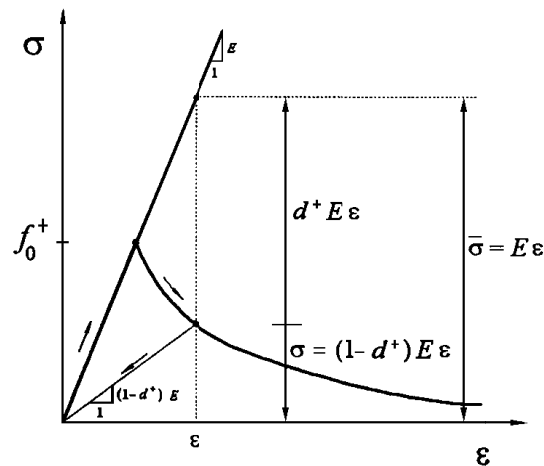
Figure 2.18: σ-ε diagram for pure tension   .

Compression

Considering the case of pure compression, the constitutive law of the eqn (2.36) changes to:

$$\sigma = (1-d^-)\bar{\sigma} = (1-d^-)E(\varepsilon - \varepsilon^p) \quad (2.42)$$

which is graphically represented in the Figure 2.19.
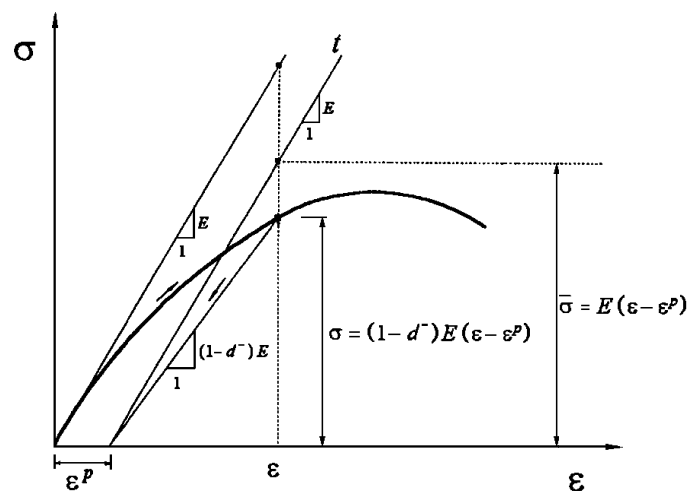
Figure 2.19: σ-ε diagram for pure compression.

43

44

Chapter 3

Current experimental campaign of UNIPD

3.1 Introduction

The experimental campaign of the University of Padova (UNIPD) has the aim of analysing the behaviour of three-leaf stone masonry walls both in strengthened and in original condition. The strengthening technique which was used was the grout injection with natural hydraulic lime-based grout. The walls were tested in compression and in combination of shear-compression. The building procedure started in March 2010 and the laboratory tests initiated in June 2011.

3.2 Building procedure

For the needs of the campaign, 20 three-leaf panels in 1:1 scale, 14 three-leaf panels in 2:3 and 4 single leaf panels were built in the area of the Scuola Edile of Verona. The walls were built according to the traditional construction technique with the outer leaves consisted of two different types of irregular and regular shape stone blocks and inner core filled with rubble material (Figure 3.1). The mortar of the external leaves was the T30V, provided by Tassullo S.p.A. For reproducing the worst conditions no mortar was used for the infill and no transversal connection between the leaves was provided. Two horizontal concrete beams were built on the top and base of the walls

46

for facilitating the transportation of the walls to the laboratory and the uniform application of the load for the testing necessities.

Figure 3.1: Building procedure: (a) Face of the wall; (b) Section with the rubble material.

The walls were built as continuous bodies with the half wall to remain in the original state and the other half to be subjected to injections. Later they were divided into separate panels with the cut by a wire saw. With this method it was achieved a clean cut allowing a visual survey of the effectiveness of the injection technique. Moreover, constructive inhomogenities that would be created by the building of separate panels were avoided. In this way the reality where the walls are continuous bodies is better reproduced. Also, it made easier the interpretation of the experimental results via the comparison, because every wall produced equal amount of injected and non-injected panels with the same geometrical and constructive characteristics. An intermediate small portion of every wall was cut before the injection in order not to insert grout to the part which was not intended to be strengthened. The details of the panels are presented in the Table 3.1.

Table 3.1: Dimensions of the masonry panels

Number of panels	Dimensions [cm] length x height x width	Layers [cm]	Scale	Laboratory tests
6	150x220x50	18/14/18	1:1	3 in compression/4 in shear- compression
14	100x120x50	18/14/18	1:1	3 in compression/4 in shear- compression
14	80x100x33	12/9/12	2:3	3 in compression/4 in

47

4	80x100x18	18/-/-	1:1	shear- compression 4 in compression
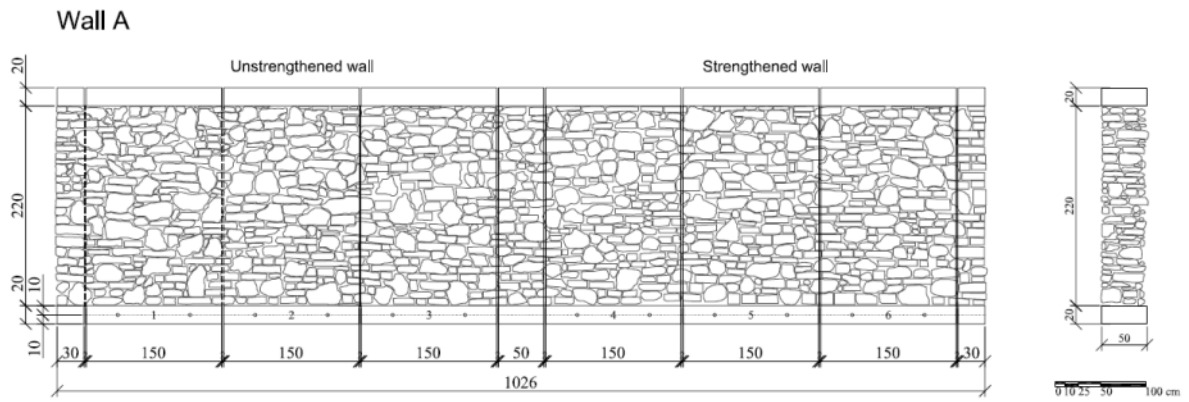
Wall A

Figure 3.2: Division into panels of the three-leaf wall A (1:1).
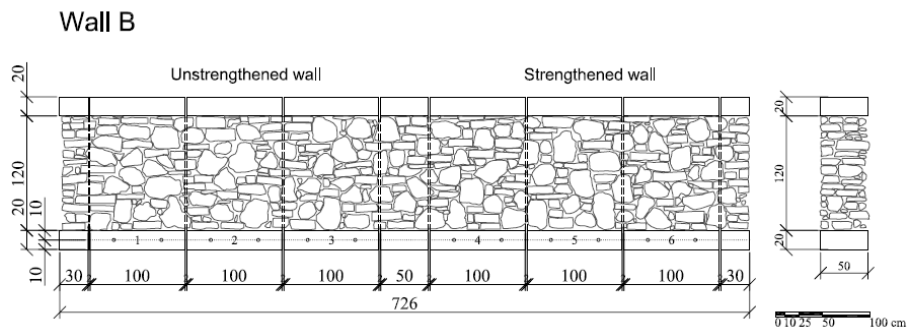
Wall B

Figure 3.3: Division into panels of the three-leaf wall B (1:1).
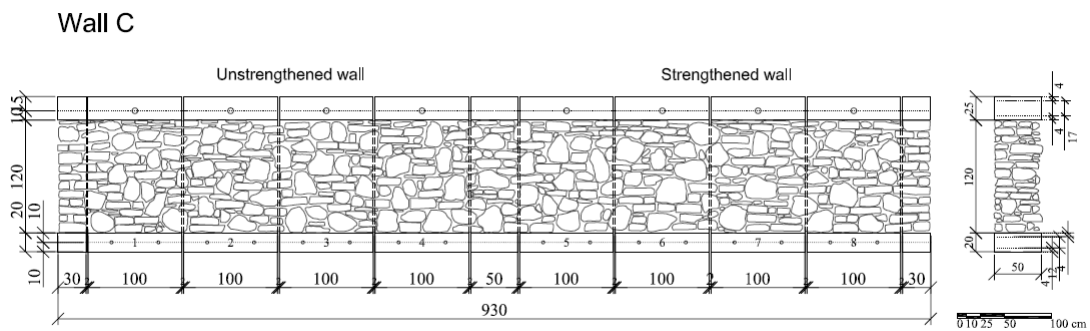
Wall C

Figure 3.4: Division into panels of the three-leaf wall C (1:1).

48
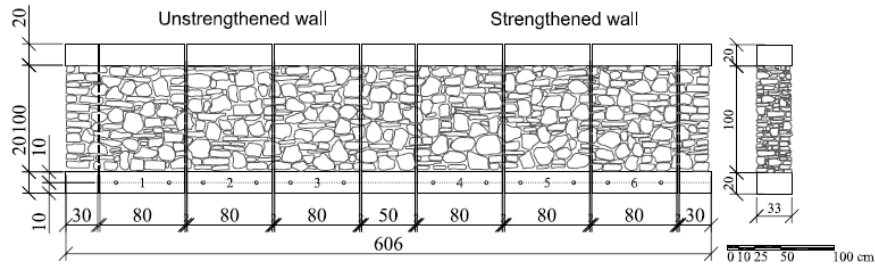
Figure 3.5: Division into panels of the three-leaf wall D (2:3).
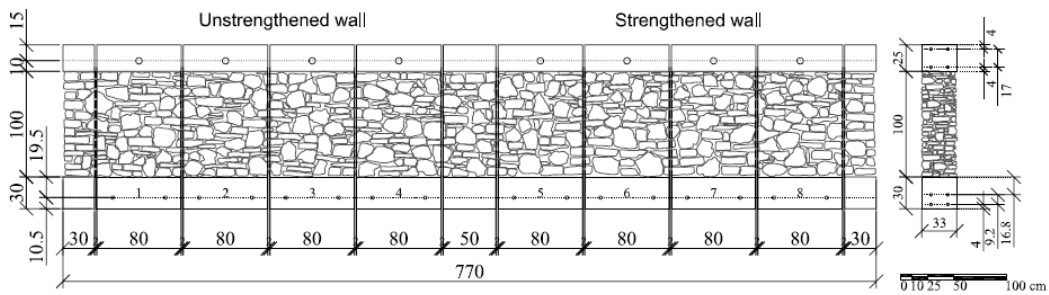
Figure 3.6: Division into panels of the three-leaf wall E (2:3).
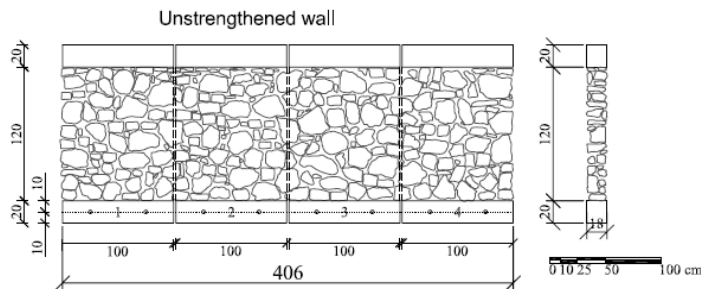
Figure 3.7: Division into panels of the single-leaf wall F (1:1)

3.3 Grout injection procedure

This intervention technique is mainly focused on the strengthening of historical and old constructions built with traditional techniques. For achieving compatibility with

49

the traditional materials and for avoiding to avoid chemical and physical deterioration problems, the grout was selected to be natural hydraulic lime-based. The grout which was used was provided by Tassullo S.p.A. and it had the commercial name Fenix-B.

The drilled holes had the diameter of 2 cm and their depth was enough in order to reach the inner core making possible the insertion of the grout there. The arrangement of the holes was triangular which is the most recommended. Holes functioning as control points were also opened at the back side of the walls but with less dense arrangement. The injection holes have distance around 30cm, in this way the density of the injection holes is 11-12 holes/m^2. The control holes were opened in a less dense distribution.

Although that a washing using water inside the holes would be help in the better binding and consolidation of the materials, this technique was not used. The reason was the will to simulate the reality where it is very often impossible to clean structures of historical and architectural heritage using water. Thus, the real absorption of the grout by the ancient and dehydrated materials was reproduced. Due to this, the fluidity of the grout was reduced as it was testified by the grout overflowing from the cracks and the holes.

The mixing of the grout was done with a compact mixing pump (m-tec mono mix FU) using 8-9 liters of water for each 25 kg bag of mortar. The fluidity and the stability of the mixture were checked with the Marsh and ASTM cone tests which will be described later. There was no manometer available for measuring the pressure which is considered to be around 0.5-1 atm according to other similar works.

The injection took place starting from the bottom row of holes moving from the edges to the centre for achieving better distribution of the grout and later moving upward to the next row following the same horizontal sequence. The flow of the grout was visible due to the utilisation of plastic tubes and nozzles.

The injection of one hole was being terminated when the grout was overflowing from another hole or a crack in great volumes. The sealing of each hole after the termination of its injection was done with mortar. Minor overflowing of the grout from small cracks was being blocked also by the sealing with mortar without the termination of the injection process.

50

After the superficial settling of the sealing mortar and the overflowing grout, the surfaces of the walls were cleaned with wire brushes. The only scope of this was the restoration of the initial appearance of the walls before the intervention technique. Indeed, having a sealing mortar and grout of similar to the original colours of the materials, the intervention did not affecting the appearance of the wall proving in this way that the grout injection can be good intervention technique for historical structures.

3.3.1 Rheological and physical properties of the grout

Fluidity

The fluidity has been evaluated by measuring the outflow time of the grouts via two different tests:

The standardized by ASTM [Standard C939 (2010)], flow cone with time limits between 19-23 sec.

The "Marsh cone" [Miltiadou (1995)], with time limits 25-30sec.

The characterisation of the fluidity was done by the comparison of the recorded time of the efflux with the ones proposed by the test descriptions. The efflux time for the ASTM cone was 6m 30s while for the Marsh cone it was 4m 25s (Figure 3.8). Despite the fact that those values were far from the recommended ones, since the instructions of the company producing the grout were followed correctly the injection process should continue. The tests were repeated later with almost similar results, thus the initial time results were kept for the characterization of the rheological properties.
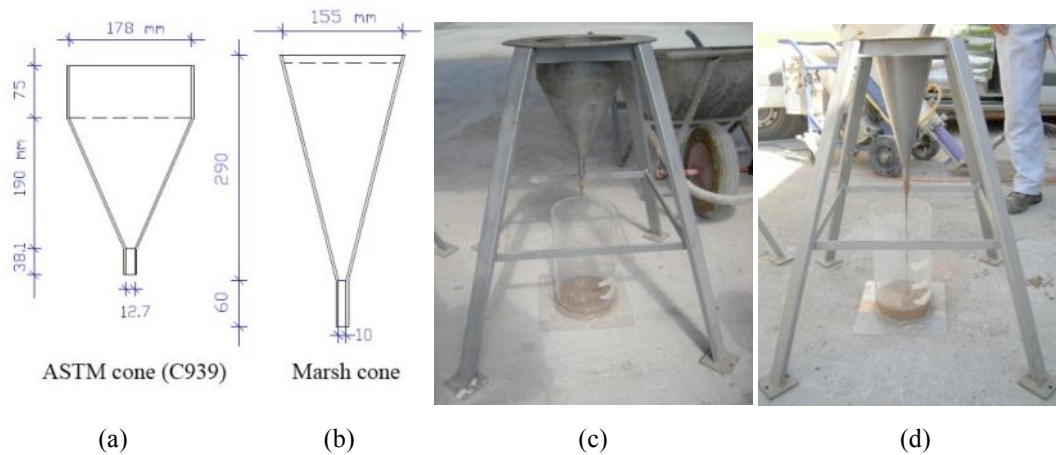
Figure 3.8: (a),(c) ASTM cone; (b),(d) Marsh cone.

Stability

The homogeneity of the grout can be evaluated by the observation of the segregation and the bleed water on the surface of the hydraulic lime. The mixture was put into two transparent graded vessels according to the ASTM standard C940 [(1989)] and it was left to settle for 30 minutes. The bleeding was found to be low with only one very thin layer of water to have formed on the surface and the segregation to be around % of the total height. The bleeding and the segregation need to conform to the requirements of the ASTM Standards C937-89 which allow a minimum bleeding but without any segregation.

Injectability

The injectability tests were carried out in plastic moulds filled with stone fragments. The injection was proceeded from a point near the bottom of the mould and the required time for the filling of the tube with grout was recorded for each specimen. The tests were done in moulds of full scale and 2:3 scale with aggregates of dimensions 1-7 cm and 0.66-4.66 cm respectively. A visual investigation is able to give a first estimation of the success of the injection technique which will mean complete filling of the voids. The specimens, after the grout hardening, were later

52

used for the determination of the mechanical characteristics of the grouted internal leaf.

Figure 3.9: Injectibility test and preparation of the cylinders.

3.4 Characterisation of materials and composite elements properties

The tests took place in the Laboratory of the Department of Constructions and Transports of the University of Padova.

3.4.1 Stone characterisation

For the construction of the walls were used three types of stone taken from the quarry of Cugnano in Belluno. For simplicity the three types were defined as red stone, white irregular shape stone and white regular shape stone. The stone specimens were subjected to tests according to the following standards:

UNI EN 1926 [(2007)]: Determination of the compression strength from uniaxial compression.

UNI EN 12372 [(2007)]: Determination of the flexural strength.

UNI EN 14580 [(2005)]: Determination of the Young's modulus of elasticity.

53

UNI EN 1936 [(2007)]; UNI EN 772-4 [(2001)]: Determination of the apparent volumic mass and of the open porosity.

Table 3.2: Characteristics of the stones (220 days).

	Stone typology					
	Red		White regular		White irregular	
Compression strength	93.4	N/mm^2	163.8	N/mm^2	-	N/mm^2
Flexural strength	17.3	N/mm^2	16.079	N/mm^2	5.755	N/mm^2
Young's modulus	54473	N/mm^2	68021	N/mm^2	-	N/mm^2
Apparent volumic mass	2670	Kg/m^2	2660	Kg/m^2	2720	Kg/m^2
Open porosity	1.29	%	1.41	%	1.79	%
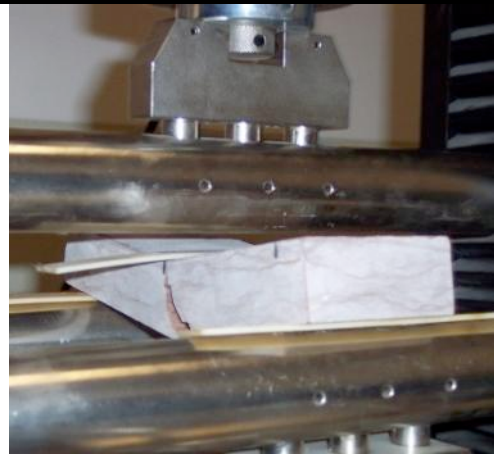
(a)   (b)

Figure 3.10: (a) compression test of cubic specimen of red stone; (b) flexural strength test of white stone

3.4.2 Mortar T30V characterisation

The mortar T30V is produced according to the UNI EN 998-1 referring to mortars suitable for masonry works. The maximum size of the aggregates in the mortar was 4mm. The tests were carried out according to the following standards:

UNI EN 1015-11 [(2007)]: Determination of the compressive and flexural strength.

UNI 6556 [(1976)]: Determination of the Young's modulus of elasticity and Poisson's ratio.

54

Table 3.3: Mechanical characteristics of the mortar (220 days).

Mortar T30V		
Compression strength	3.57	N/mm^2
Flexural strength	1.44	N/mm^2
Young's modulus	4645	N/mm^2
Poisson's ratio	0.265	

(a)	(b)	(c)
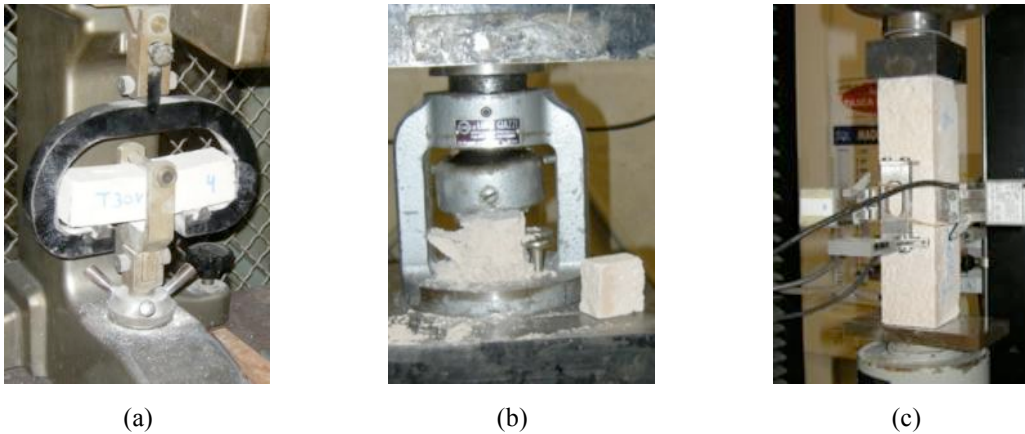
Figure 3.11: Tests for: (a) the flexural strength; (b) the compression strength; (c) the Young's modulus and Poisson's ratio.

3.4.3 Grout Fenix-B characterisation

The same tests of the mortar, UNI EN 1015-11 and UNI 6556, were used for the characterisation of the grout mechanical properties. The results are presented in the Table 3.4.

Table 3.4: Mechanical characteristics of the mortar (40 days).

Grout Fenix-B		
Compression strength	12.48	N/mm^2
Flexural strength	2.75	N/mm^2
Young's modulus	7504	N/mm^2
Poisson's ratio	0.290	

55
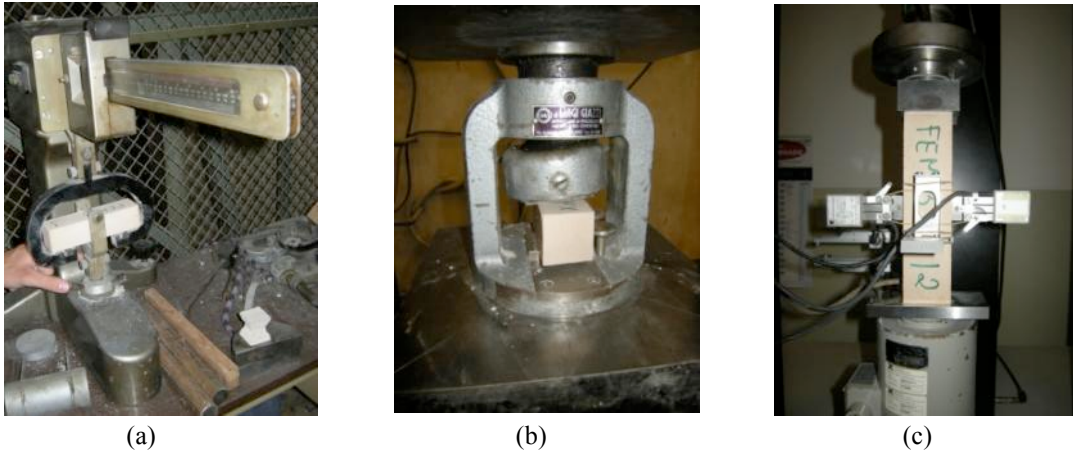
Figure 3.12: Tests for: (a) the flexural strength; (b) the compression strength; (c) the Young's modulus and Poisson's ratio.

3.4.4 Cylinders

The cylinders which were created during the injectability tests were tested for finding the mechanical properties of the grouted infill material. After the removal of the plastic moulds and the levelling of the surfaces, the cylinders were tested according to:

UNI EN 12390-3 [(2003)]: For determination of the compression strength via uniaxial compression test.

UNI EN 12390-6 [(2002)]: For determination of the flexural strength via indirect tensile test (Brazilian test).

UNI 6556 [(1976)]: Determination of the Young's modulus of elasticity.

Table 3.5: Mechanical characteristics of the mortar (40 days).

	Grouted infill material			
	1:1 scale		2:3 scale	
Compression strength	3.44	N/mm^2	3.81	N/mm^2
Flexural strength	0.50	N/mm^2	0.47	N/mm^2
Young's modulus	4150	N/mm^2	3614	N/mm^2
Density	1942	Kg/m^2	1808	Kg/m^2

Figure 3.14: Progress of the compression test for a grouted cylinder.
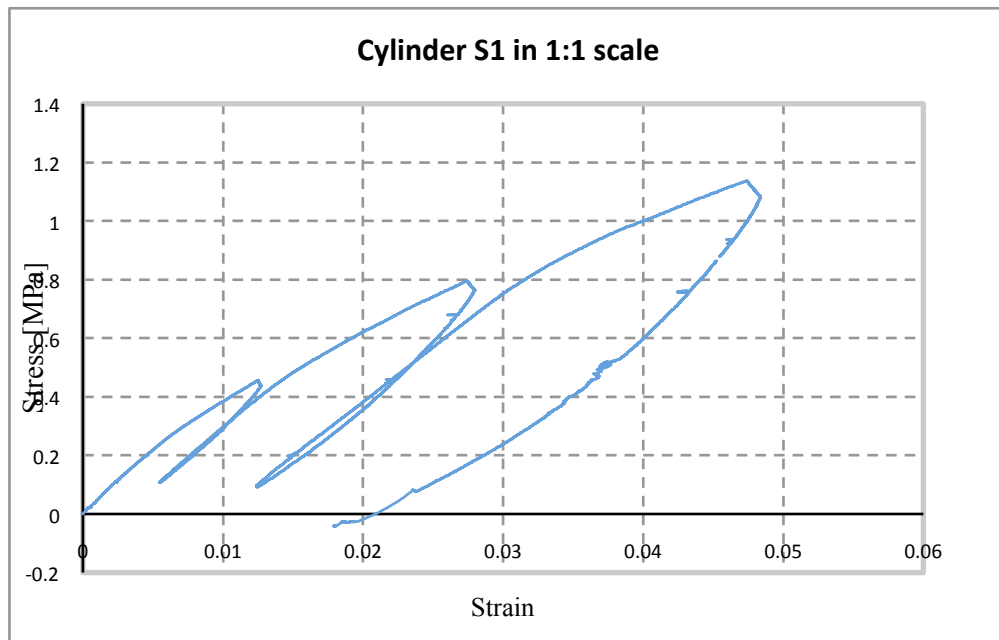
Figure 3.12: Determination of the Young's modulus of elasticity via the stress-deformation curve for the S1 cylinder in 1:1 scale.
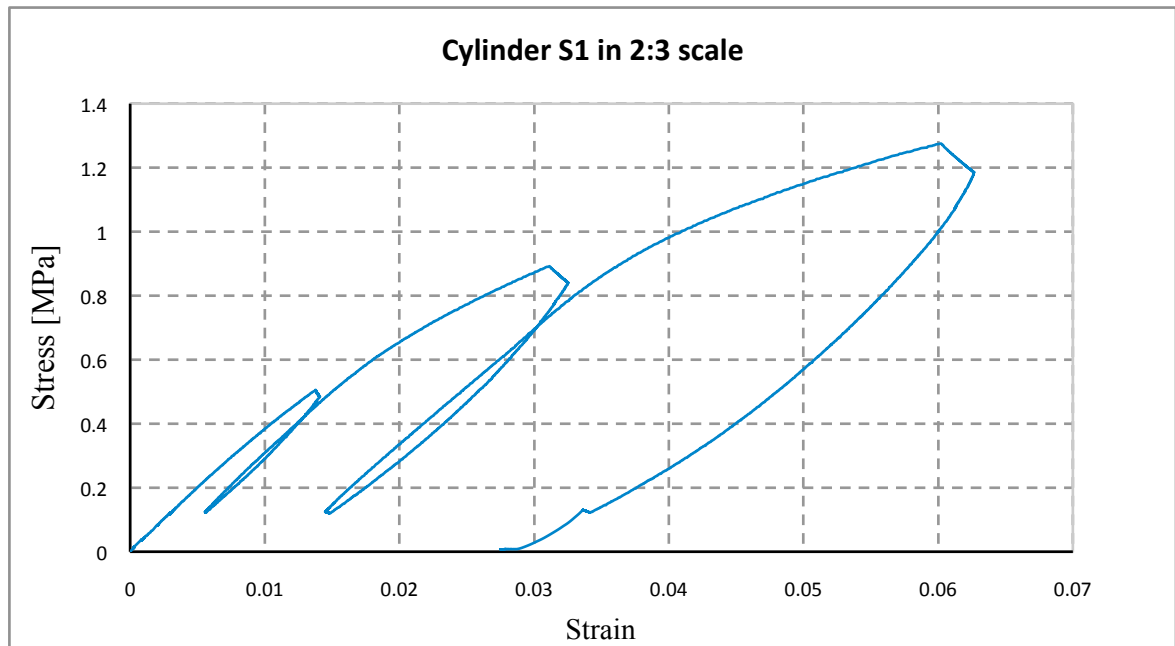
Figure 3.13: Determination of the Young's modulus of elasticity via the stress-deformation curve for the S1 cylinder in 2:3 scale.

| (a) | (b) | (c) |
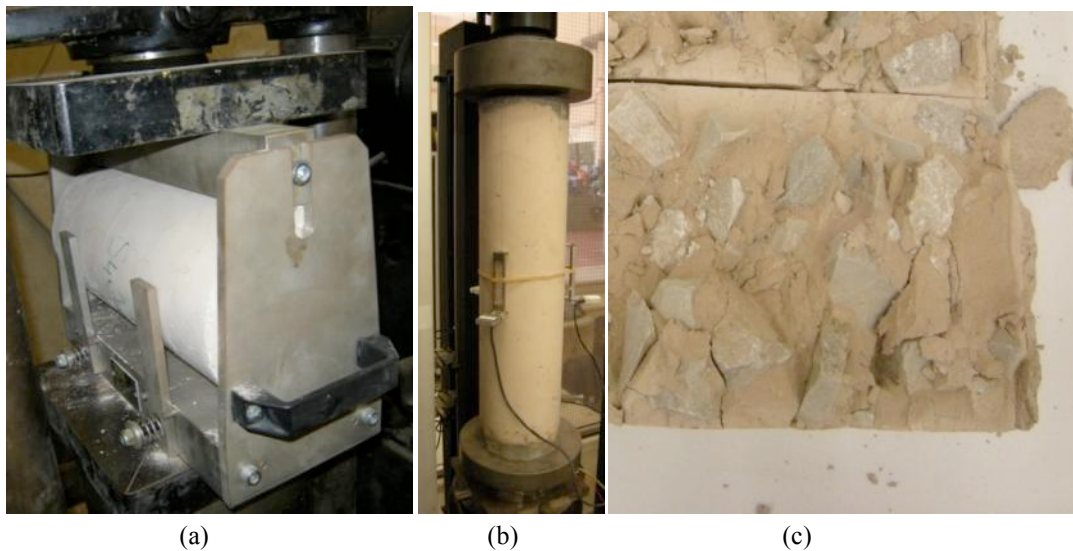
Figure 3.15: (a) Brazilian test; (b) Determination of the Young's modulus; (c) visual inspection of the section of visual investigation of the injectability.

3.5 Experimental results of the stone masonry walls

58

The experimental results of the monotonic and cyclic compression showed the high influence that the injection technique had on the resistance of the stone masonry wall panels. In the (Figure 3.15a) it can be shown that in the case of the monotonic compression tests the strength of both the walls in 1:1 and 2:3 scale was increased around 100% while the ductility of the injected walls in most of the cases is lower than the original. The same high influence of the injections can be also shown in the (Figure 3.16) where it is presented the enhanced behaviour under cyclic compression for walls in 1:1 and 2:3 scale. It needs to be pointed out that both for the monotonic and for the cyclic compression; the scale of the wall plays an important role in the influence of the strengthening, with the walls in 2:3 scale to appear higher increase of the compressive strength than the ones in 1:1 scale.

Another point that needs to be mentioned is the different behaviour of the same wall type between the monotonic and the cyclic compression tests. For all the walls the ultimate vertical strains are higher in the case of the monotonic tests (Figure 3.17).

Finally the, shear-compression test (Figure 3.18) which carried out on a 2:3 scale reinforced wall E have shown that the wall exhibited sufficient energy dissipation during the cyclic loading.
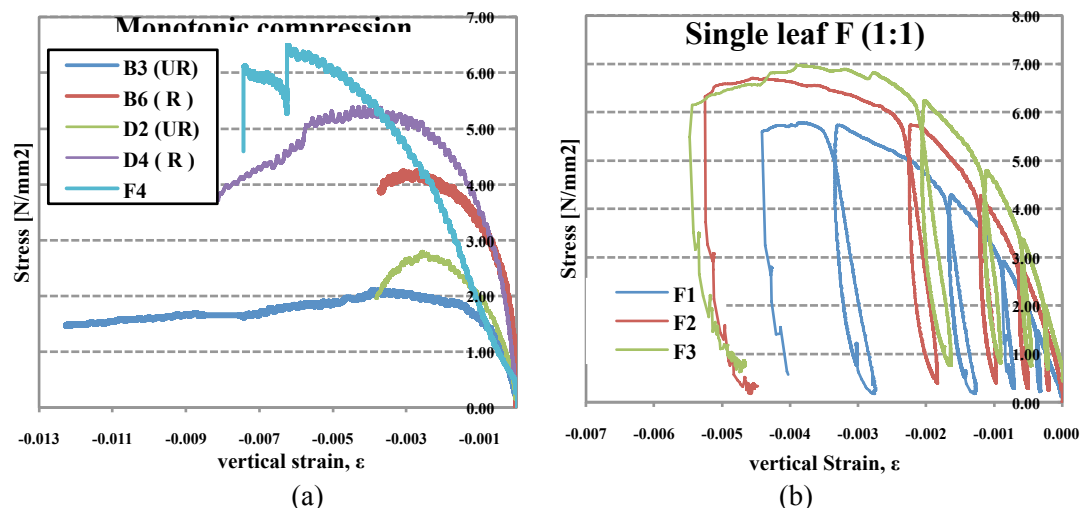
Figure 3.15: Stress-strain diagrams for: (a) behaviour under monotonic compression of all the wall types in original and injected conditions; (b) behaviour under cyclic compression of the single leaf wall F.
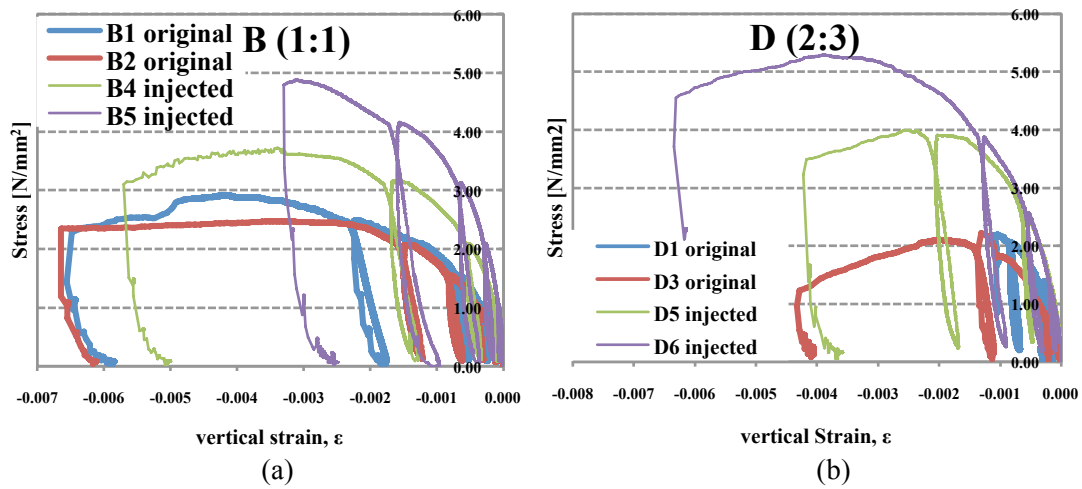
Figure 3.16: Comparison between the injected and original conditions under cyclic compression for: (a) the wall B in 1:1 scale; (b) the wall D in 2:3 scale.
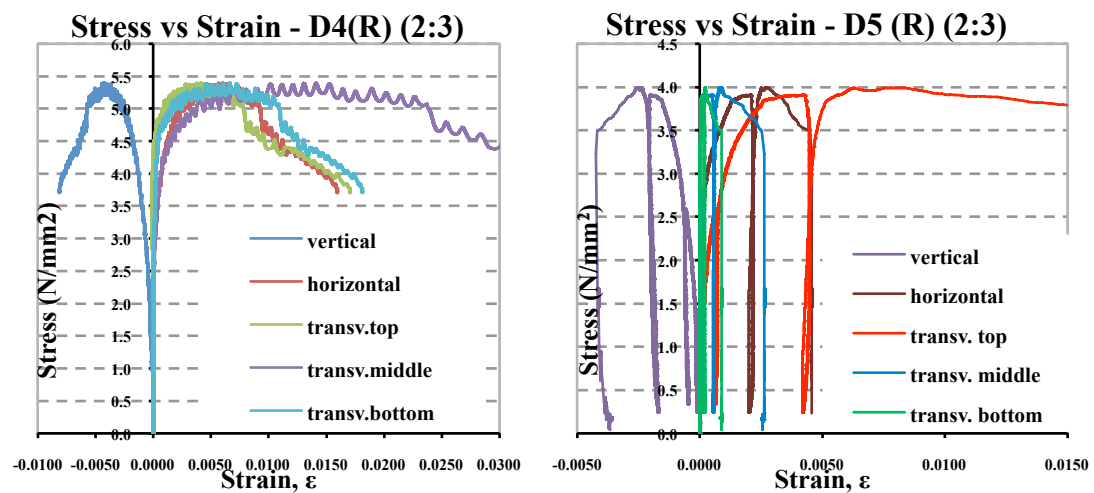
Figure 3.17: Stress-strain diagrams for different areas of strengthened walls D in 2:3 scale for: (a) monotonic compression; (b) cyclic compression.

60

Shear-Compression test- Reinforced wall E7 (2:3 scale)
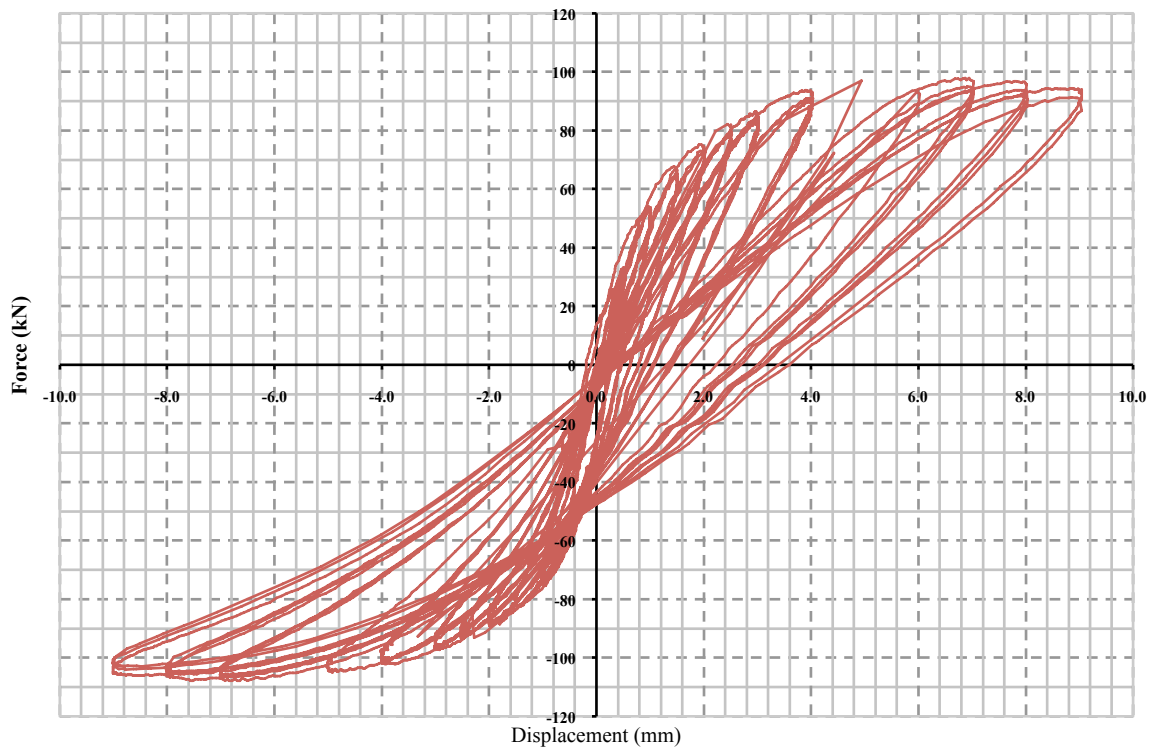
Figure 3.17: Force-displacement diagram for the shear-compression test of the reinforced wall E in 2:3 scale.

Chapter 4

Calibration of the numerical material behaviour curves

4.1 Introduction

The main scope of the work described in this chapter is the calibration of the numerical material behaviour curves using the previously described continuous damage model. For this calibration are used the UNIPD experimental campaign on stone masonry walls. In the results are included all the monotonic and the cyclic compression tests on injected and non injected three-leaf stone masonry walls with scale 1:1 and 2:3 and a single leaf wall in 1:1. It was also available one shear-compression test on a three-leaf (2:3) reinforced stone masonry wall. Parameters which were not possible to be calculated via the laboratory tests were based on the results of other analyses bibliographically available. The first approach of the calibration was to simulate the walls using a homogeneous and isotropic material capable of taking into account the joint behaviour of stone, mortar and consolidation material, but also the internal and external leaves and giving numerical results close to experimentally obtained ones. In this way low computational demands can be achieved opening the way for complex and large dimensions analyses. The simulation using a homogeneous material is considered to be a necessary first step which can be used for better understanding of the wall behaviour and for more advanced future calibration using different materials for the internal and external leaves and taking into account the interface between them.

4.2 Cast3M

The software which was used for the analyses is the Cast3M, a powerful code for solving partial differentials equations by the finite element method, developed by the Department of Modelisation of Sytems and Structures (DM2S) of the French Atomic Energy Commissariat (CEA). The software, having an integrated solver with pre- and post-processing, becomes an independent analysis tool.

The code is mainly focused on the solving of non-linear mechanical problems including plasticity, buckling, creep, seismic analysis, thermo-plasticity, post-buckling, fracture mechanics etc. Cast3M uses the high level macro-language GIBIANE which gives the user the ability to adapt or extend the GIBIANE code in order to address the needs of his analysis creating involving operators and creating new objects. Multiple and complex problems in 2D or 3D can be modelled with the use of a comprehensive library of structural finite elements (shell elements, beam elements, solid elements, joint elements etc) combined with a wide range of constitutive models for engineering materials like masonry, concrete, steel etc.

The damage model which was used is the already described model of Faria and Oliver [(1993)] which requires the calibration of eighteen mandatory parameters shown in the Table 4.1 in order to describe the real behaviour of the structure.

Table 4.1: Mandatory parameters for the calibration of the Faria and Oliver [(1993)] model in Cast3M.

	Parameter	Parameter
YOUN:	Young's modulus $-E$	Experimentally
NU :	Poisson's coefficient - v	Experimentally
RHO :	Density $-\rho$	Geometry
HLEN :	Effective length - l	Geometry
GVAL :	Tensile fracture energy - G_f	Bibliography
FTUL:	Tensile stress - f_0^+	Bibliography
REDC :	Drop factor for peak tensile stress - Δf_0^+	Bibliography
FC01:	Elastic limit compressive stress - $f_{0_{1D}}^-$	Experimentally
RT45 :	Equi-biaxial compressive ratio - $f_{0_{2D}}^- / f_{0_{1D}}^-$	Bibliography
FCU1 :	Compressive peak stress - f_u^-	Experimentally
STRU:	Ultimate limit strain - ε_u^-	Experimentally
EXTP:	Reference strain for plastic parameter - ε_p^-	Experimentally
STRP:	Reference stress for plastic parameter - σ_p^-	Experimentally

EXT1 :	Fitting point 1 (Strain) -	Experimentally
STR1:	Fitting point 1 (Stress) -	Experimentally
EXT2:	Fitting point 2 (Strain) -	Experimentally
STR2 :	Fitting point 2 (Stress) -	Experimentally
NCRI:	Tensile softening criteria (1-Exponencial / 2-	Bibliography

4.3 Sensitivity analysis

The sensitivity analysis took place in order to evaluate the influence of the different parameter on the calibrated numerical behaviour curves. The influence is shown on the alteration of the stress-strain diagrams depending on the variation of the under analysis parameter. Sensitivity analyses were carried out both for monotonic and for cyclic compression tests. The initial properties which were used are shown in the Table 4.2.

Table 4.2: Initial parameters for the sensitivity analysis

	Parameter	2:3 D(R) Monotonic	1:1 B(R) Cyclic
YOUN	Young's modulus (N/m²)	$5.69 \cdot 10^9$	$21.0 \cdot 10^9$
NU	Poisson's coefficient	0.25	0.25
RHO	Density (kg/m³)	2600	2600
HLEN	Effective length	Dens=0.05	Dens=0.05
GVAL	Tensile fracture energy (J)	50	50
FTUL	Tensile stress (N/m²)	$0.17 \cdot 10^6$	$0.17 \cdot 10^6$
REDC	Drop factor for peak tensile stress	1	1
FC01	Elastic limit compressive stress (N/m²)	$-1.8 \cdot 10^6$	$-0.35 \cdot 10^6$
RT45	Equi-biaxial Compressive Ratio	1	1
FCU1	Compressive peak stress (N/m²)	$-5.3 \cdot 10^6$	$-3.7 \cdot 10^6$
EXTU	Ultimate limit strain	-0.008	-0.0057
EXTP	Reference strain for plastic parameter	-0.054	-0.0008
STRP	Reference stress for plastic parameter	$-5.0 \cdot 10^6$	$-1.0 \cdot 10^6$
EXT1	Fitting point 1 (Strain)	-0.0032	-0.0020
STR1	Fitting point 1 (N/m²)	$-5.2 \cdot 10^6$	$-3.7 \cdot 10^6$
EXT2	Fitting point 2 (Strain)	-0.0076	-0.0052
STR2	Fitting point 2 (N/m²)	$-4.1 \cdot 10^6$	$-3.4 \cdot 10^6$
NCRI	Tensile softening criteria	1	1

4.3.1 Influencing parameters in compression

YOUN – Young's modulus of elasticity

This parameter defines the modulus of elasticity and it was selected in order the numerical behaviour curve to resemble the experimental results. The sensitivity analysis on this parameter has shown it can modify the rigidity of the material while keeping the fitting points (P1,P2) fixed. As it is shown in the Figure 4.1 the increase of the YOUN parameter gives the curve a slightly higher rigidity comparing to the initial one. In the same way, a slightly less rigid can occur by lowering the values of the modulus of elasticity.

Influence of the YOUN parameter - monotonic compression

Figure 4.1: Influence of the YOUN parameter on the rigidity for monotonic compression (initial value: YOUN=$5.69 \cdot 10^9$ N/m^2).
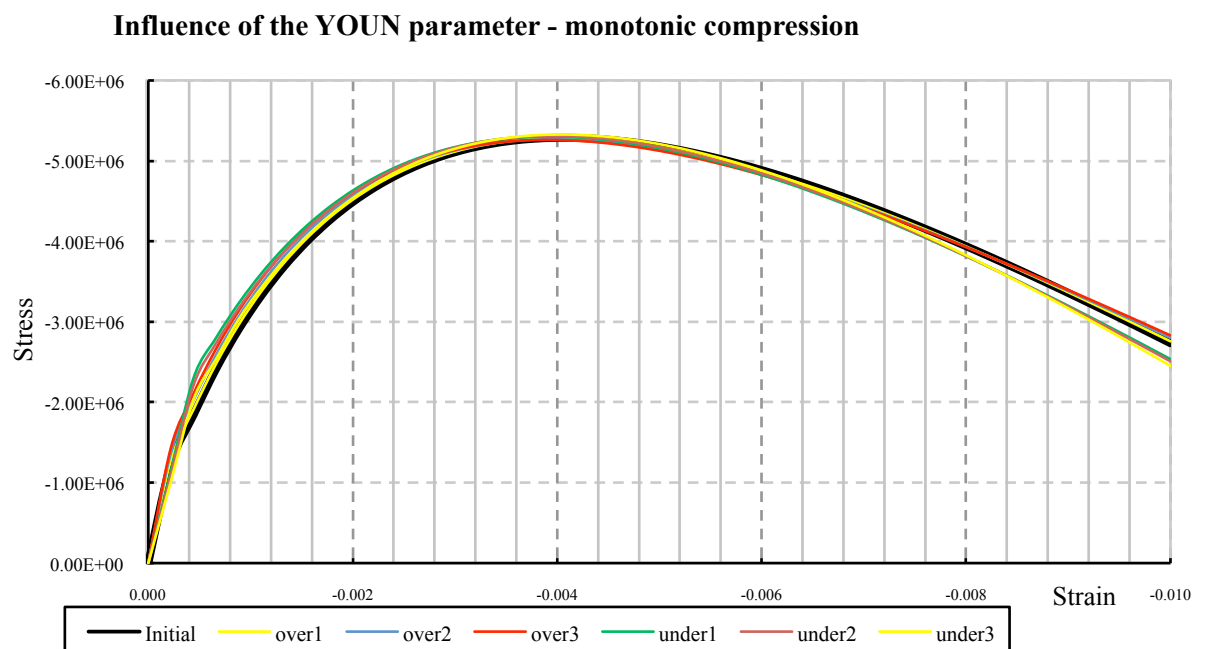
In a similar way is affected the curve by the YOUN parameter in the cyclic compression behaviour. Higher rigidity is achieved by higher YOUN values. In the Fugure 4.2 it can be observed the influence on the last part of the curve which is not close to the fixed fitting points P1 and P2.

Influence of the YOUN parameter - cyclic compression
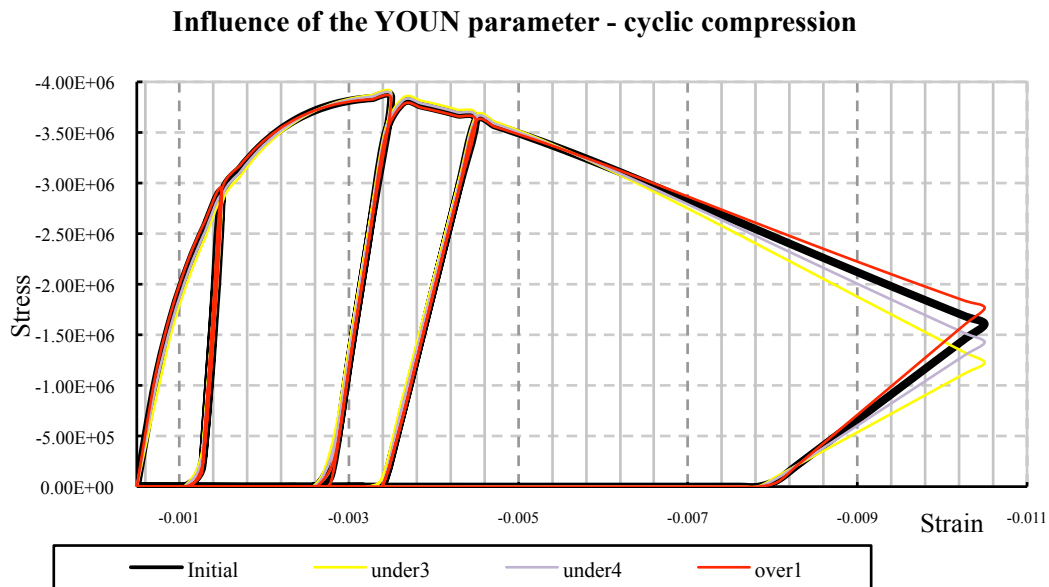
Figure 4.2: Influence of the YOUN parameter on the rigidity for cyclic compression (initial value: YOUN=$21.0 \cdot 10^9$ N/m^2).

The damage model implements two fitting points (P1,P2) using the parameters EXT1, EXT2, STR1 and STR2 as their coordinates for the strain and stress respectively. The influence of those is shown in the Figures 4.3, 4.4, 4.5 for monotonic and Figures 4.5, 4.6 for the cyclic compression and it is similar for both cases. It can be noticed that a mutual increase of the STR1 and STR2 can increase the peak compressive strength of the material while a mutual decrease can lower this peak point.

Influence of the STR1 and STR2 parameters for translation in the same direction - monotonic compression
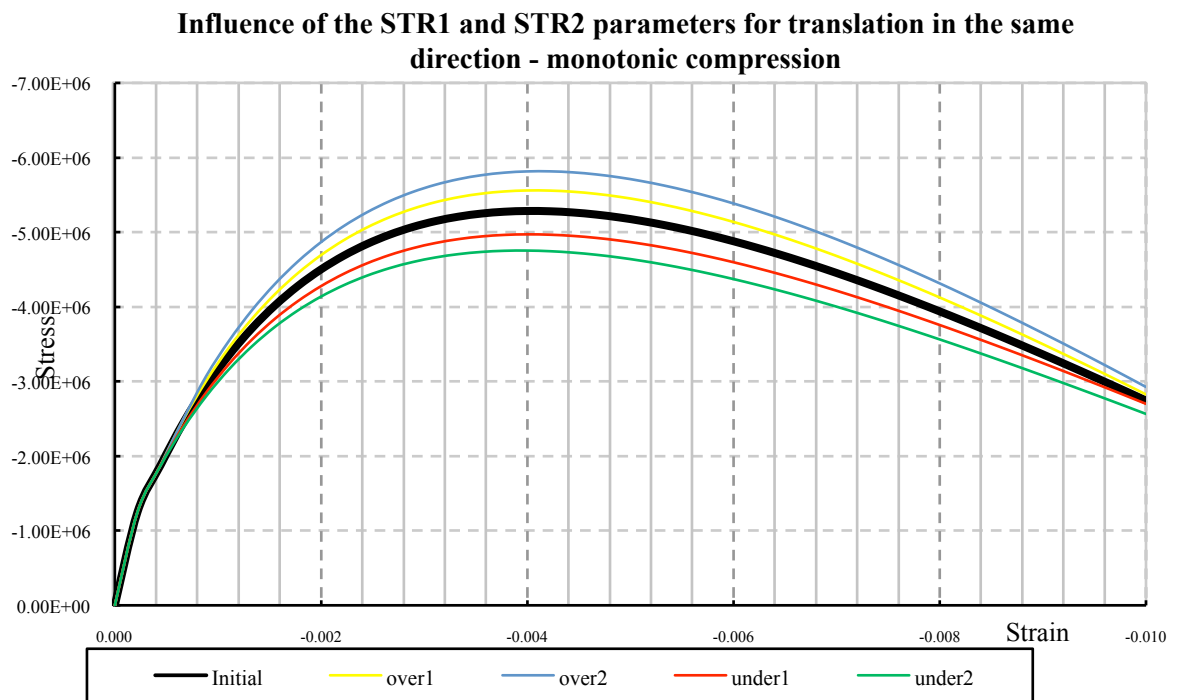
Figure 4.3: Influence of the STR1 and STR2 parameters on the compressive strength of the material under monotonic compression (initial values:STR1=-5.2·10^9 N/m^2; STR2=-4.1·10^6 N/m^2).

Influence of the EXT1 and EXT2 parameters for translation in the same direction - monotonic compression
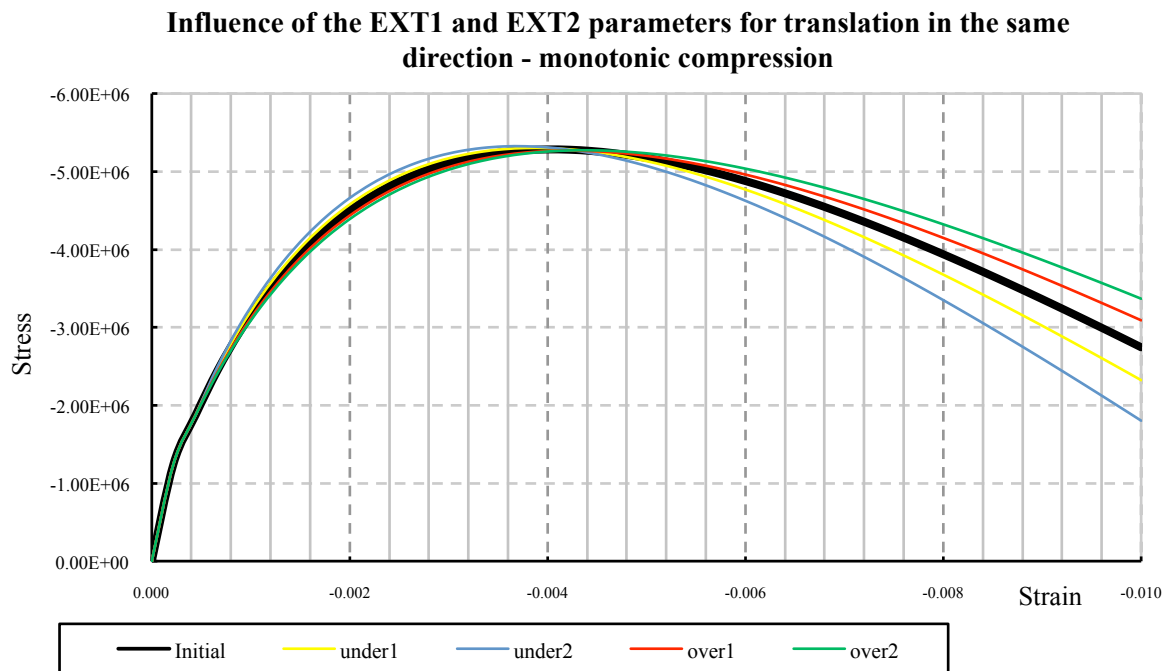
Figure 4.4: Influence of the EXT1 and EXT2 parameters (translation in the same direction) on the compressive strength of the material under monotonic compression (initial values: EXT1=-0.0032; EXT2=-0.0076).

67
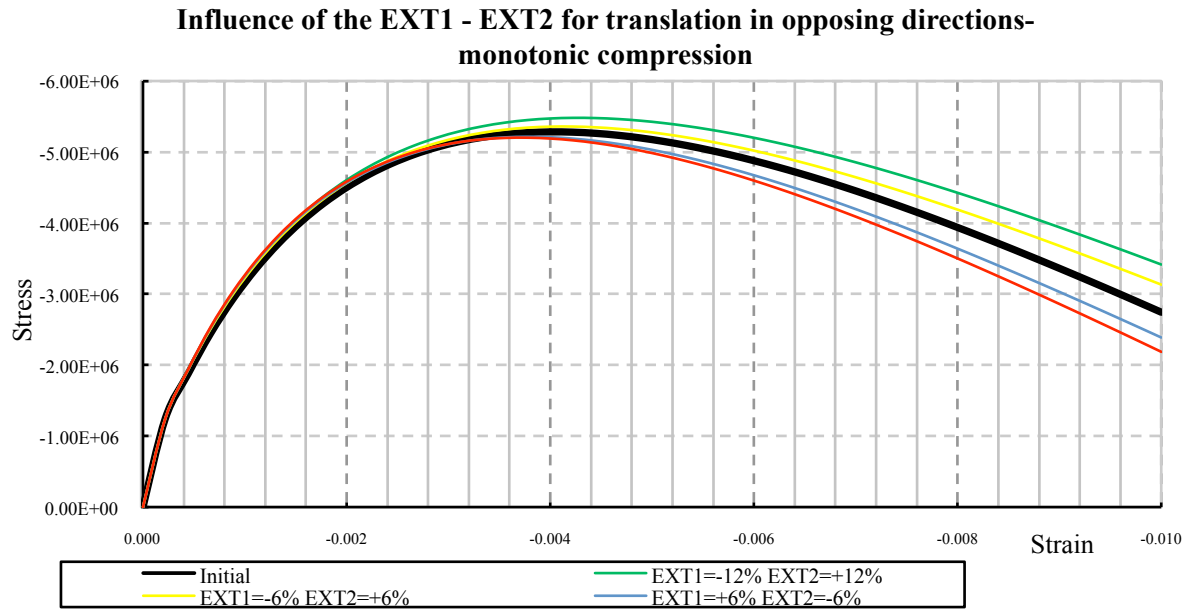
Figure 4.5: Influence of the EXT1 and EXT2 parameters (translation in opposing directions) on the compressive strength of the material under monotonic compression (initial values: EXT1=-0.0032; EXT2=-0.0076).
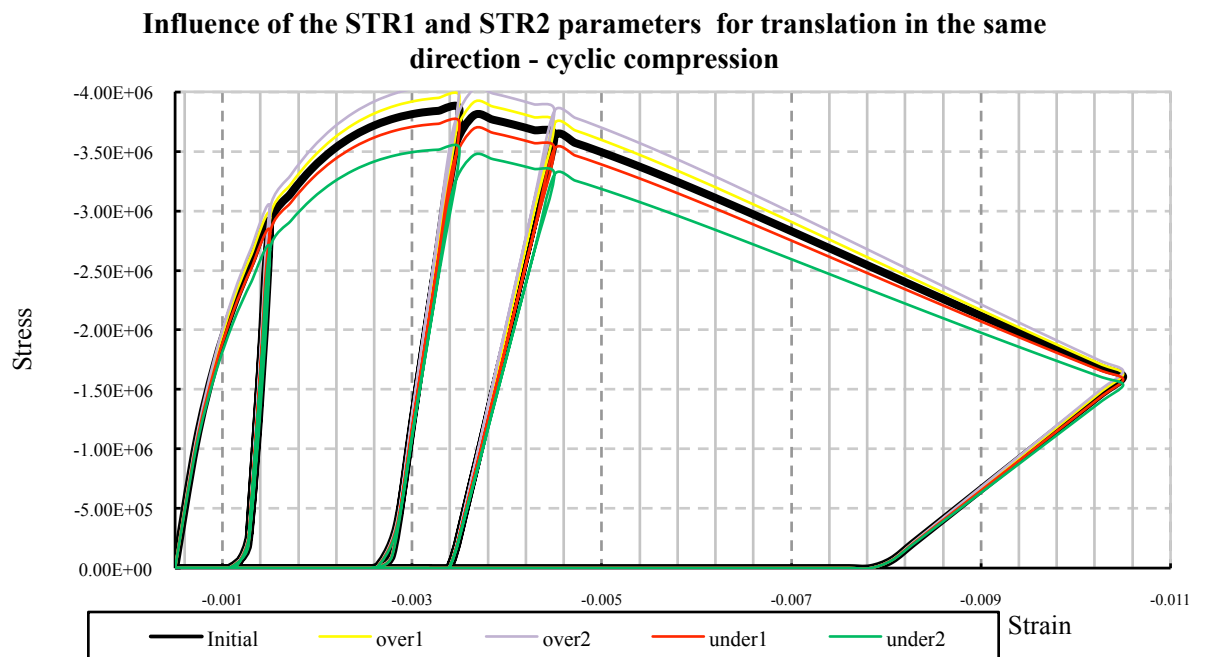
Figure 4.6: Influence of the STR1 and STR2 parameters on the compressive strength of the material under cyclic compression (initial values:STR1=-3.7·10^9 N/m^2; STR2=-3.4·10^6 N/m^2).

68
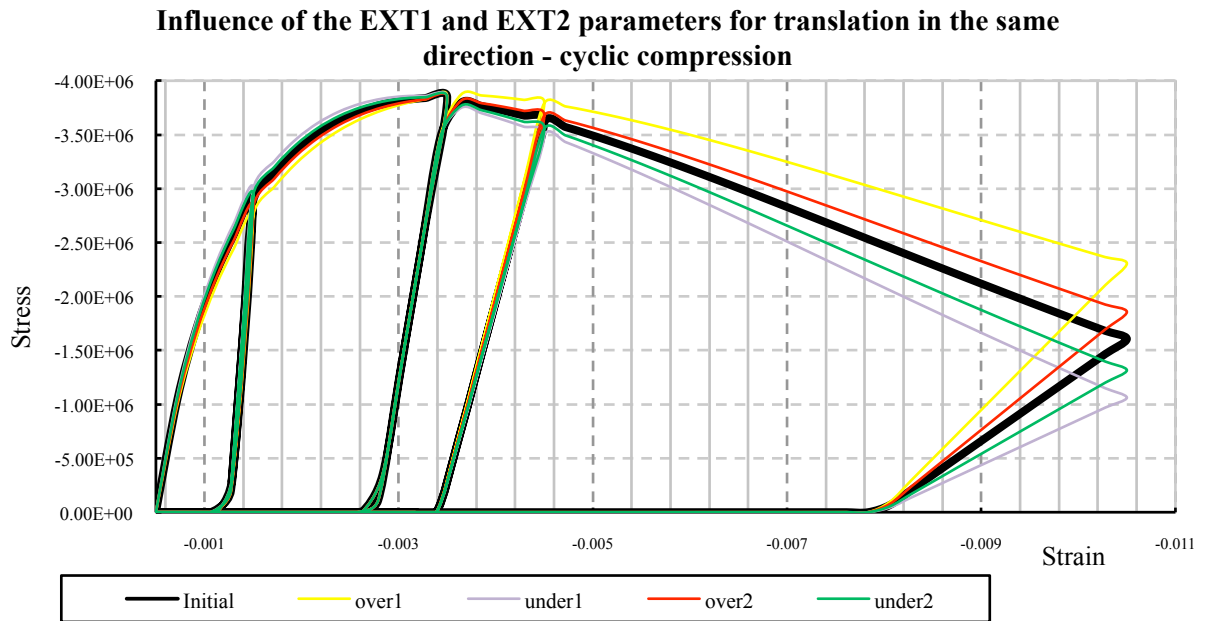
Figure 4.7: Influence of the EXT1 and EXT2 parameters on the compressive strength of the material under monotonic compression (initial values: EXT1=-0.0020; EXT2=-0.0052).

FCU1- Compressive peak stress

Although the FCU1 defines the compressive strength of the material, this parameter does not affect the peak point of the numerical behaviour curve. The influence of the FCU1 parameter can mainly be noticed on the inclination of the unloading-loading cycles since for the calculation of those cycles it is used by the damage model along with the 'β' parameter. However, due to the fact that the FCU1 is used by the damage model for a plethora of different calculations, it is crucial the FCU1 to take the value of the desired peak stress point and not to be used for the calibration of the unloading-loading segments.

69

Influence of the FCU1 parameter- cyclic compression
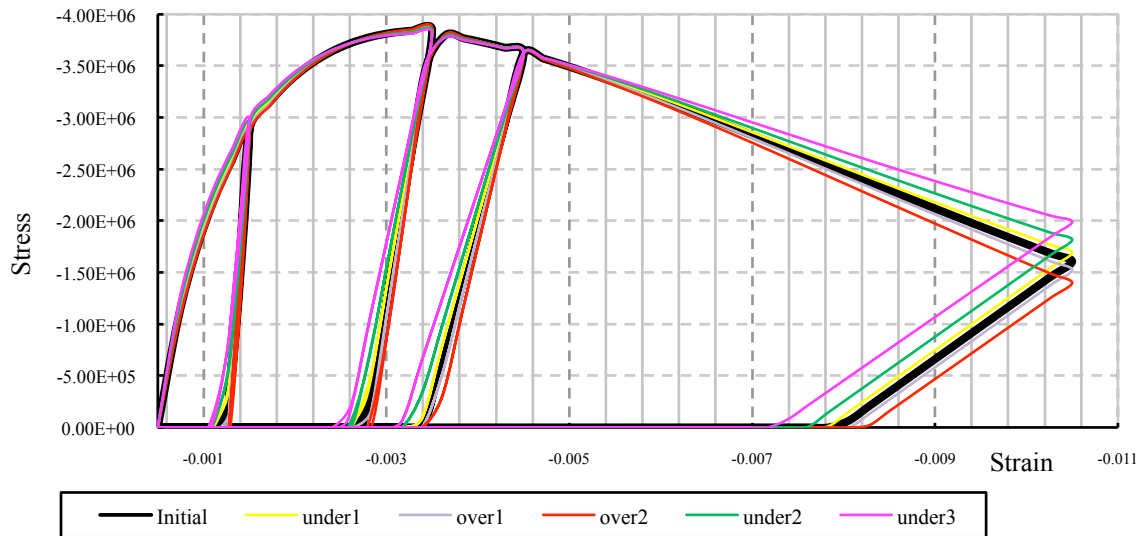
Figure 4.8: Influence of the FCU1 parameter on the numerical behaviour curve under monotonic compression (initial value: EXT1=-0.0020; EXT2=-0.0052).

4.3.2 Influencing parameters in tension

NCRI – Tensile Softening Criteria

This parameter describes the softening segment of the tensile fracture curve. It can be exponential softening (value 1) or to be considered a linear softening (value 2) (Figure 4.9a, 4.9b). For the sensitivity analysis the parameter is kept constant in order to have an exponential softening behaviour.

REDC – Drop factor for Peak Tensile Stress - Δf_0^+

70

This parameter defines the behaviour of the material after the peak tensile stress. A non zero value indicates a linear softening connecting the peak point with the maximum tensile strain. Any non-zero Δf_0^+ indicates a local vertical drop of the stress by this value followed by linear softening as it is shown in the Figure 8888c. For the sensitivity analysis it was used exponential softening, thus the drop factor takes a zero value.
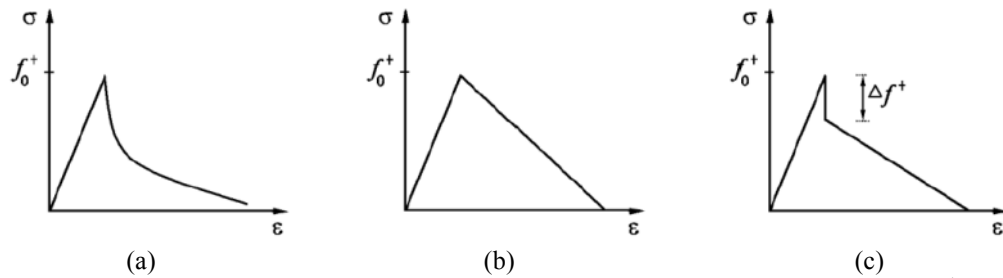
Figure 4.9: (a) exponential softening criteria; (b) linear softening criteria with zero Δf_0^+ (c) linear softening criteria with non-zero Δf_0^+.

GVAL – Tensile fracture energy

The influence of the tensile fracture energy which is defined as the area under the line which describes the softening of the material after the tensile fracture was also part of the sensitivity analysis. In the Figure 4.10 it is shown that the lower values the GVAL parameter takes the more fragile the fracture due to tension is. On the contrary, higher of tensile fracture energy can give the material a more ductile behaviour after the reaching of the tensile threshold capacity.

Influence of the GVAL parameter in tension
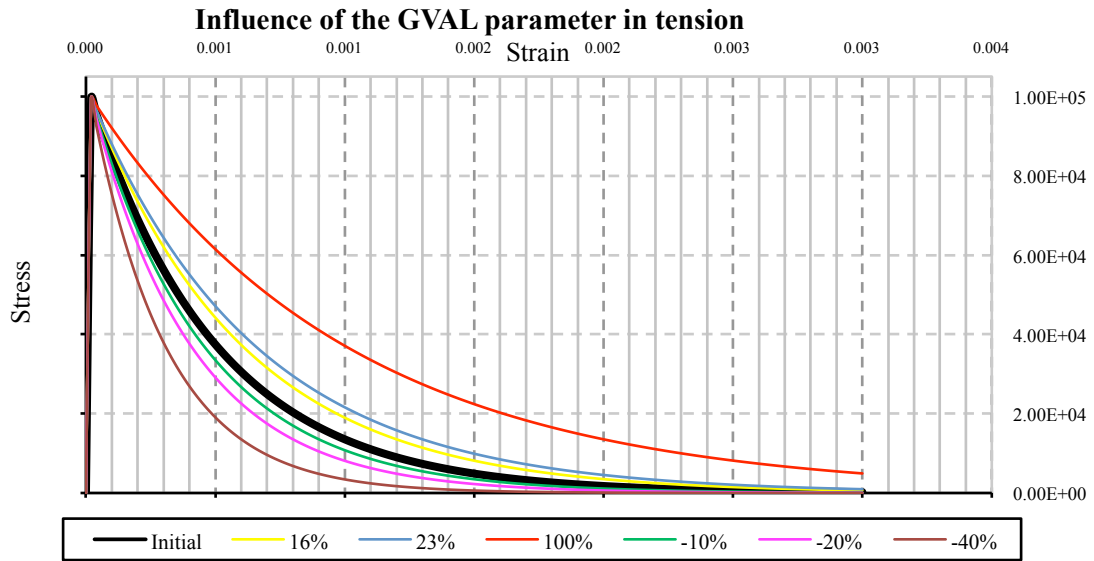
Figure 4.10: Influence of the GVAL parameter on the tensile fracture (initial value: GVAL=50J).

FTUL – Tensile strength

The influence of the FTUL parameter is shown in the Figure 4.11 where it can be observed the different peak tensile stress point for the different FTUL values keeping the tensile fracture energy constant.

Influence of the FTUL parameter
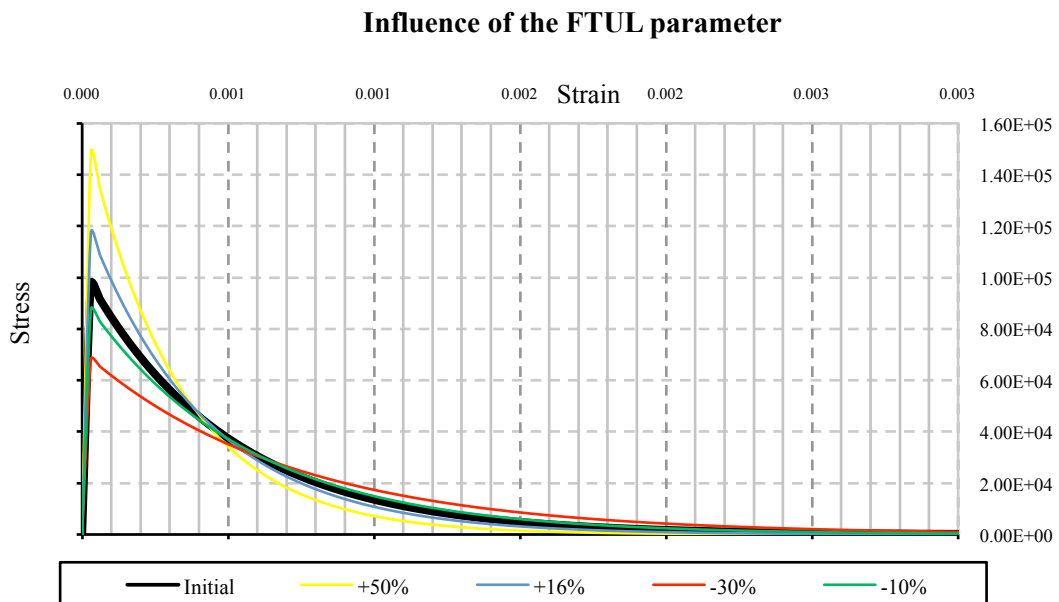
Figure 4.12: Influence of the FTUL parameter on the tensile fracture
(initial value: FTUL=$0.1 \cdot 10^{6}$ N/m^{2}).

Influence on the internal parameter β

The 'β' parameter is responsible for the inclination of the unloading-loading segments of the numerical behaviour curve. This internal parameter is calculated with the use of the YOUN, EXTP, STRP, FCU1 and FC01 as it is shown by its equation:

$$\beta = \frac{\left(E\varepsilon_p - \sigma_p\right)f_u^-}{\left(E\varepsilon_p - f_0^-\right)\left(\sigma_p + f_u^-\right)}$$

For the sensitivity analysis the FC01, FCU1 and YOUN were proportionally increased or decreased with the extreme values to differ around 15% from the initial ones. The EXTP and STRP are differenT combinations for points located on the non linear segment of the behaviour.

It is shown that the most effective way to manipulate the 'β' parameter is by the moving of the EXTP and STRP coordinates in different positions along the curve. Nevertheless, it has to be mentioned that there is an upper bound on the influence of the EXTP and STRP on 'β'. If a greater 'β' value is desired, the combination of EXTP and STRP has to be moved on a point which is not placed on the numerical behaviour curve.
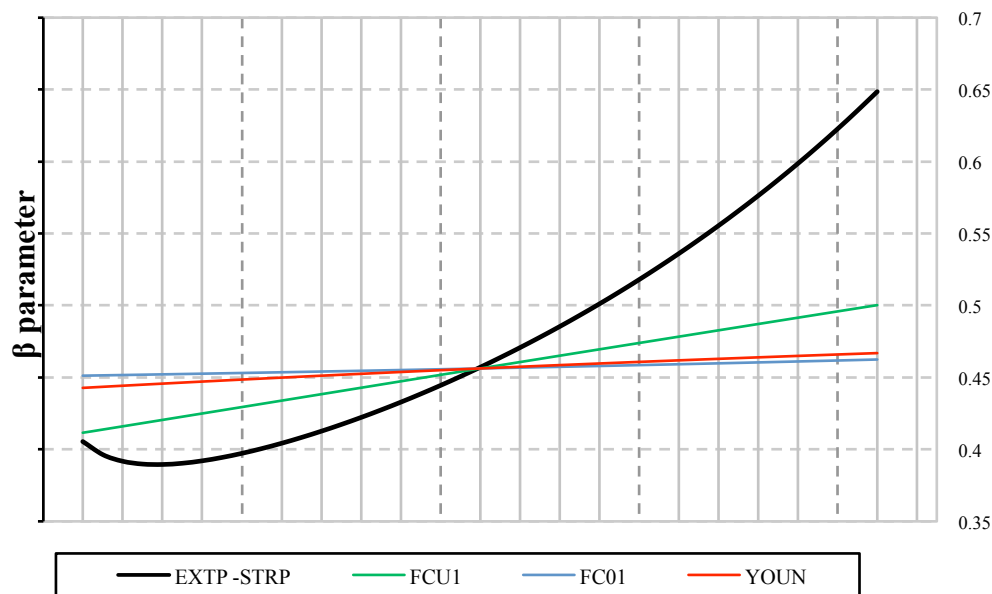
Figure 4.13: Influence of multiple parameters on the internal parameter 'β'
(initial values: FCU1=5.3·10^{6}N/m^2; FC01=1.8·10^{6}N/m^2; YOUN=5.69·10^{9}N/m^2).

73

4.4 Calibration of the behaviour curves

4.4.1 Calibration based on the monotonic and cyclic compression tests

The calibration of the curves was realised based on the results of both the monotonic and the cyclic compressive tests which were carried out for every wall type considering an homogeneous material for the masonry body. Although the material has in fact the same properties in both of the testing types, its behaviour is different and highly affected by the loading and unloading cycles. Thus, it was inevitable to calibrate every material twice, with different parameters for monotonic and cyclic compression.

The majority of the parameters were taken from the experimental result. The Poisson's ratio (NU) was calculated for the load corresponding to the 40% of the maximum load and it was taken from the average results of the transducers located on the main face of the walls. The compressive peak stress (FCU1) and the ultimate strain (EXTU) were also obtained by the stress-strain diagrams of the tested panels. In the case of the cyclic compression where more than one experimental curve were available it were considered average values.

The used constitutive law uses two fitting points (P1,P2) which are located on the desired curve in order to make possible its reproduction. Extent parametric analysis were carried out considering different combinations of those points (EXT1,EXT2,STR1,STR2) until the selection of the curve which were fitting the experimental results in the best possible way. The behaviour of the material during the unloading and the loading cycles is calibrated via the reference strain (EXTP) and stress (STRP) plastic parameters. In the case of the monotonic loading condition where the unloading and loading cycles are not simulated, this stress and strain was selected to be a point on the plastic part of the experimental curve. The calibration of those plastic parameters for the cyclic compression model was a more complex procedure. Being the stone masonry a very inhomogeneous material, it appears behaviour with high plastic strains during the unloading and loading cycles which were able to be sufficiently captured with the use of the current constitutive law. The

74

EXTP and STRP are connected with the calculation of the 'β' which is an internal parameter and used for calculating the remaining strains (for β=0 the behaviour is totally elastic). The parameter 'β' is also described in the following section of the sensitivity analysis and it can be found from the equation:

$$\beta = \frac{\left(E\varepsilon_p - \sigma_p\right)f_u^-}{\left(E\varepsilon_p - f_0^-\right)\left(\sigma_p + f_u^-\right)}$$

The only unloading segments which were not reproduced sufficiently are the ones at the ultimate strain. Due to the highly non linearity of the material characterized by the formation of big cracks that lead to energy dissipation incapable of being realistically reproduced with this type of models.

Regarding the Young's modulus of elasticity (YOUN), two very different approaches were followed. In the case of the monotonic compression model, the used Young's modulus is the one corresponding to the range 10%-30% of the compressive strength. This approach was not able to be followed for the cyclic compression models because the unloading-loading cycles were not possible to be represented in a realistic way with this modulus of elasticity. After a parametric analysis on the effect of the Young's modulus, it was found that the value which is able to reproduce the experimental behaviour of the material was the average inclination of the unloading-loading cycles. The value which was adopted for every wall type corresponds to the average modulus of elasticity taken from the unloading-loading cycles excluding the ones very close to the low stress domain which give very high values. The only exception of the above was the single leaf wall F which was calibrated in both of the cases with the rule of 10%-30% modulus of elasticity.

The elastic limit stress (FC01) was also selected in a different way for each of the two loading conditions. For the monotonic compression model the elastic limit stress was taken up to the 30% percent of the compressive strength that is also the value for which the Young's modulus was calculated. For the cyclic compression test where the modulus of elasticity has significantly higher values the limit elastic stress had to take lower values. With this constitutive law, a zero limit for the elastic stress was found to give results which represent the experimental behaviour very well. Nevertheless, this

75

would have a negative effect on the computational cost in a time history analysis where the model would enter the non elastic domain even for very low load. Aiming to have a compromising solution between the reality and the computational cost it was selected the limit elastic stress to correspond to the 10%-20% of the peak compressive stress.

The parameters which were found via bibliographic research include the tensile fracture energy (GVAL), the tensile softening criteria and the tensile strength. According to Lourenço (1996) for the tensile fracture energy a value between 10-100 J is considered to be plausible and thus it was selected the average value of 50J. Moreover, the exponential softening behaviour (NCRI=1) with zero drop factor (REDC) is the one which describes the masonry behaviour in the most realistic way. A tensile strength of 0.07MPa and 0.17MPa was adopted for the unstrengthened and strengthened walls respectively according to the [CIRCOLARE (2009)]. Finally for the equi-biaxial compressive ratio (RT45) was adopted a value equal to 1.
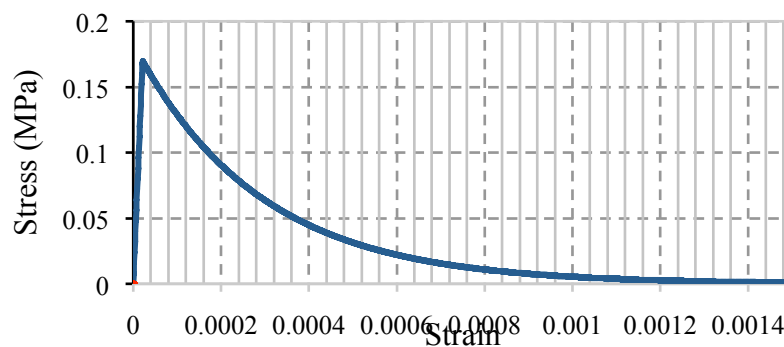
Figure 4.14: Tensile fracture with fracture energy 50J, tensile strength 0.17MPa and exponential softening criteria.

The density (DENS) of the material was calculated from the known geometry of the samples taking into account the specific weight of the constituent materials and the percentage of voids. Finally, the effective length parameter (HLEN) depends on the geometry of the finite element model which will be used and more specifically from the size of every finite element.

The values of all the used parameters for the monotonic and for the cyclic compression models are shown in the Table 4.1 and Table 4.2 respectively followed experimental and calibrated curves for each wall type.

76

Monotonic tests

Table 4.1: Parameter values for the monotonic compression models.

	Parameter	1:1 B(UR)	1:1 B(R)	2:3 D(UR)	2:3 D(R)	1:1 F
YOUN	Young's modulus (N/m^2)	$3.18 \cdot 10^9$	$8.0 \cdot 10^9$	$3.25 \cdot 10^9$	$5.69 \cdot 10^9$	$2.84 \cdot 10^9$
NU	Poisson's coefficient	0.20	0.25	0.25	0.25	0.25
RHO	Density (kg/m^3)	2600	2600	2600	2600	3200
HLEN	Effective length	Dens=0.05	Dens=0.05	Dens=0.05	Dens=0.05	Dens=0.05
GVAL	Tensile fracture energy (J)	50	50	50	50	50
FTUL	Tensile stress (N/m^2)	$0.07 \cdot 10^6$	$0.17 \cdot 10^6$	$0.07 \cdot 10^6$	$0.17 \cdot 10^6$	$0.17 \cdot 10^6$
REDC	Drop factor for peak tensile stress	0	0	0	0	0
FC01	Elastic limit compressive stress (N/m^2)	$-0.6 \cdot 10^6$	$-1.5 \cdot 10^6$	$-0.84 \cdot 10^6$	$-1.8 \cdot 10^6$	$-1.8 \cdot 10^6$
RT45	Equi-biaxial Compressive Ratio	1	1	1	1	1
FCU1	Compressive peak stress (N/m^2)	$-2.1 \cdot 10^6$	$-4.3 \cdot 10^6$	$-2.75 \cdot 10^6$	$-5.3 \cdot 10^6$	$-6.7 \cdot 10^6$
EXTU	Ultimate limit strain	-0.011	-0.0025	-0.0038	-0.008	-0.012
EXTP	Reference strain for plastic parameter	-0.002	-0.0027	-0.0032	-0.0054	-0.012
STRP	Reference stress for plastic parameter	$-2.5 \cdot 10^6$	$-3.95 \cdot 10^6$	$-2.5 \cdot 10^6$	$-5.0 \cdot 10^6$	$-4.2 \cdot 10^6$
EXT1	Fitting point 1 (Strain)	-0.0034	-0.0018	-0.0022	-0.0032	-0.006
STR1	Fitting point 1 (N/m^2)	$-2 \cdot 10^6$	$-4.0 \cdot 10^6$	$-2.66 \cdot 10^6$	$-5.2 \cdot 10^6$	$-6.6 \cdot 10^6$
EXT2	Fitting p int 2 (Strain)	-0.0052	-0.0027	-0.0032	-0.0076	-0.0018
STR2	Fitting point 2 (N/m^2)	$-2.5 \cdot 10^6$	$-3.9 \cdot 10^6$	$-2.5 \cdot 10^6$	$-4.1 \cdot 10^6$	$-5.5 \cdot 10^6$
NCRI	Tensile softening criteria	1	1	1	1	1

Wall B Unreinforced (1:1)- Behaviour curve for monotonic compression

77
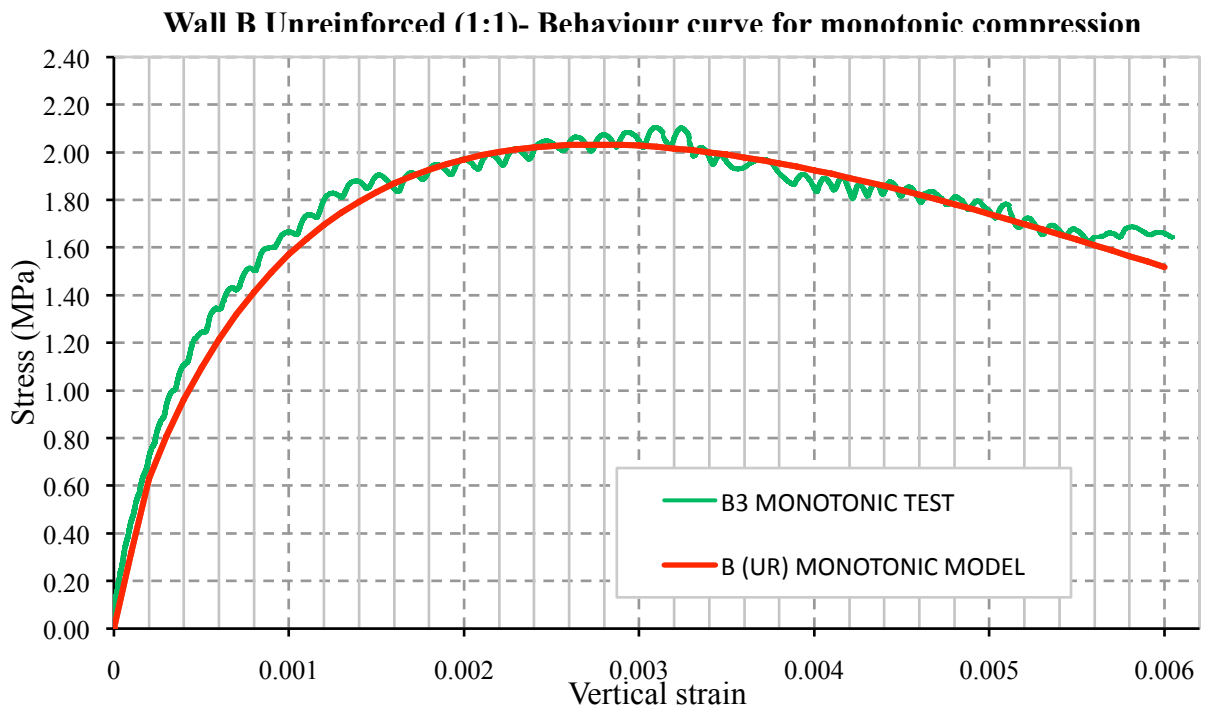
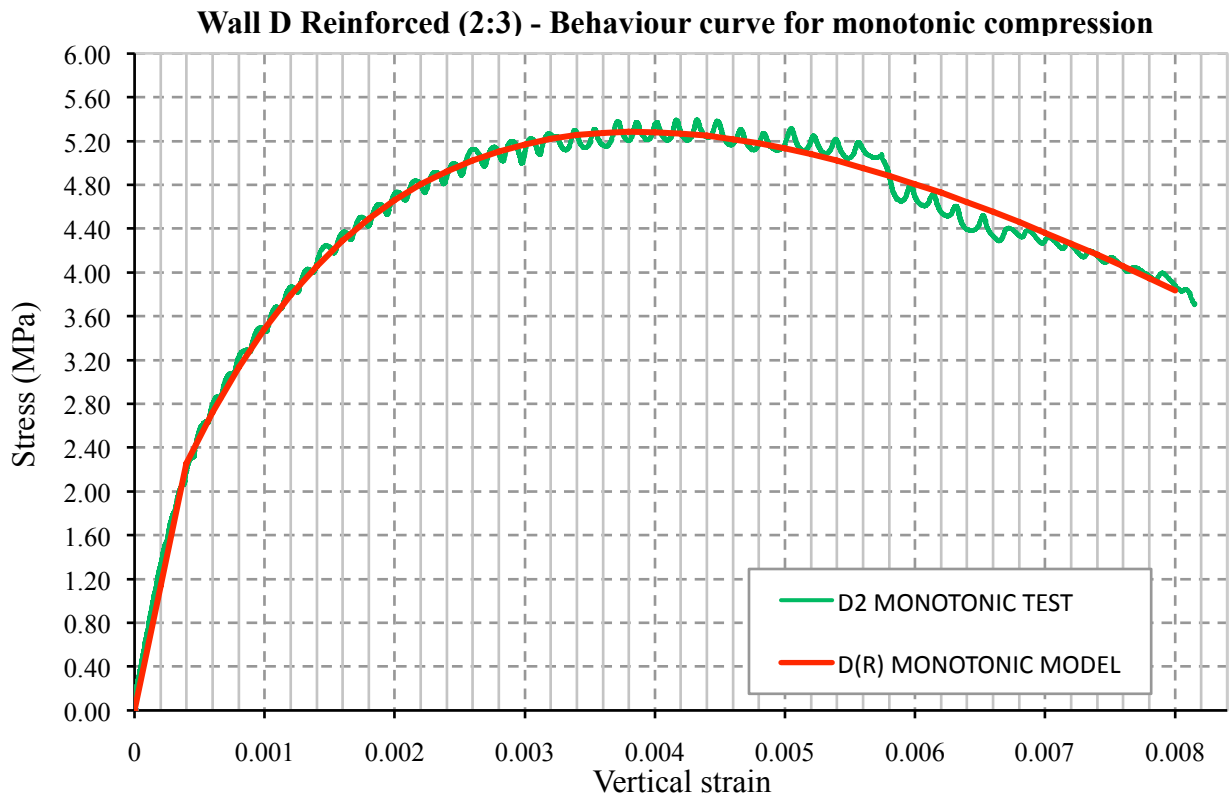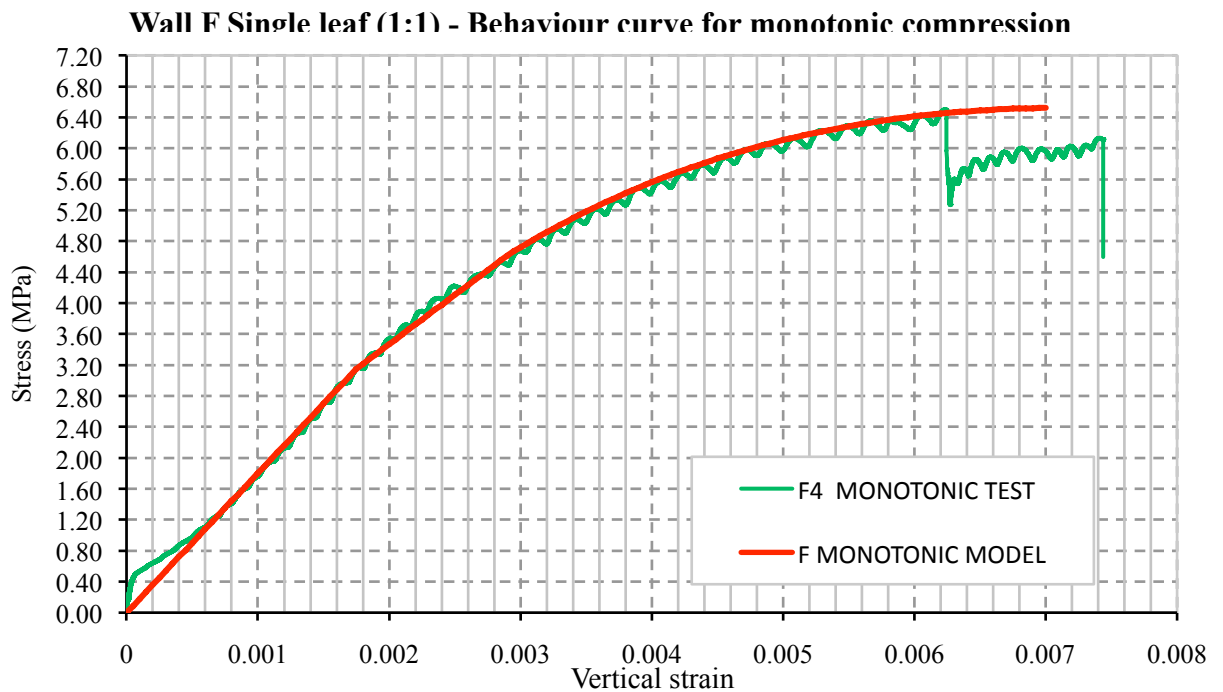Figure 4.15: Experimental and model behaviour curves of the reinforced wall B for monotonic compression.

Wall B Reinforced (1:1) - Behaviour curve for monotonic compression
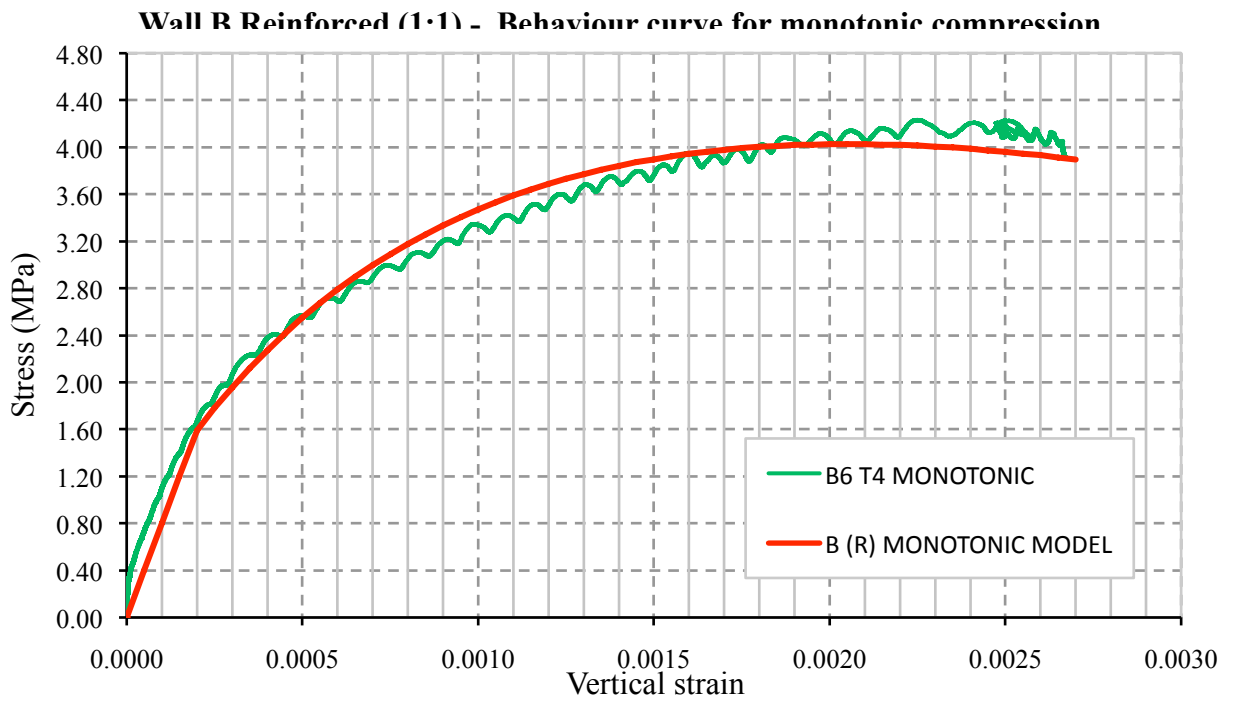
Figure 4.16: Experimental and model behaviour curves of the reinforced wall B for monotonic compression.

Wall D Unreinforced (2:3) - Behaviour curve for monotonic compression
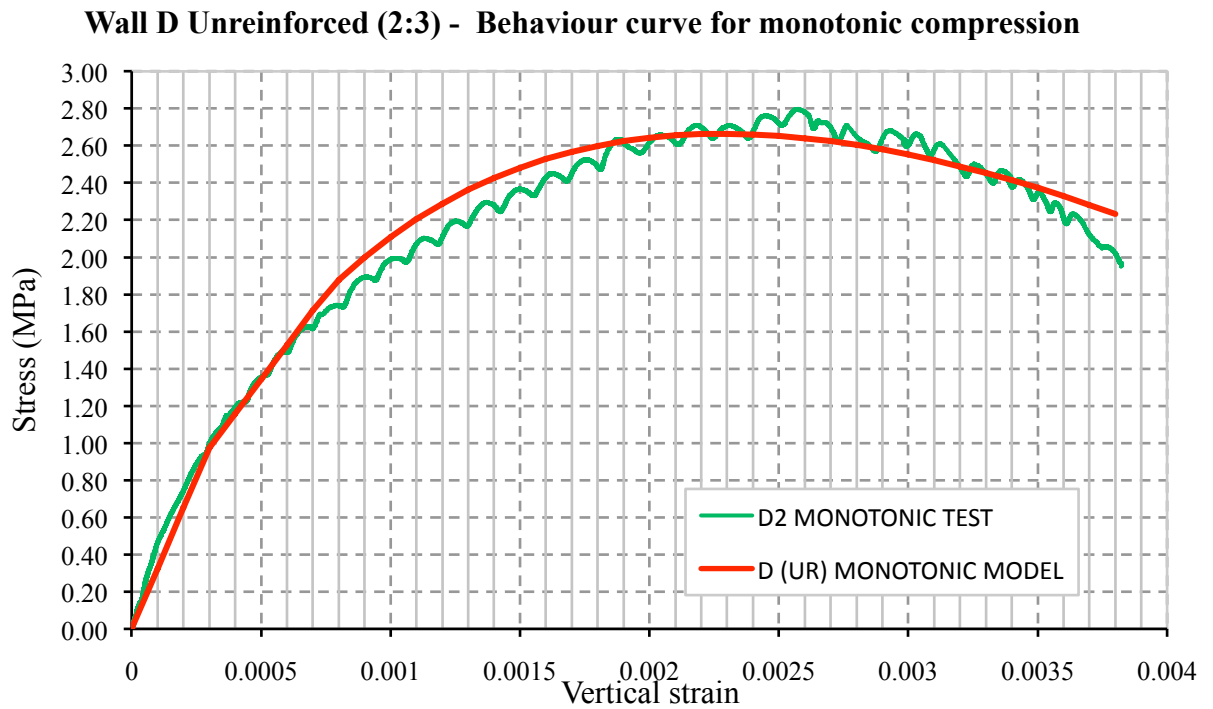
Figure 4.17: Experimental and model behaviour curves of the unreinforced wall D for monotonic compression.
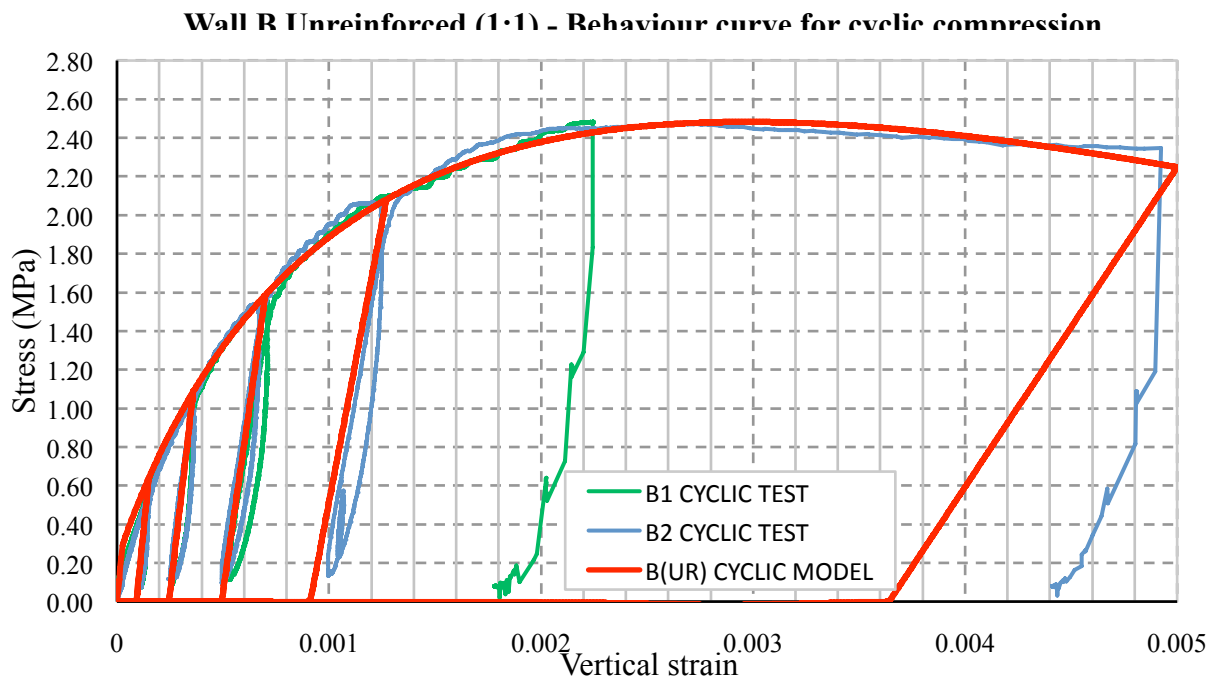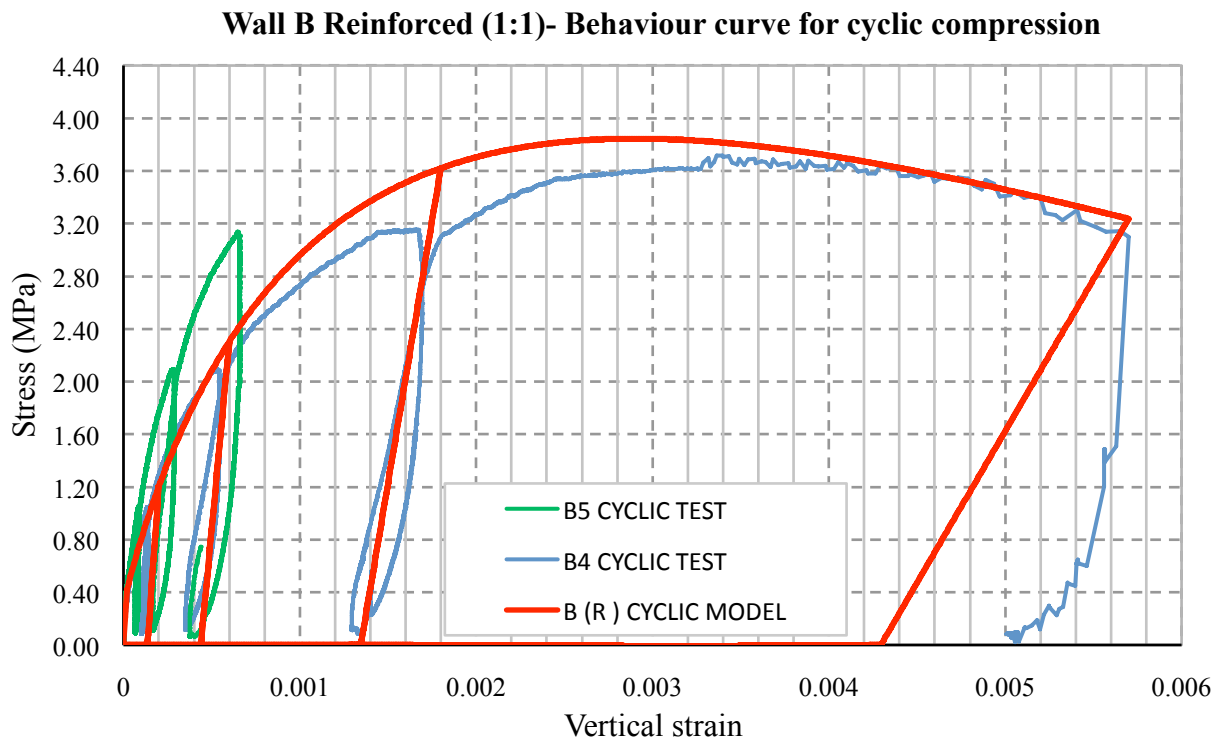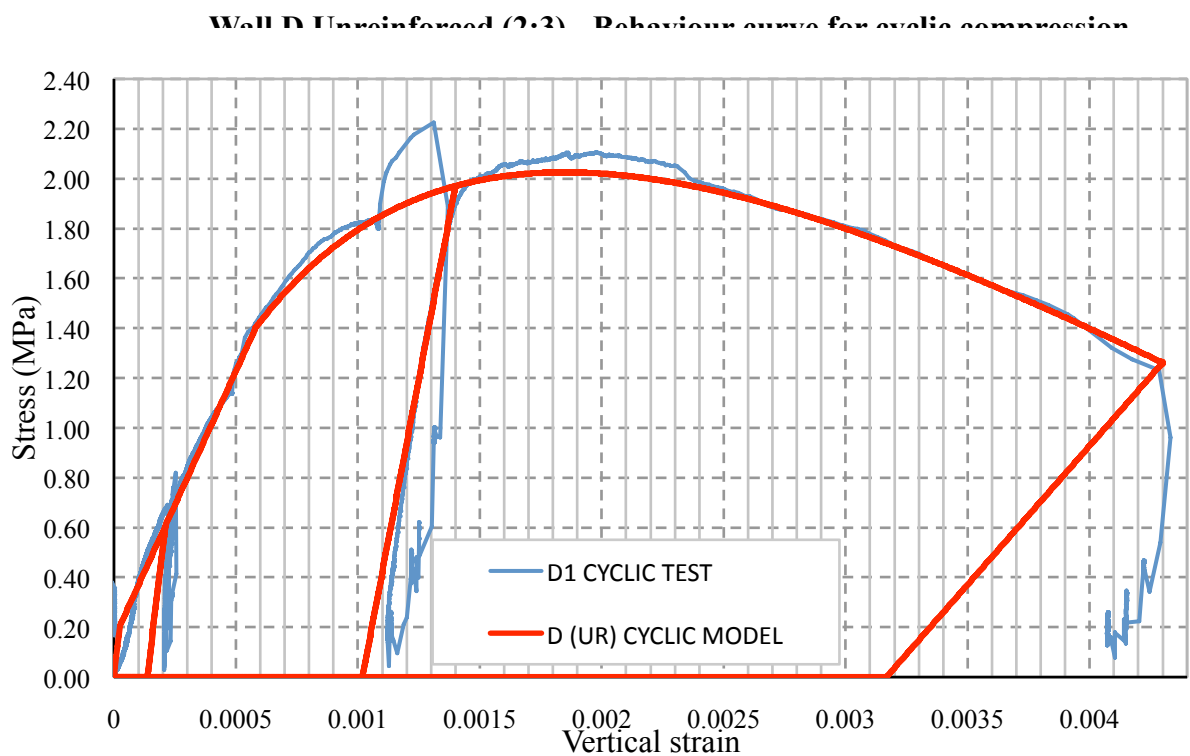
78

Figure 4.18: Experimental and model behaviour curves of the reinforced wall D for monotonic compression.

Figure 4.19: Experimental and model behaviour curves of the single leaf wall F for monotonic compression.

79

Cyclic tests

Table 4.2: Parameter values for the cyclic compression models.

	Parameter	1:1 B(UR)	1:1 B(R)	2:3 D(UR)	2:3 D(R)	1:1 F
YOUN	Young's modulus (N/m^2)	11.53·10^9	21.0·10^9	8.29·10^9	13.17·10^9	14.86·10^9
NU	Poisson's coefficient	0.25	0.25	0.25	0.25	0.25
RHO	Density (kg/m^3)	2600	2600	2600	2600	3200
HLEN	Effective length	Dens=0.05	Dens=0.05	Dens=0.05	Dens=0.05	Dens=0.05
GVAL	Tensile fracture energy (J)	50	50	50	50	20
FTUL	Tensile stress (N/m^2)	0.07·10^6	0.17·10^6	0.07·10^6	0.17·10^6	0.17·10^6
REDC	Drop factor for peak tensile stress	0	0	0	0	0
FC01	Elastic limit compressive stress (N/m^2)	-0.24·10^6	-0.35·10^6	-0.2·10^6	-0.84·10^6	-0.1·10^6
RT45	Equi-biaxial Compressive Ratio	1	1	1	1	1
FCU1	Compressive peak stress (N/m^2)	-2.4·10^6	-3.7·10^6	-2.2·10^6	-4.64·10^6	-5.6·10^6
EXTU	Ultimate limit strai	-0.005	-0.0057	-0.005	-0.008	-0.0044
EXTP	Reference strain for plastic parameter	-0.002	-0.0008	-0.01	-0.005	-0.0003
STRP	Reference stress for plastic parameter	-0.8·10^6	-1.0·10^6	-0.75·10^6	-1.75·10^6	-0.8·10^6
EXT1	Fitting point 1 (Strain)	-0.0015	-0.0020	-0.0012	-0.0013	-0.0022
STR1	Fitting point 1 (N/m^2)	-2.2·10^6	-3.7·10^6	-1.9·10^6	-3.6·10^6	4.9·10^6
EXT2	Fitting point 2 (Strain)	-0.005	-0.0052	-0.003	-0.009	-0.0044
STR2	Fitting point 2 (N/m^2)	-2.25·10^6	-3.4·10^6	-1.8·10^6	-3.6·10^6	-5.8·10^6
NCRI	Tensile softening criteria	1	1	1	1	1

Figure 4.20: Experimental and model behaviour curves of the unreinforced wall B for cyclic compression.

80

Wall B Reinforced (1:1)- Behaviour curve for cyclic compression

Figure 4.21: Experimental and model behaviour curves of the reinforced wall B for cyclic compression.

Wall D Unreinforced (2:3) - Behaviour curve for cyclic compression

Figure 4.22: Experimental and model behaviour curves of the unreinforced wall D for cyclic compression.

81

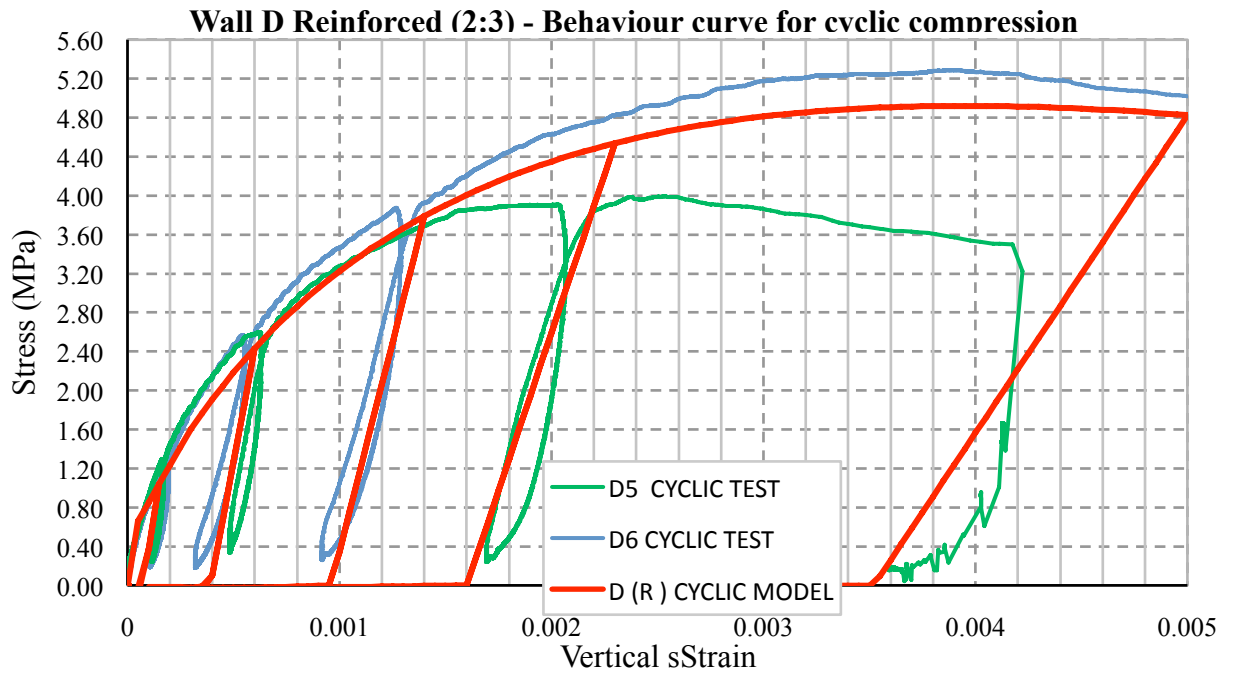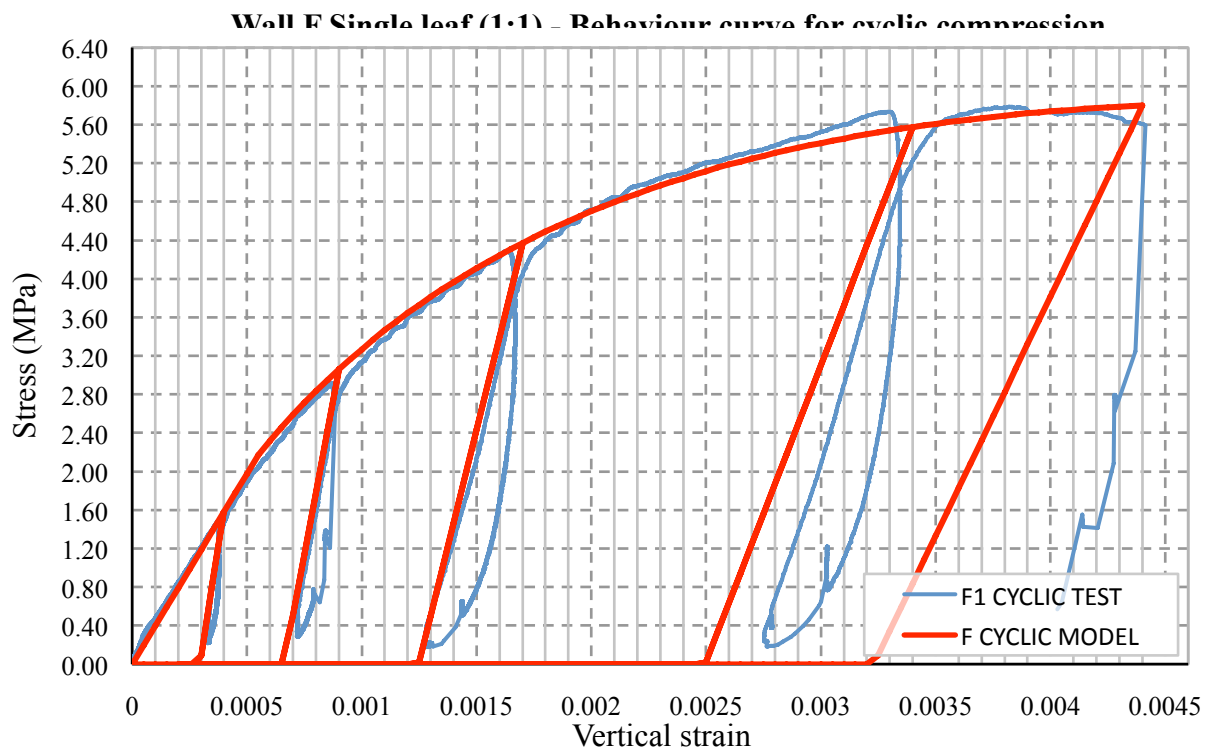Figure 4.23: Experimental and model behaviour curves of the reinforced wall D for cyclic compression.

82

Figure 4.24: Experimental and model behaviour curves of the single leaf wall F for cyclic compression.

4.5 Discussion on the calibration procedure of the compression tests

The fact that for every loading condition the material was calibrated with different properties is acceptable as a method but it creates some restrictions in the use of each model. The cyclic compression model can describe very well the loading cycles and it can be used for non linear time history analysis. Nevertheless, having high values of Young's modulus this model would have the consequence of non realistic results during a modal analysis. Thus, for modal analysis, linear or non linear static (pushover) analysis or lateral force analysis the monotonic compression model is recommended.

In the current project, the material properties have been calibrated assuming a homogeneous material which is able to be used for complex and large dimensions analyses due to the low computational cost. Future research can be focused on the calibration and simulation of inhomogeneous material with three different leaves like the real wall panels. It can be studied the assumption of no interaction between the different leaves or it can be used a joint surface between them with linear or non linear properties. By assessing the accuracy of each method and taking into account the computational cost it can be found the most preferable method depending on the desired type of analysis.

4.6 Finite element models of the wall panels

4.6.1 Description

The exact geometry of the different kinds of panels was modelled in Cast3M. To facilitate the process of the creation of the numerical models into Cast3M, the commercial software programs AutoCad (Autodesk, 2007) and GiD (CIMNE, 2007) were used in combination with some user developed applications.

83

The structure was simulated using 8 nodes volumetric solid elements (CUB8) with three translational degrees of freedom at each node. The structured meshing with such brick elements is considered to be a very effective approach for the consistency and the stability of the analysis. The mesh density was selected to be 0.05 in every direction in order to be able to give sufficiently accurate results without demanding extreme computational effort which would cause time consuming analyses. The base of the walls is fixed and the vertical load is imposed at the top nodes for the compression tests. In the case of future shear and compression tests the horizontal load can be imposed as horizontal displacements at the same nodes.

Although the geometry of the three different leaves has been modelled, the whole body of the masonry wall is simulated as one and homogeneous material. The models are already prepared for future research in which different materials will be added to the leaves. The same model, giving it different properties for every leaf and for the interface between the leaves can be used in the future for non homogeneous properties analyses. Due to the significantly higher strength of the concrete and due to the fact that the stresses in it will not exceed the elastic domain, the concrete properties were selected to be linear and isotropic (Table 4.3).

Table 4.3: Linear isotropic properties for the concrete beams

	Parameter	
YOUN' :	Young's Modulus (N/m^2)	$25 \cdot 10^9$
NU' :	Poisson's coefficient	0.25
RHO' :	Density (kg/m^3)	2500

	Wall A
	Dimensions [cm] 150x(220+40)x50
	Layers [cm] 18/14/18
	Number of elements 17160
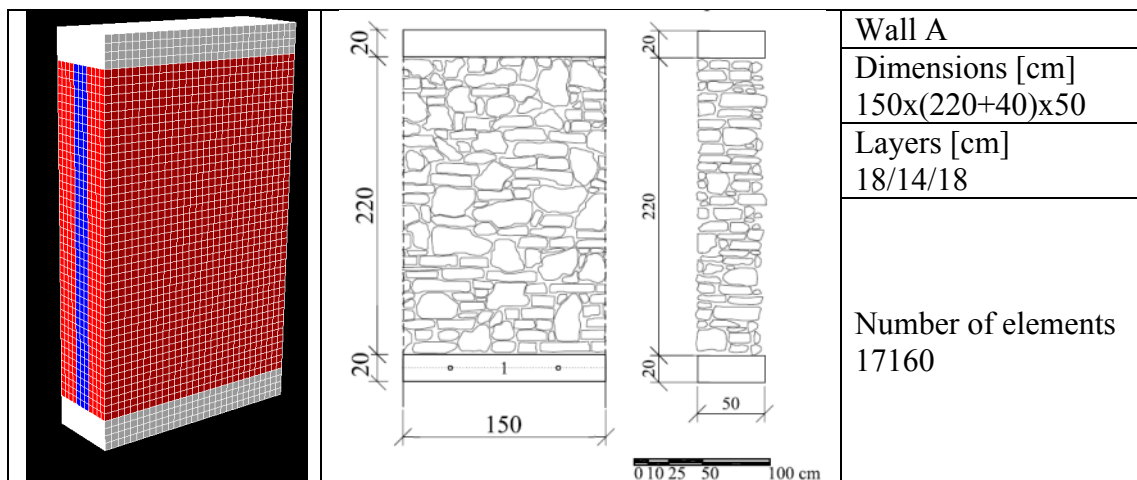
Figure 4.25: Finite element model of the wall A panels.

		Wall B-Wall C
		Dimensions [cm] 100x(120+40)x50
		Layers [cm] 18/14/18
		Number of elements 7392
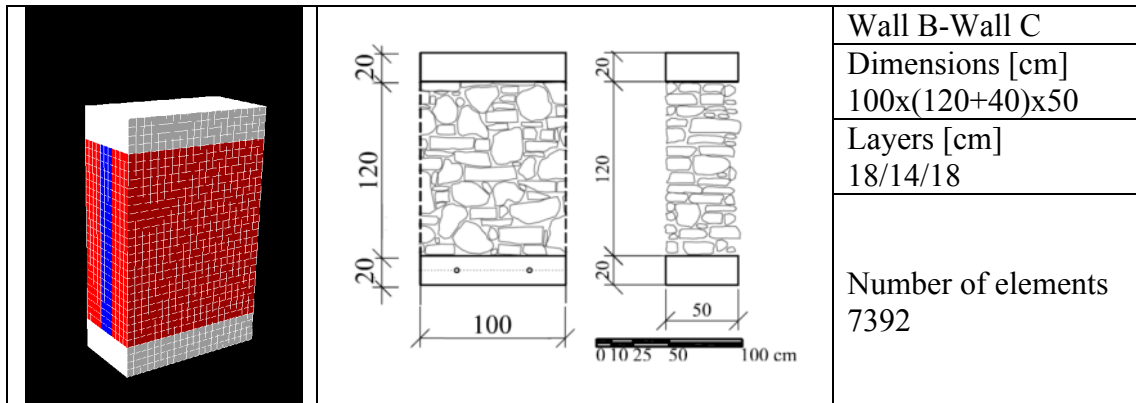
Figure 4.26: Finite element model of the wall B and C panels.

		Wall D-Wall E
		Dimensions [cm] 80x(100+40)x50
		Layers [cm] 12/9/12
		Number of elements 2688
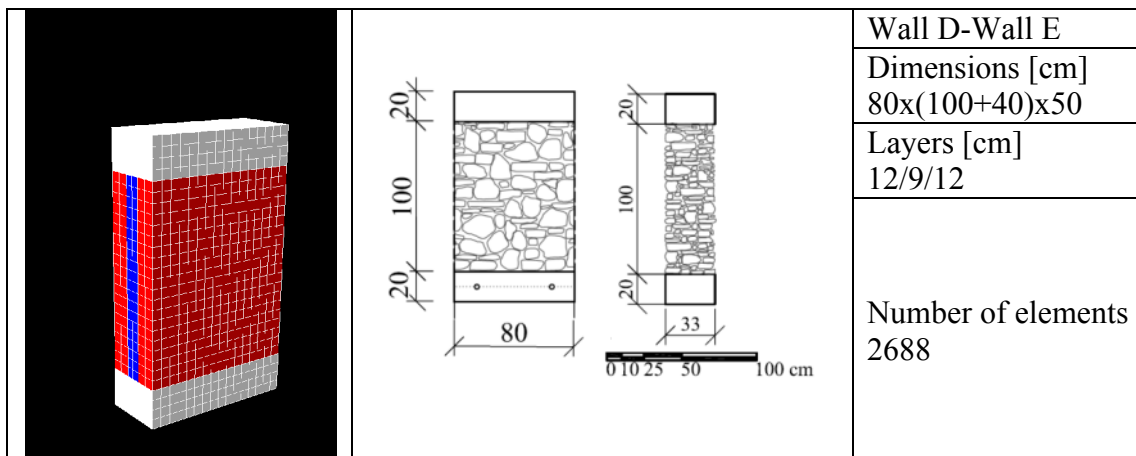
Figure 4.27: Finite element model of the wall D and E panels.

		Wall F
		Dimensions [cm] 150x(120+40)x18
		Layers [cm] 18/-/-
		Number of elements 2240
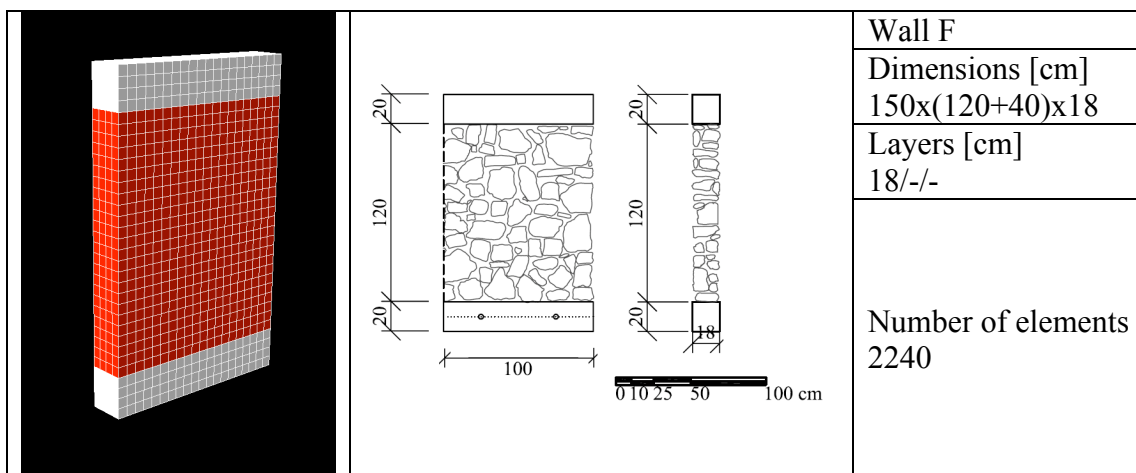
Figure 4.28: Finite element model of the single leaf wall F panels.

85

4.6.2 Behaviour under monotonic and cyclic compression

The numerical analysis of the wall panel models was carried out only for the walls B, C and F for which the material behaviour was calibrated. No experimental test took place for the wall A until now, therefore its behaviour is left to be calibrated in a future work. The preliminary interpretation of the analysis results of the wall panels under monotonic compression seem to be realistic. The stress-strain diagrams for every wall are identical with the ones of their calibrated behaviour curve. Also, the damage level and distribution appear to be plausible (Figure 4.29) on the main faces of the numerical model where they can be correlated with the creation of cracks in the same area of the masonry walls during the tests. Nevertheless, the damage distribution that the model appears on the lateral faces does not represent the reality where the main damage pattern was the detachment of the internal and external leaves. Thus, further research needs to be done in order to reproduce the real damage distribution corresponding to the reality, focusing mainly on the use of inhomogeneous material and also taking into consideration the interface between the internal and external leaves.

86
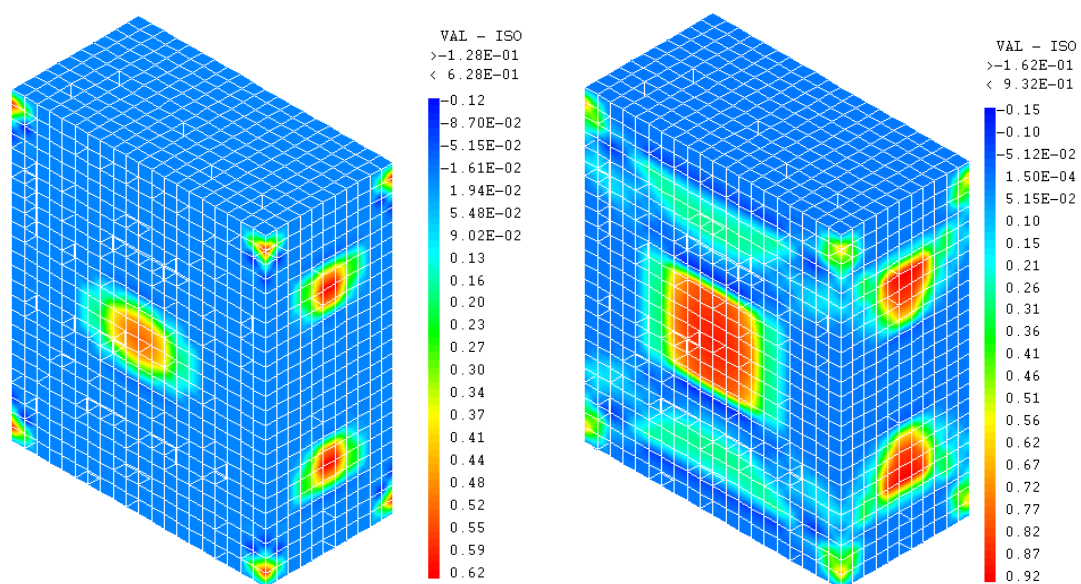
Figure 4.29: Damage levels for the strengthened wall B under monotonic compression for constraint displacement (a) 4mm; (b) 6mm.

4.6.2 Simulation of the shear-compression cyclic loading

In this section it is presented the numerical simulation of a shear-compression test on a reinforced stone masonry panel scale 2:3 (E7) which was the only experimental result available at the moment. The force-displacement diagram which was produced from this test is shown in Figure 4.30.

Shear-Compression test- Reinforced wall E7 (2:3 scale)
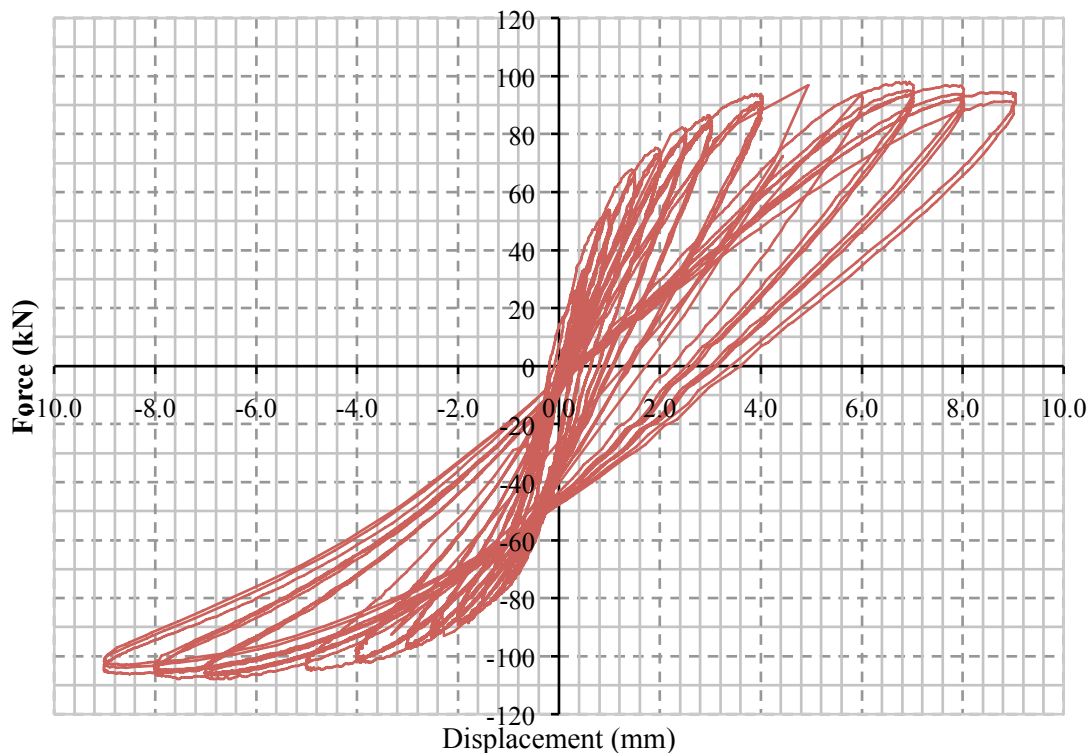
Figure 4.30: Experimental results for the shear-compression test on the reinforced wall E7 (2:3) scale.

In this simulation it was adopted the numerical material behaviour curve calibrated for the wall B under compressive cyclic loading as the walls E and D are of the same typology. The numerical model (already presented previously) was fixed at the base and a compression of 1.5 MPa (30% of the maximum compressive resistance) was

87

applied and kept constant. The displacement history similar to the experimental was applied on the top of the wall (Figure 4.31).

Displacement history for the shear-compression test of the reinforced wall E7 (2:3)
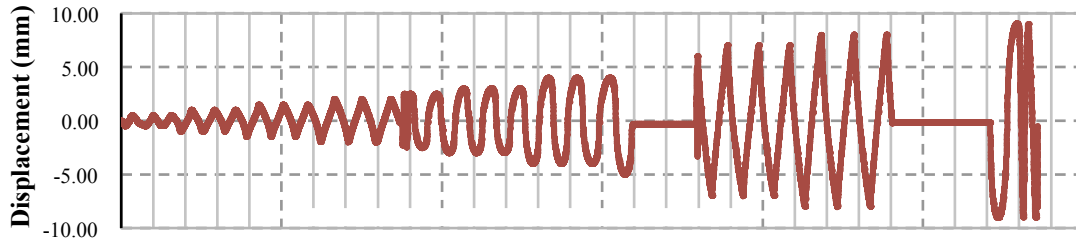
Figure 4.31: Displacement history for the shear-compression test of the injected wall E7 in 2:3 scale.

A preliminary analysis was carried out using the material properties which were found for the cyclic compression tests. In this analysis the numerical model appeared the same maximum base shear force with the experimental results but with a more rigid behaviour.

Thus, a new adjustment of the material properties in order to behave according to the experimental results was performed. The new properties had to give the material a more ductile behaviour which would appear the maximum stress at higher strain levels.

With the current damage model it was not possible to capture the behaviour of both of the segments of the force-displacement diagram at the same time as the obtained experimental results were not totally symmetric. If it is adopted a model with low rigidity the segment on the positive force domain can be simulated (lower bound) while with higher rigidity it is possible to have a behaviour close to the other segment (upper bound). The lower bound numerical material behaviour is shown in the Figure 32 and the upper bound in the Figure 33.

Shear-Compression numerical material behaviour curve (2:3 scale)-Lower bound
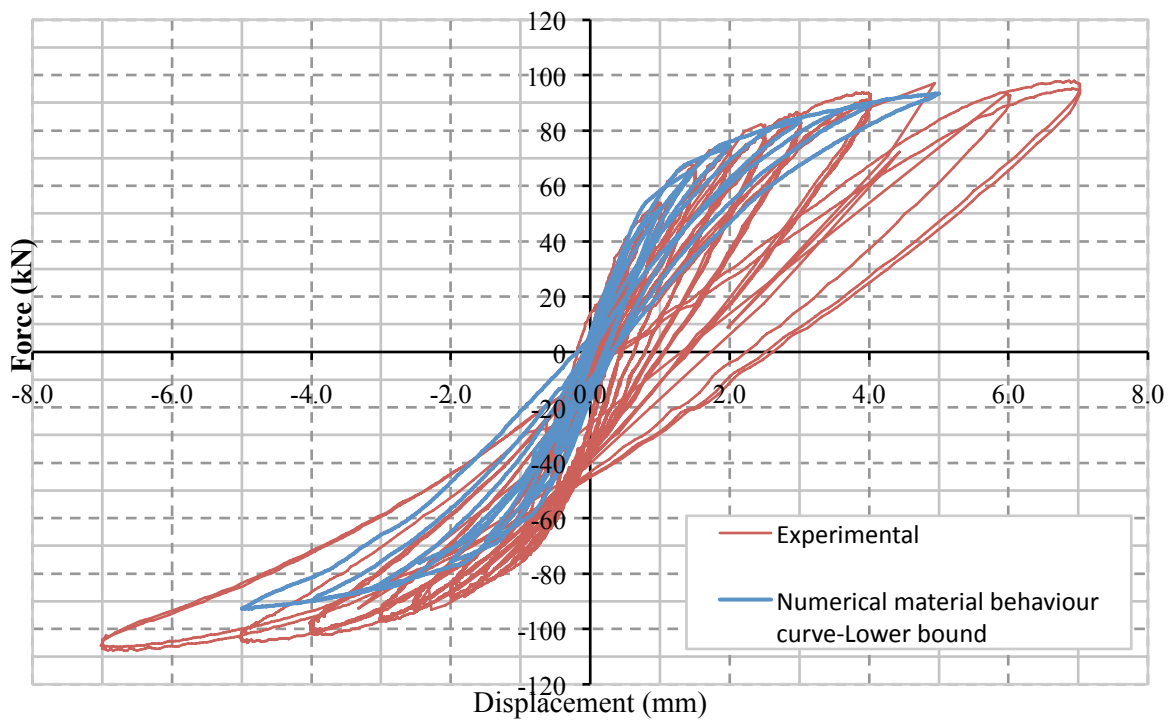
Figure 4.32: Numerical model material behaviour – Lower bound.

Shear-Compression numerical material behaviour curve (2:3 scale)-Upper bound
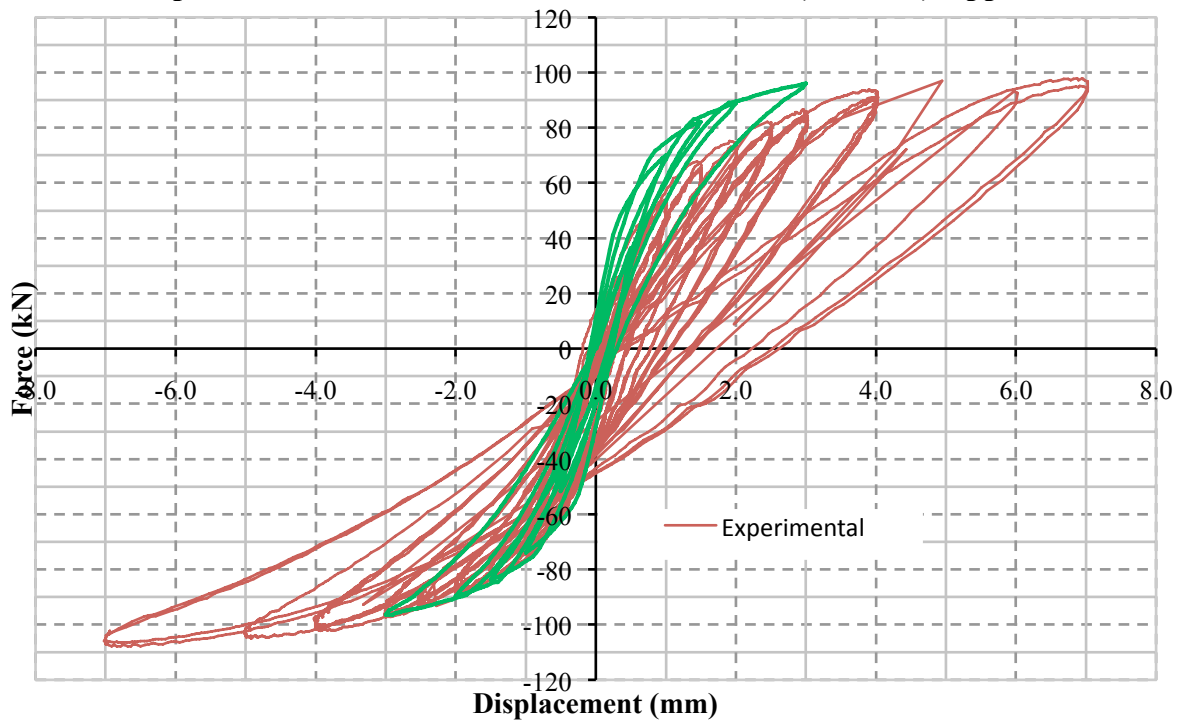
Figure 4.33: Numerical model material behaviour – Upper bound.

89

The modified curves were found via a 'try and error' repetitive procedure of manual calibration keeping the G_{fc} constant and trying to approach the experimental behaviour. The compressive fracture energy can be found by the area included under the peak stress point and the ultimate strain multiplied by the length of the used finite element. The stress and strain parameters which were modified are presented in the Table 4.4 and the original and the modified curves for the upper and lower bounds are shown in the Figure 4.34

Table 4.4: Original and modified parameters for the shear-compression simulation

	Parameter	Initial	Lower bound	Upper bound
FCU1	Compressive peak stress (N/m^2)	$-4.64 \cdot 10^6$	$-2.32 \cdot 10^6$	$-3.25 \cdot 10^6$
FC01	Elastic limit compressive stress (N/m^2)	$-0.4 \cdot 10^6$	0.0	0.0
EXTU	Ultimate limit strain	-0.005	-0.0105	-0.0013
EXT1	Fitting point 2 (Strain)	-0.0013	-0.0015	-0.0015
STR1	Fitting point 1 (N/m^2)	$-3.6 \cdot 10^6$	$-1.61 \cdot 10^6$	$-2.27 \cdot 10^6$
EXT2	Fitting point 2 (Strain)	-0.009	-0.0135	-0.0135
STR2	Fitting point 2 (N/m^2)	$-3.6 \cdot 10^6$	$-3.6 \cdot 10^6$	$-4.0 \cdot 10^6$
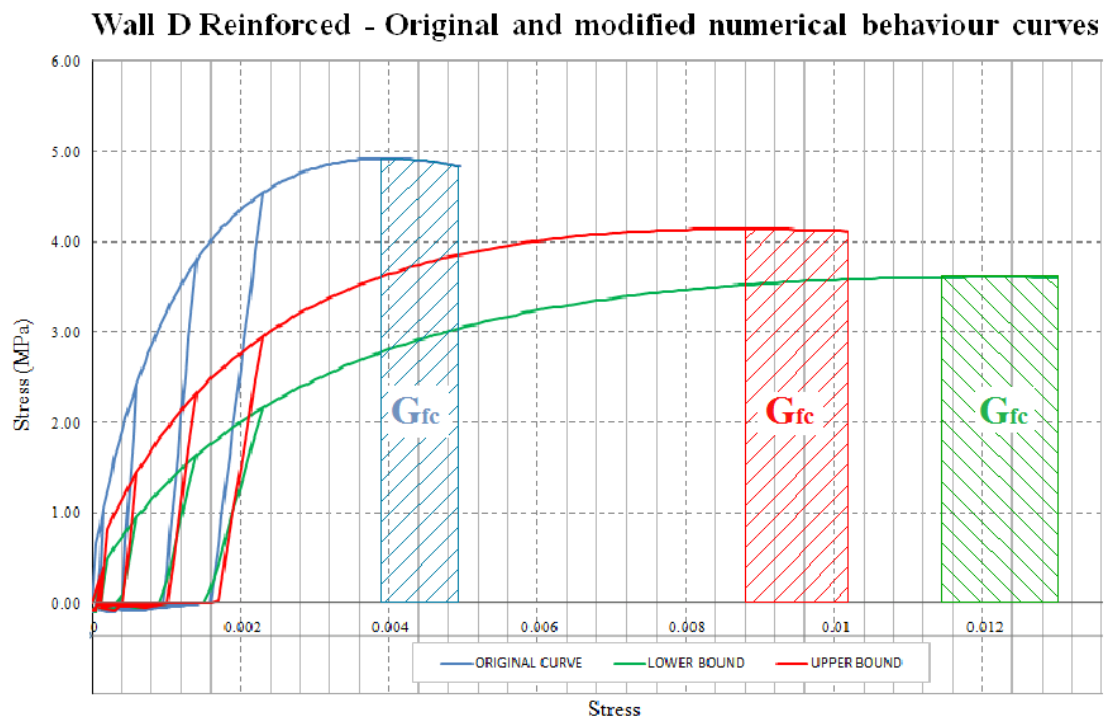
Figure 4.34: Initial and modified curves keeping constant the compressive fracture energy.

90

Either an average between the lower and upper bound or for more conservative results the lower bound curve can be adopted for the simulation of the shear-compression test and for application in more complex experimental and real case studies. It can be noticed that the numerical model can reproduce quite well the dissipation until a certain level of horizontal displacement, i.e., it is impossible for a finite element model to be able approach the real dissipation and the hysteretic behaviour of the masonry wall when it demonstrates a highly non linear behaviour characterised by the formation of big cracks (Figure 4.35). It is expectable that the large scale cracks produced during the shear-compression test and the energy that is dissipated during their cyclic opening and closing cannot be reproduced from a numerical model based on the continuous mechanics.

Figure 4.35: Stone masonry wall during shear-compression test experiencing the formation of big cracks.

91

4.7 Conclusions of the numerical behaviour calibration

It can be concluded that the damage model which was used, with the assumption of homogeneous material, it has the ability to capture the behaviour of the stone masonry walls under monotonic and cyclic compression test in a satisfactory extent. Nevertheless, different properties had to be used for the two cases in order to make possible the reproduction of the unloading-loading segments of the cyclic compression cyclic stress-strain diagrams. Those different parameters and especially the different Young modulus of elasticity put some limitations in the use of the calibrated numerical behaviour properties regarding with the type of analysis that is going to be carried out. The properties occurred from the calibration of the cyclic compression test are applicable for use on time history analysis while the ones of the monotonic compression can be used for pushover or lateral force analysis.

The analysis which was carried out for the simulation of the shear-compression test showed that in order to simulate the real behaviour of the masonry wall, the numerical material behaviour properties had to be recalibrated with emphasis on the higher ductility and the lower rigidity. From this procedure occurred a lower and an upper bound for the numerical material properties in order to be able to reproduce the two different segments of the force-displacement diagram. The numerical model was able to have hysteretic behaviour with energy dissipation during the cycles; however it was not possible using a finite element model to fully reproduce the highly non linear behaviour and to appear the same level of energy dissipation and overall deformation with the real stone masonry wall.

Chapter 5

Case study: San Domenico church of L'Aquila

5.1 Introduction

In this chapter it is presented the San Domenico church of L'Aquila which evidenced severe damages during the earthquake of Abruzzo on the 9th of April 2009. The University of Padova participates actively in the work of the overall damage investigation and structural analysis and strengthening of the church. For the needs of a future finite element analysis of the structure a numerical model has been created. The numerical behaviour parameters which will be used will be based on the calibration which was realised based from the already described laboratory experimental campaign of UNIPD. Useful parameters for the further calibration of the church numerical model can be taken by the available results of the non destructive and minimum destructive test on the structure. Moreover, the numerical results can be used for the correlation with the also available macroelement identification of the failure mechanisms for verifying the structural pathologies. Finally, the same numerical model can be used for the study of future interventions

5.2 Historical review

The church of San Domenico was built by the Domenican friars on one of the highest hills of l'Aquila. The location was formerly occupied by the Palazzo Reale, residence of Carlo II d'Angiò who gifted it to the friars according to his vow when he was

94

imprisoned in Barcelona. The new structure which started in 1309 was planned to include in its body a pre-existing smaller church of the previous century.

Figure 5.1: Arial views of San Domenico church of L'Aquila: South (top left); East (bottom left); North (top right); West (bottom right).

The building was continuously being built and repaired as a result of the various intense earthquakes of the area including the ones of 1315 and 1349 during the first years of construction and later one of 1452. In 1461 another earthquake cause the collapse of the central and of one lateral naive. Intense seismic events also happened in 1501 and 1646. The most tragic incident in the history of San Domenico happened by the earthquake which took place on the 2nd of February 1703 around noon when the church was full of people participating in the celebrating ceremony of Cantelora. The collapse of the roof and of the whole apsidal system caused around 600 human losses out of the 3000 deaths that the city counted, [Antonini (2010)]. The repair of the structure lasted until 1712 and it finished with the adding of architectural details according to the Baroque style. The most intense earthquake in the history of the city causing 6000 deaths happened in 1786. Recently, L'Aquila suffered from the severe earthquake of the 6th of April 2009, which had an epicenter very close to the city and a magnitude of 6.3 Richter, resulting in 308 deaths and in huge amounts of damage mainly of masonry structures. Important damages were caused also at the San

95

Domenico church. The structural issues had to be addressed urgently in order the overall stability of the church not to be endangered.

5.3 Structural description

The church is built in a plain form with the western wall to be joined with the San Domenico monastery complex. The main façade on the South-West direction is partially dressed since the 14th century with stones due to economical problems in that historical period. The façade also brings two circular windows laterally filled with building material and one rectangular window above the main entrance which replaced the preexisting circular opening collapsed during an earthquake in 1709.

Figure 5.2: Main façade of San Domenico church.

The structure consists of one transept one naive and two aisles, laterally disposed symmetrically with respect to the naive. The apse and the transept bear vaults surrounding the main dome of the church. Smaller of symmetric dimensions domes are covering the aisles supported on one side by two columns and on the other by the masonry church wall. The columns separating the central nave from the side aisles are cruciform in section. The overall length of the structure is 68m with a width of 28m at the main façade and 37m at the transept. The maximum height of the church on the top of the main dome is 22m. The nave and the aisles are divided into 6 parts, with the

ones of the nave to have dimensions approximately 6m by 12m and of the aisles around 7m by 6.5m.
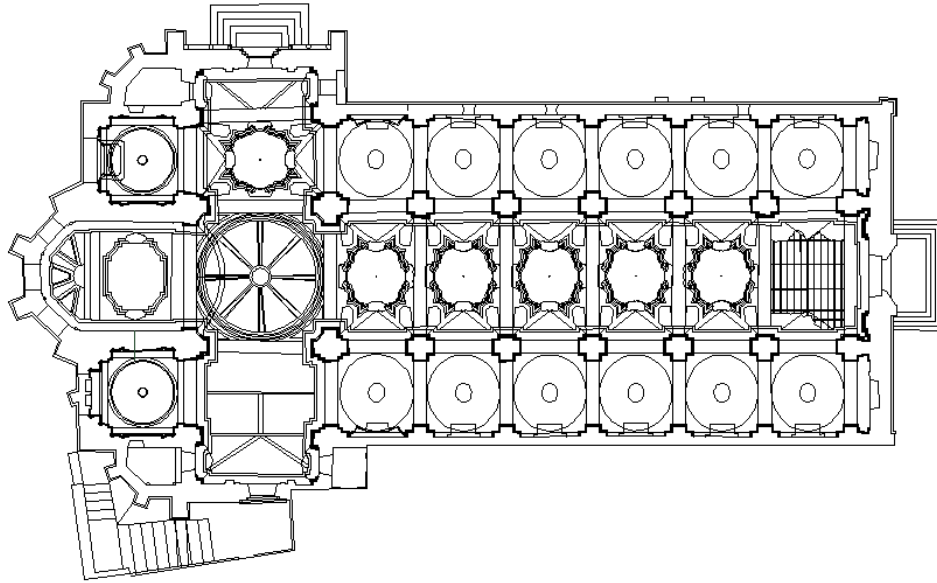
Figure 5.3: Floor plan of the San Domenico church.

5.4 Damage identification with the use of macroelements

The extended damage survey and the identification of the macroelement failure mechanism was a part of the huge investigation work which followed the 2009 earthquake and in which the University of Padova participated. The summarised results of the macroelement identification are presented in this section.

The damage grades which were used are according to the European macroseismic scale 1998 (EMS-98), published by the European Seismological Commission. These grades have been developed to enable a clearer relationship between the observed level of damage and the magnitude of the seismic event. The damage grades are shown in the Table 5.1.

Table 5.1: Damage grades according to the European macroseismic scale of 1998

Assessment	Description
Grade 1	Negligible to slight damage
Grade 2	Moderate damage
Grade 3	Substantial to heavy damage

97

| Grade 4 | Very heavy damage |
| Grade 5 | Destruction |

Summarised results of the macroelement identification

1. OVERTURNING OF THE FACADE   Damage Rating: ☒☒☒☐☐
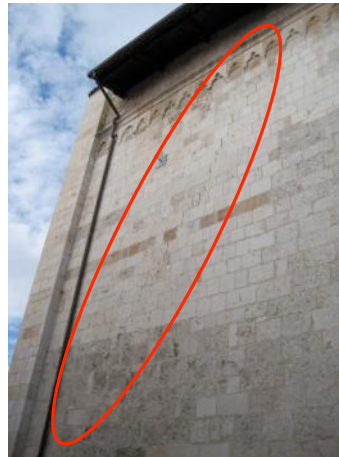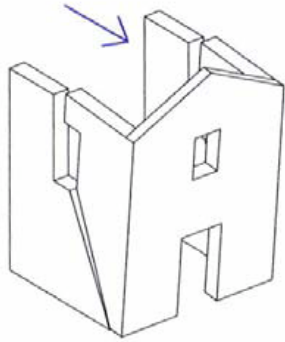
External View	Internal View

Observed Damage:

- Cracking within the external side wall at the south-west corner of the Church. Indicates mobilisation of out of plane facade mechanism towards the front of the Church.
- Cracking extends full thickness of the wall.

Observed Vulnerabilities:

- Lack of longitudinal ties or buttresses.
- High imposed lateral actions with hammering by the reinforced concrete roofing system.

2. MECHANISMS AT UPPER PART OF FACADE   Damage Rating (critical area): ☒☒☒☒☒
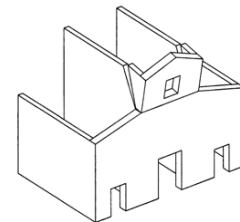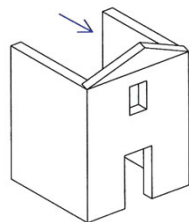
Gable of west façade	View from south-west

Observed Damage: Observed Vulnerabilities:

98

Complete overturning at the upper section of the facade.
Out-of plane displacement of upper section of the facade.

Lack of longitudinal ties or buttresses.
High imposed lateral actions with hammering by the reinforced concrete roofing system.

3. SHEAR MECHANISMS IN THE FACADE

Damage Rating: ☒☒☐☐☐
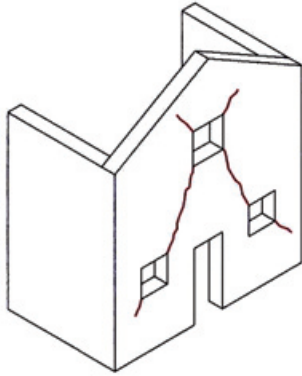
Western entrance

Observed Damage:
Minor diagonal and vertical cracking within façade above and at northern side of doorway and above and below circular niches.

Observed Vulnerabilities:
Lack of lateral ties.
Presence of openings.

4. TRANSVERSAL VIBRATION OF NAVE

Damage Rating: ☒☒☒☐☐
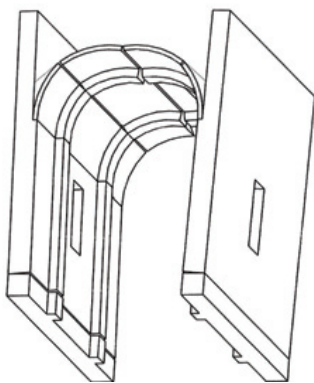
View of nave arches from transcept, following some repairs including installation of temporary ties and FRP intrados reinforcing

99

Observed Damage:
- Longitudinal cracking within arches in central nave.
- Deterioration at base of columns.

Observed Vulnerabilities:
- Lack of lateral ties or buttresses.
- Detachment of upper level reinforced concrete roof system from nave walls.

5. SHEAR MECHANISMS IN THE SIDE WALLS   Damage Rating: ☒☐☐☐☐
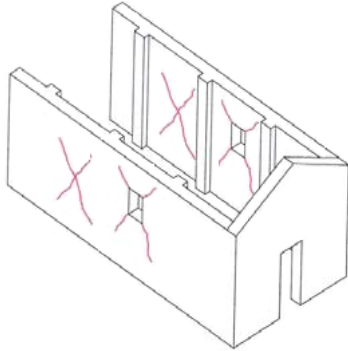
Eastern end of southern external wall

Observed Damage:
- Minor cracking within external leaf of masonry

Observed Vulnerabilities:
- Possible slight opening of an existing cracking under shear forces, possibly originally due to differential settlements.

6. LONGITUDINAL VIBRATION OF THE CENTRAL NAVE   Damage Rating: ☒☒☒☐☐
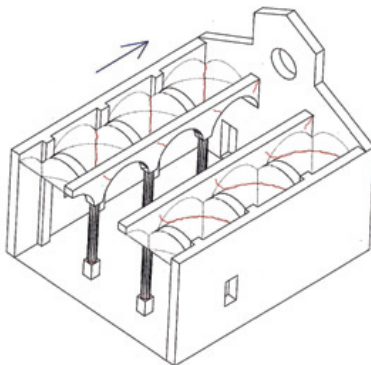
Cracking at base of columns

Observed Damage:
- Cracking and spalling of renders and masonry at base of columns.
- Minor cracking of longitudinal archways at inner side of nave.
- Significant cracking at surrounds of side naves.

Observed Vulnerabilities:
- Lack of effective longitudinal buttresses.
- Imposed longitudinal forces by reinforced concrete roofing system.
- Bending at base of columns due to longitudinal forces, combined with axial forces from loads and

100

from significant vertical seismic excitation.

7. VAULTS OF THE CENTRAL NAVE

Damage Rating (critical area): ☒☒☒☒☒
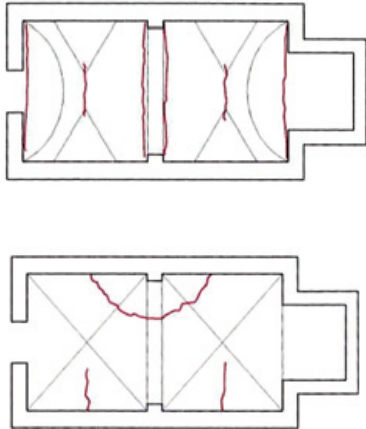


Westernmost vault of central nave

Observed Damage:

- Collapse of westernmost vault.
- Cracking adjacent to longitudinal arches in subsequent vaults.

Observed Vulnerabilities:

- High imposed longitudinal and lateral actions by the reinforced concrete roofing system.
- Hammering action from roof to vault structures, as they are supported independently by the side nave walls.

8. VAULTS OF THE SIDE NAVES

Damage Rating: ☒☒☒☐☐
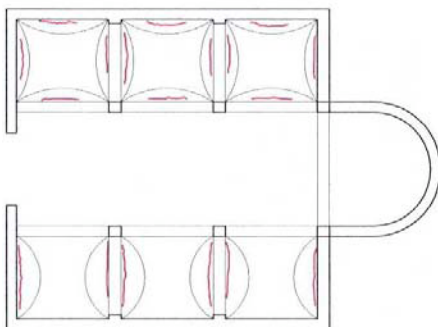
Typical vault of side nave
(central nave to right of picture)

101

Observed Damage:
- Detachment around perimeter of vaults from arch supports both between vaults and along central nave.
- Cracking and spalling of renders.
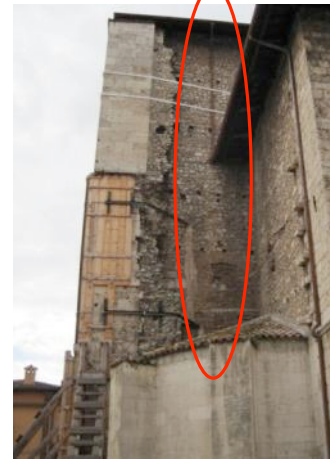
Observed Vulnerabilities:
- High imposed longitudinal actions by the reinforced concrete roofing system to walls of the central nave.
- Development of shear stresses within side vaults due to differential displacement of central nave supports and external walls.

9. OVERTURNING OF END WALL OF TRANSEPT   Damage Rating: ☒☒☒☒☐
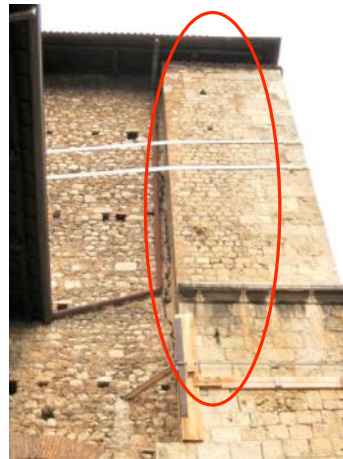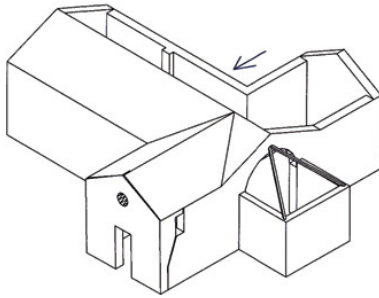
Western side of transept   Eastern side of transept

Observed Damage:
- Out of plane displacement of façade to the south.
- Detachment of the façade from each of the side walls of the transept.
- Cracking extends full thickness of the wall.

Observed Vulnerabilities:
- Lack of longitudinal ties or buttresses.
- Inconsistent wall thickness and morphology between façade and return walls.
- High imposed lateral actions with hammering by the reinforced concrete roofing system.

10. SHEAR MECHANISMS IN THE TRANSEPT   Damage Rating (critical area):

☒☒☒☒☒
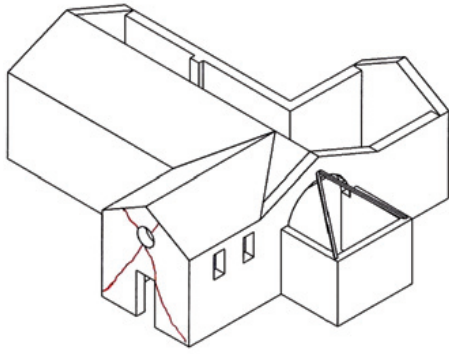
Southern end wall of transept

Observed Damage:

- Collapse of masonry above upper level opening.
- Significant inclined shear cracking that extend the full wall thickness.

Observed Vulnerabilities:

High imposed lateral actions parallel to end wall by reinforced concrete roofing system. Lack of effective ties or buttresses parallel to end wall of transept.

11. VAULTS OF THE TRANSEPTS

Damage Rating (critical areas): ☒☒☒☒☒
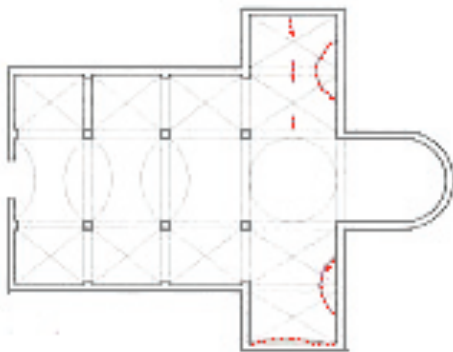
Remnants of northernmost vault of transept
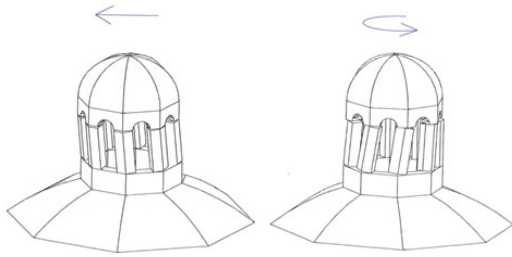
Observed Damage:

- Collapse of northernmost and southernmost vaults.
- Cracking adjacent to and within supporting arches and walls.

Observed Vulnerabilities:

- High imposed longitudinal and lateral actions by the reinforced concrete roofing system through vault supports.
  High vertical actions due to significant vertical seismic excitation.

12. LANTERN

Damage Rating: ☒☒☐☐☐
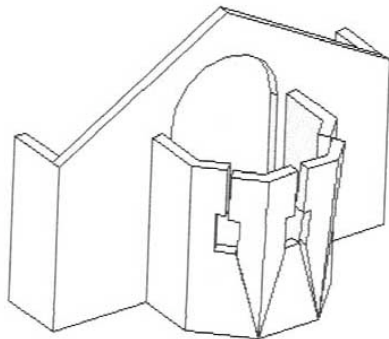
103

South-east side of lantern

Observed Damage:

- Horizontal cracking aligned with top of lantern piers.
- Minor spalling of render and loss of lateral support to timber frames.

Observed Vulnerabilities:

- Lateral and torsional loadings from lantern roof at top of piers.

13. OVERTURNING OF THE APSE

Damage Rating: ☒☒☒☒☐

Southern side of apse
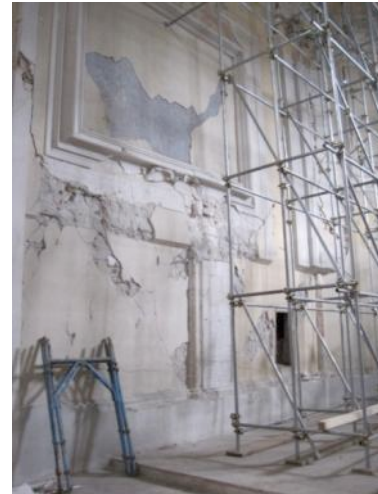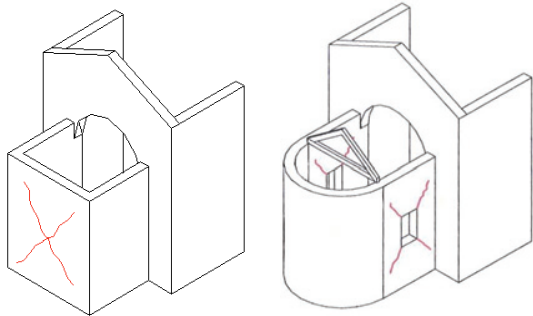
Northern side of apse

Observed Damage:

- Fracturing of walls between buttresses with out of plane deformation of apse walls.
- Cracking extends full thickness of the wall.

Observed Vulnerabilities:

- Lack of effective ring or longitudinal ties.
- Wall weakening at openings.
- High imposed lateral actions with hammering to western side of apse by the reinforced concrete roofing system.

14. SHEAR MECHANISMS IN PRESBYTERY / APSE

Damage Rating: ☒☒☐☐☐

104

Northern side of apse, facing east
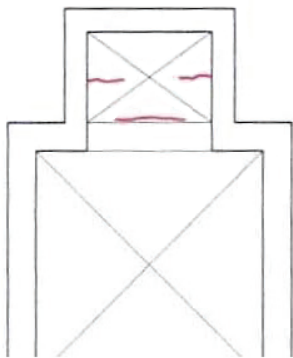
Observed Damage:

- Diagonal shear cracking within internal walls of apse.

Observed Vulnerabilities:

- Irregular masonry and openings within wall.
- Imposed actions parallel to wall by the reinforced concrete roofing system at western side of apse.

15. VAULTS IN THE PRESBYTERY AND THE APSE   Damage Rating: ☒☒☐☐☐

Dome of northern presbytery

Observed Damage:

- Cracking and spalling of plaster within dome of presbytery in both radial and longitudinal patterns.
- Vertical cracking of plaster at dome support at regular spacings.

Observed Vulnerabilities:

- High imposed longitudinal actions by the reinforced concrete roofing system of the adjacent transept.
- High vertical actions due to significant vertical seismic excitation.

105

16. ROOF MECHANISMS, SIDE WALLS OF NAVE / AISLES   Damage Rating: ☒☒☐☐☐
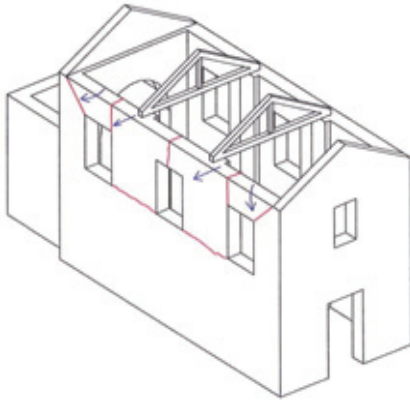
Western end of southern nave wall
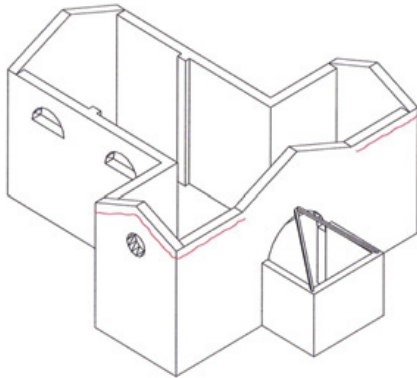
Observed Damage:

- Cracking of masonry at support to roofing member.

Observed Vulnerabilities:

- High imposed longitudinal actions and hammering by the rigid reinforced concrete roofing system.

17. ROOF MECHANISMS OF THE TRANSEPT   Damage Rating: ☒☒☐☐☐

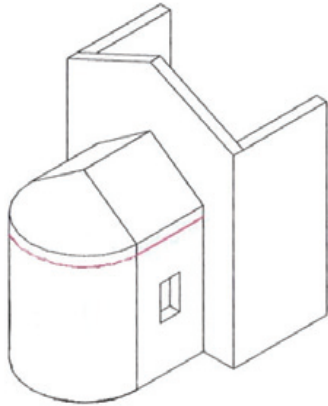Top of southern end wall of transept

Observed Damage:

- Cracking and dislocation of masonry out of plane at top of the wall immediately below the roof support.

Observed Vulnerabilities:

- High imposed longitudinal actions and hammering by the reinforced concrete roof system of the transept.
  High vertical actions due to significant vertical seismic excitation.

106

18. ROOF MECHANISMS OF APSE / PRESBYTERY   Damage Rating: ☒☒☐☐☐



Top of southern wall of apse

Observed Damage:
- Cracking and dislocation of masonry along top of the wall immediately below the roof support.

Observed Vulnerabilities:
- High imposed longitudinal actions and hammering to the apse walls by the reinforced concrete roof system of the adjacent transept.
- High vertical actions due to significant vertical seismic excitation.

19. INTERACTIONS WITH ADJACENT BUILDINGS   Damage Rating: ☒☒☐☐☐
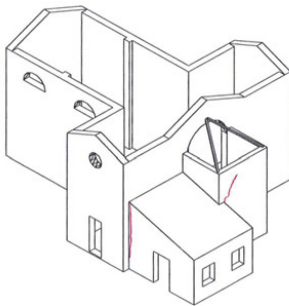
Upper northern corner of west façade

Observed Damage:
- Out of plane displacement of masonry above connection to adjacent structure.
- Horizontal cracking within bed joints coincident with wall height of adjacent building.

Observed Vulnerabilities:
- Hammering action between adjacent buildings subjected to different actions, of different stiffness and morphology.
- Lack of effective separation between adjacent building elements.

5.5 Non destructive and minimum destructive tests

107

A plethora of in situ non destructive (NDT) and minimum destructive (MDT) were carried out for the church of San Domenico. In case of structures with high historical importance like the San Domenico church and despite the already existing damage due to the earthquake the NDT and MDT are the most applicable methods in order both to achieve an evaluation of the structural condition of the building and to avoid extensive damage caused by more destructive techniques [Gregorczyk and Lourenço (2000)]. In the tests are included sonic pulse velocity tests, single and flat jack tests, Schmidt hammer tests, pacometer tests and dynamic identification tests. was performed by the EXPIN Ltd. Company, a spinoff of the University of Padova and the equipment belongs to the Department of Construction and Transportation of the University of Padova. The interpretation of the results occurred from those tests in combination with the visual inspection and the architectural survey are very crucial for the knowledge of the overall behaviour of the structure, for the safety assessment, for the evaluation of the effectiveness of the repair techniques and for the calibration the behaviour parameter of a numerical model.

5.5.1 Sonic pulse velocity tests

Description

The sonic pulse methodology is a non-destructive testing technique based on the generation of sonic waves and their propagation through the body of the structure. The elastic wave is created by a transmitter (instrumental hammer) and it is collected by receiver (piezoelectric accelerometer). The presence of voids within the masonry can be detected, as the transmission path of the wave prefers higher density material and will take longer for it to reach the receiver if many discontinuities force it to travel a longer distance [DELIVERABLE D11.1 (2004)]. The sonic pulses given to the material are in the frequency range of mechanical sound (20-20000 Hz). The necessary equipment for the carrying out the test includes a hammer and accelerometers all connected to a signal amplifier and an analogue-digital converter. Finally, all the data are acquired by the computer unit and with the proper software it

records the impulse of the hammer and the receiver wave, plotting both on the same axes. The system setup is presented in the Figure 5.4.
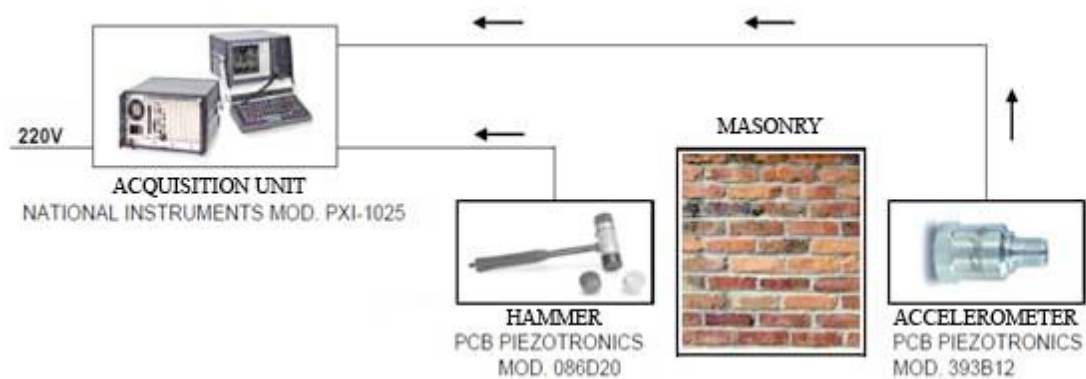

Figure 5.4: Equipment setup for the sonic pulse velocity test [Casarin (2006)].

The sonic velocity test can be performed using different transmission methods:

(a) Direct method

(b) Indirect or superficial method

(c) Semi-direct or radial method

(d) Sonic tomography method

These different configurations are shown in Figure 5.5 where the green dot represents the location of the hammer transmission and the yellow dots represent the locations of the accelerometers.
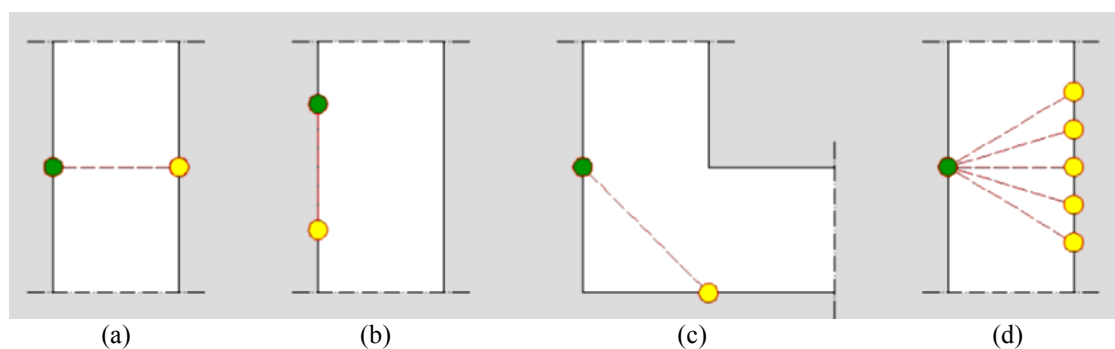

| (a) | (b) | (c) | (d) |

Figure 5.5: Sonic pulse velocity tests configurations: (a) direct; (b) indirect or superficial; (c) semi-direct or radial; (d) sonic tomography [DELIVERABLE D11.1 (2004)].

(1)   Direct transmission method

109

In the direct sonic test the transmitter and the receiver are positioned on the opposite sides of the wall, thus the wave goes through the thickness of the wall. With this method the consistency and quality of the wall can be evaluated.

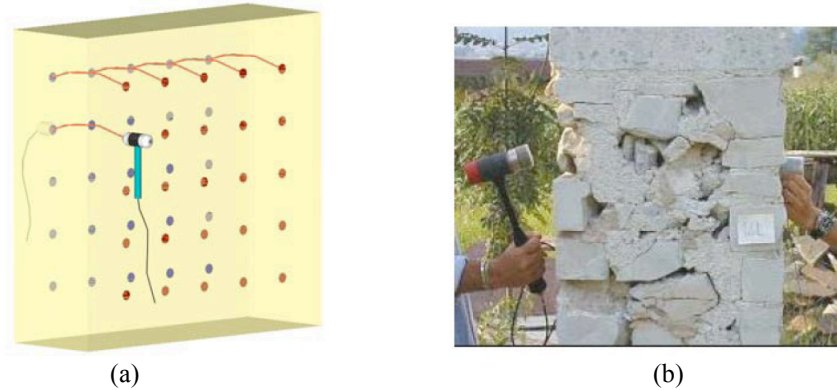(a)   (b)

Figure 5.6: Direct sonic test: (a) configuration; (b) in situ application [DELIVERABLE D11.1 (2004)].

(2)   <u>Semi-direct or radial transmission method</u>

In the semi-direct transmission method the transmitter and the receiver are located on adjacent sides of a corner or at acute angles on a column (Figure 5.6a).

(3)   <u>Indirect or superficial transmission method</u>

In this method, the transmitter and the accelerometer are positioned on the same side of the structural element. This configuration makes possible the identification of the characteristics of the outer layer of the masonry which can find significant application in the case of multi-leaf masonry walls. The depth of cracks, the consistency and the quality of the external layer can be evaluated. Nevertheless, with this method is not possible the acquisition of data for the total section due to the fact that the sonic wave cannot penetrate in a sufficient depth (Figure 5.6b).

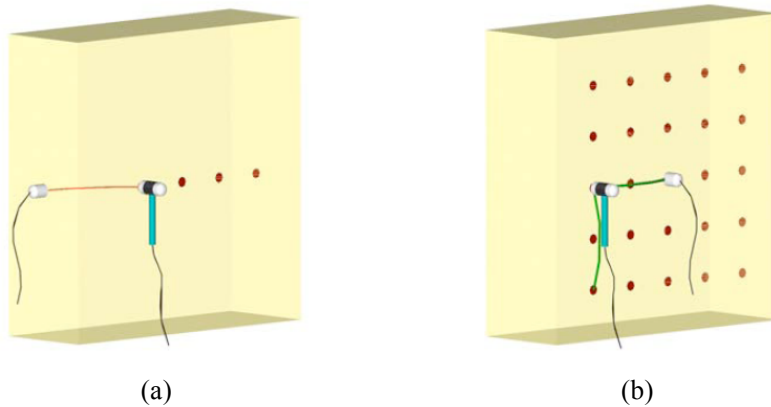<center>(a)   (b)</center>

Figure 5.6: (a) Semi-direct transmission test; (b) Indirect or superficial transmission test [DELIVERABLE D11.1 (2004)].

(4)   Sonic tomography method

This method which is the most complete comparing to the previous ones demands the use of multiple receiver sensors. In this way, the section is crossed by a dense net of ray paths with different recorded velocity for each one of them depending on the followed path (Figure 5.7). From the acquired results it is possible to reconstruct a 3D model of the velocity distribution which will give information about local velocity variations possibly correlated with weak zones or flaws in the internal fabric of the structure. Although that the sonic tomography is more precise than the other methods, it is far more time consuming complex in the implementation and requires high accuracy during the tests.
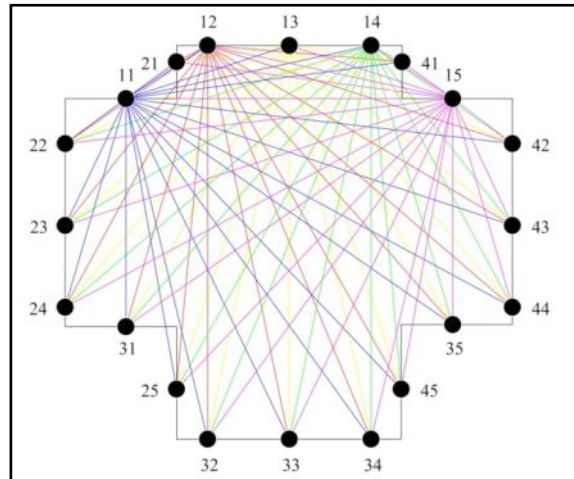
Figure 5.7: Sonic tomography ray paths in a pier of San Domenico church (courtesy of EXPIN).

Applicability

The main principal of the method is that since the thickness of the investigated structural element is known and the propagation time is measures, the velocity of the sonic wave can be calculated. From the velocity it can be taken information concerning the quality and the consistency of the structural element. Especially in the case of masonry walls, the velocity can be affected by the composition, the homogeneity, the presence of voids and the existence of cracks.

For the homogeneous, isotropic and with constant density materials, the relation connecting the velocity with the modulus of elasticity and the density is:

$$v = \sqrt{\frac{E}{\rho}}$$

Where,

v: the velocity of the sonic wave.

E: the Young's modulus of elasticity.

ρ: the density of the material.

It is obvious that since the masonry does not fulfil any of the homogeneity, isotropy and constant density criteria, the previous relation cannot be used qualitatively. Thus, the sonic pulse tests can be used mainly for comparison between the different areas of

112

the same structure in an effort to detect possible weak areas with voids or different materials and to make a rough estimation of the overall homogeneity and the consistency of the masonry walls. Nevertheless, a very interesting use of the method can take place for the evaluation of the effectiveness of conducted injection interventions. The sonic pulse test results after the injection can be compared with the ones before the intervention. The sufficient filling of the voids and discontinuities can be testified by the reduced wave propagation time measurements.

.

Sonic pulse velocity tests on San Domenico church

A total of 19 sonic tests were carried out on the San Domenico Church in L'Aquila. Two different configurations were employed for these tests, direct tests and tomographic tests. In the case of the direct tests, a grid of points was marked on either side of the material consisting of four rows of four points each for a total of sixteen test points as shown in Figure 5.8. The points were spaced 30cm apart both horizontally and vertically. Three trials were conducted for each point and the transmitting data from the hammer and the receiving data from the accelerometer were recorded.
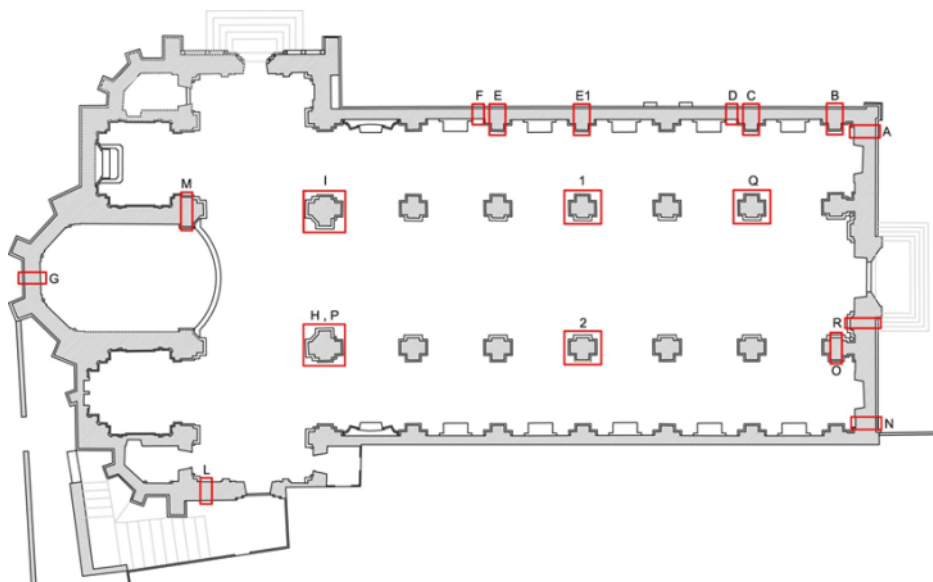

Figure 5.8: Locations of the sonic pulse velocity tests

Table 5.2: Sonic tests performed on the San Domenico church

113

Symbol	Typology of the test	Site
A	Square grid 4x4 with 30cm spacing	Perimeter wall
B	Square grid 4x4 with 30cm spacing	Perimeter pillar
C	Square grid 4x4 with 30cm spacing	Perimeter pillar
D	Square grid 4x4 with 30cm spacing	Perimeter wall
E	Square grid 4x4 with 30cm spacing	Perimeter pillar
E1	Square grid 4x4 with 30cm spacing	Perimeter pillar
F	Square grid 4x4 with 30cm spacing	Perimeter wall
G	Square grid 4x4 with 30cm spacing	Perimeter wall
H	Square grid 4x4 with 30cm spacing	Interior pillar
I	Plaster line with 30 cm spacing	Interior pillar
L	Square grid 4x4 with 30cm spacing	Perimeter wall
M	Square grid 4x4 with 30cm spacing	Internal masonry
N	Square grid 4x4 with 30cm spacing	Perimeter wall
O	Plaster line with 20 cm spacing	Interior pillar
P	Plaster line with 30 cm spacing	Interior pillar
Q	Plaster line with 30 cm spacing	Interior pillar
R	Square grid 4x4 with 30cm spacing	Perimeter pillar
TOMO1	Sonic tomography	Interior pillar
TOMO2	Sonic tomography	Interior pillar

The results of the test showed high variations between the velocity values among the different parts of the structure. Having the lowest velocity at 351m/s and the highest at 3365 m/s it can be assumed that the large range of the material density throughout the San Domenico church.

The different tested areas of the church were assessed regarding their homogeneity which is shown from the small variations of the velocities around the area and also regarding the density which is shown by high velocity values. Also, contour plots were created for the visualisation of the density maps and for the easier recognition of the problematic areas.

Table 5.3: Characterisation regarding the velocity range

Velocity range	Characterisation
0-550	Homogeneous and uniform
550-900	Fairly uniform
>900	Non uniform with inhomogenities

It was found that the exterior walls of the west and north sides of the church have inhomogenities and a high range of velocities although their average velocity is sufficiently high. The exterior walls of the facade and the east side of the church are more uniform and consistent but they have very low velocities which can be interpreted as lower density. The perimeter pillars were characterised by uniform velocities over the tested sections with some of them to appear high densities and others lower. Generally, despite local inhomogenities, the velocities are relatively high for all the pillars showing that good quality stones were used for these important support columns. The results of the tests with the material characterisation are summarised on the Table 5.4.

Table 5.4: San Domenico sonic pulse velocity tests comparison

Symbol	Site	Low	High	Average	Range	Notes
A	Perimeter wall	772	1418	994	646	Fairly uniform, good constituency
B	Perimeter pillar	909	1352	1093	443	Uniform, sufficiently high
C	Perimeter pillar	1051	1790	1396	739	Fairly uniform, high density
D	Perimeter wall	845	3365	2268	2520	Inhomogenities however very high density in some parts, partial detachment of plaster in low speed area
E	Perimeter pillar	879	1397	1043	518	Uniform, sufficiently high
E1	Perimeter pillar	441	805	564	364	Uniform, low
F	Perimeter wall	480	1541	913	1063	Inhomogenities, low values
G	Perimeter wall	660	1890	1303	1230	Inhomogenities, high values
H	Interior pillar	691	2487	1137	1796	Relatively homogeneous with edges distorting the range, high density
I	Interior pillar	656	2160	1246	1504	Inhomogenities, high values
L	Perimeter wall	351	949	704	418	Uniform, low
M	Internal masonry	1051	1790	1319	418	Uniform, low
N	Perimeter wall	531	949	704	418	Uniform, low
O	Interior pillar	1051	1790	1034	739	Fairly uniform, high density
P	Interior pillar	665	2023	907	1358	Uniform and low in centre, high density on outer edges
Q	Interior pillar	586	2305	1220	1719	Inhomogenities, high values at edges
R	Perimeter pillar	559	1175	699	616	Fairly uniform

115

5.5.2 Flat jack tests

Single flat jack test

Description

The single flat jack test is used for in-situ determination of the state of stress based on the stress relaxation caused by a cut perpendicular to the wall surface. The test is based on the principle of partial stress release and involves the local elimination of stresses, followed by controlled stress compensation (Figure 5.9). The stress state is determined by a partial closing of the cutting.
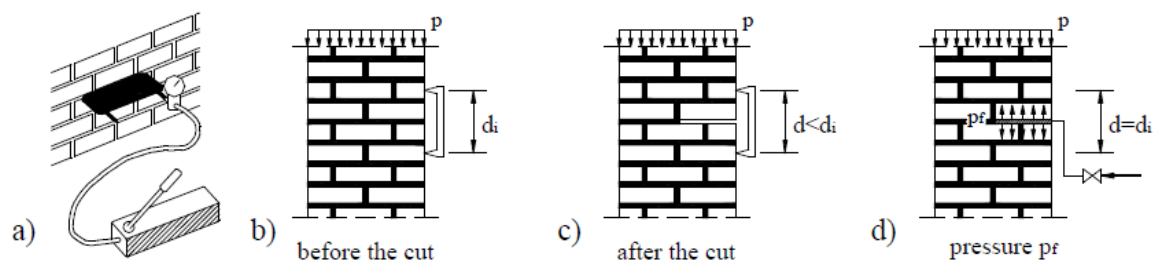

Figure 5.9: Phases of the Flat jack test [Gregorczyk and Lourenço (2000)].

The proper instructions for the test are described by the RILEM Standard [MDT D.4] and the [ASTM C 1196-91] ,according to which the slots is necessary to be parallel, vertically aligned and separated by at least 3 courses of masonry in case of unit height equal to or greater than 100mm for stone masonry. The use of thin steel sheets is necessary for packing tightly the inserted jacks. Those sheets will protect the jack membrane from local swelling especially in the case of internal voids. The gradual increase in increments of less than 10% of the maximum expected compressive strength must be done until the initial distances are almost achieved. In practice the initial geometry cannot completely retrieved. Finally the cuts are restored with the proper and compatible with the masonry mortar.

According to the RILEM Standard and Recommendations MDT. D.4, the restoring stress value is given by the relation:

$$S K_{fel} p \times \times \quad \frac{A_{slot}}{A_{je}}$$

Where,

K_e: a dimensionless geometrical efficiency constant which takes into account the position of the slot in relation to the mortar joints, the relative size of the jack and the units and the geometrical characteristics of the jack.

p: the pressure which restores the initial strain condition.

A_{slot}: the area of the slot Slot / jack area constant.

A_{je}: the effective area of the flat jack.

Applicability

The main application of the single flat jack test is the determination of the compressive stress state in a specific area of a masonry wall. By comparing the variation of the results in different parts of wall it can be evaluated the consistency and the quality of the masonry. Moreover, the knowledge of the stress state contributes in a better understanding of the behaviour of the structural system and of its pathology leading to a more sufficient and accurate intervention proposal.

Double flat jack test

Description

The method of the double flat jack is applied in order to determine the deformability characteristics of the masonry. A second cut is made parallel to the previous cut at a distance of at least 40-50cm. In this way the two jacks delimit a masonry sample of appreciable size to which a uni-axial compression stress is applied. The procedure is the same as with the Single Flat jack test. The jacks are inserted and packed tightly into the cut using thin steel sheets is necessary. During the test, the ratio of the increase of jack pressure (Δp) to the strain increment Δe_m is monitored and once the ratio starts dropping rapidly the procedure has to be ended.

117

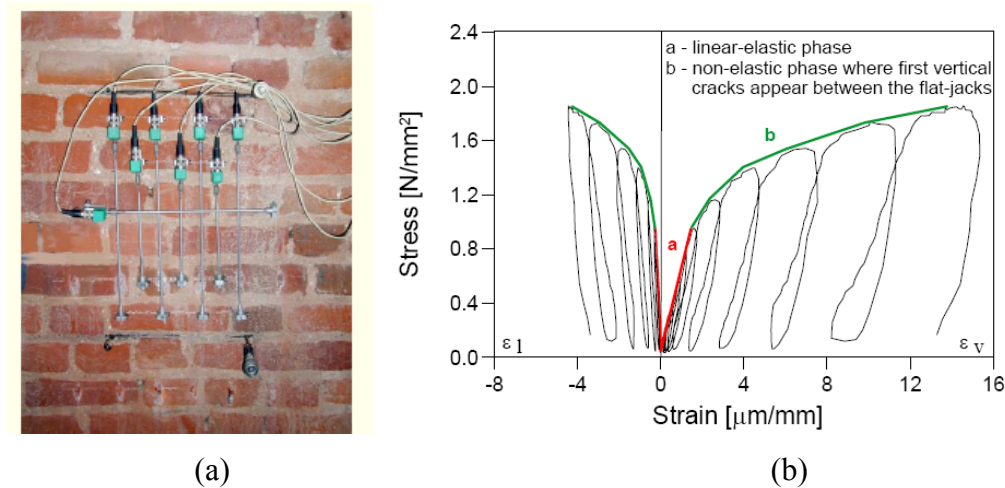(a)   (b)

Figure 5.10: Double flat jack test (a) typical installation [Binda and Tiraboschi (1999)]; (b) typical results with the different phases [Binda *et al.* (2007)].

Applicability and limitations

The double flat jack technique can be used for the identification of the deformability characteristics of the masonry. Through extended campaigns and acquired data it has been possible to find a qualitative relationship between the value of the elastic modulus and the building typology. Thus, it is possible the results of each case study to be compared with this data in order to be verified their validity.

Nevertheless, multiple difficulties are presented in the estimation of the elastic face of the masonry and in the calculation of the elastic modulus.

According to the ASTM [(1991a; 1991b)] and RILEM [(1990a; 1990b)] proposal the value of E can be calculated as:

$$E_t = \frac{\int O_{mi}}{\int J_{mi}} \qquad \text{tangent modulus}$$

Where,

$\delta\sigma_{mi}$: the increment of the stress σ at each step of loading

$\delta\varepsilon_{mi}$: the increment of the strain ε at each step of loading.

$$E_{si} = \frac{O_{mi}}{J_{mi}} \qquad \text{secant modulus}$$

Where,

$\delta\sigma_{mi}$: the value of the stress σ reached at step i.

$\delta\varepsilon_{mi}$: the increment of the strain ε at each step of loading.

118

The first way of the tangent modulus is significantly easier and it given by the variation of E along the envelope of the loading curve. The secant modulus is more difficult and complex in the calculation when there is a locking phase. Often, the elastic modulus is calculated as secant modulus in the linear part of the σ-ε diagram. Thus, the choice of the secant modulus depends much more on the operator decision [Binda *et al.* (2007)].
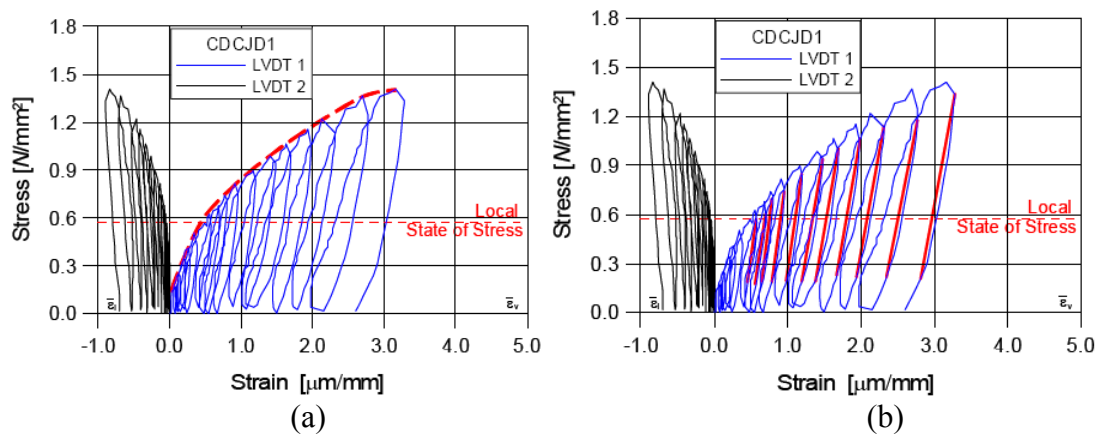

Figure 5.11: Calculation of (a) tangent modulus of elasticity; (b) secant modulus of elasticity [Binda *et al.* (2007)]

Flat jack tests on San Domenico church

A group of eight single flat-jack tests of the cylinder cross section and of seven double flat-jack tests were carried out. The object of those tests was to the determination of the stress state and deformation characteristics of the masonry walls. This data can be used for the assessment of the mechanical properties of the wall and for the calibration a finite element model.

The tests were carried out with reference to the following standards:
• ASTM C 1196-91 - In Situ Compressive Stress Within Solid Unit Masonry estimated using flat jacks Measurements;
• ASTM C1197-91 - Standard test method for in situ measurement of masonry deformability properties using flat-jack method;
• RILEM Lum 90 / 2 Lum.D.2. - In situ stress based on the flat jack;
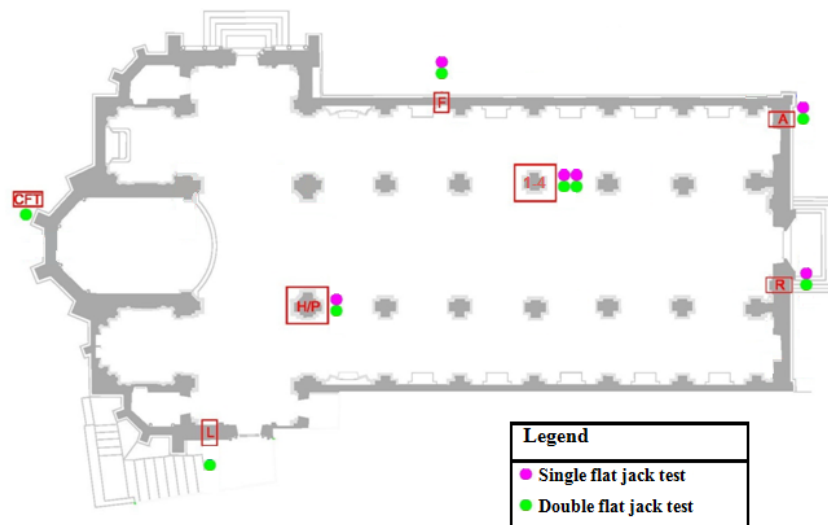• RILEM Lum 90 / 2 LumD3 - In situ strength and elasticity tests based on the flat-jack.

119

Figure 5.12: Position of single and double flat-jack tests in the Church of San Domenico

Test Details and Results

Single flat jack test SFJ-HP

The single flat jack test SFJ-HP took place at the end of the nave, in front of the apse. The cut was done at the height of 117 cm from the ground level and it had a length of 50 cm. A total of five sensors were positioned for the measurement of the displacements. The local stress value at this position was found 0.34 N/mm^2.
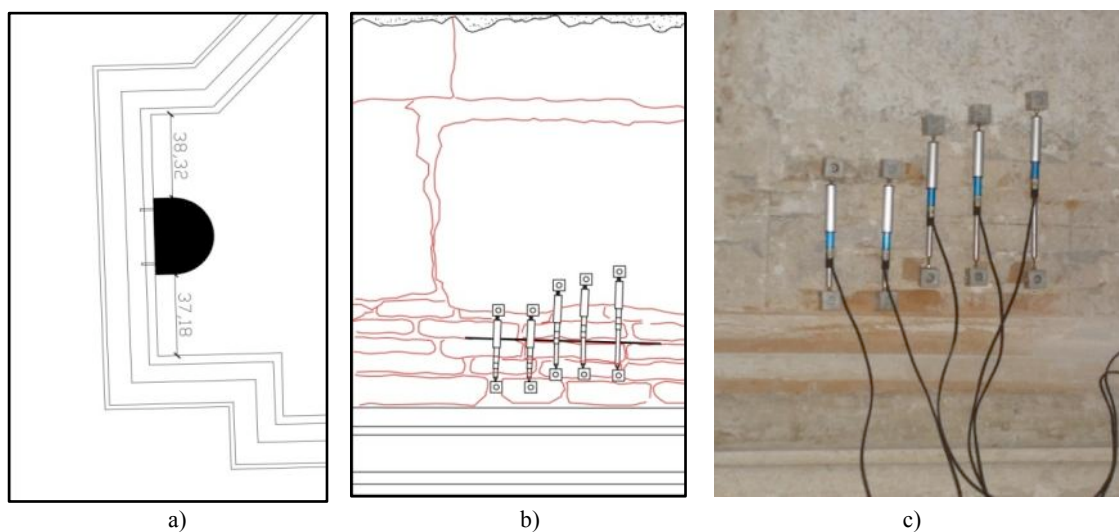

Figure 5.13: Single flat jack test SFJ-HP; (a) localisation on the floor plan; (b) Identification of displacement sensors; (c) measurement of the initial distances (courtesy of EXPIN)..
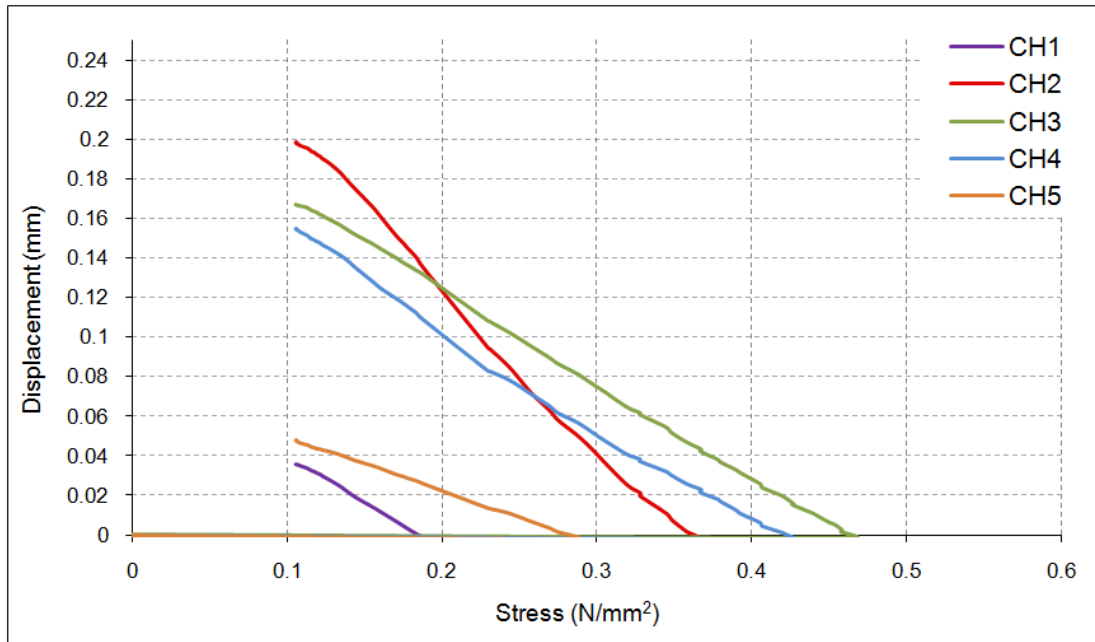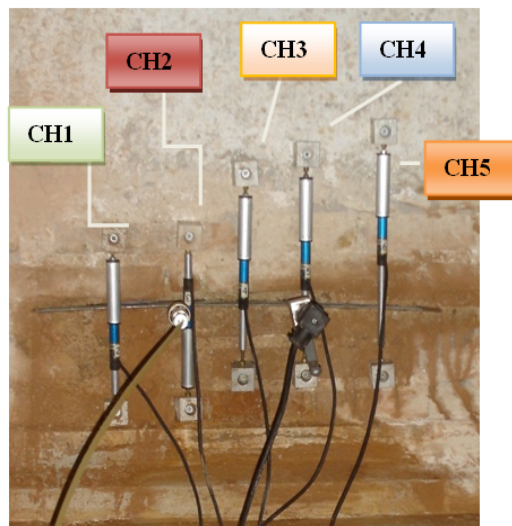
120

Figure 5.14 Stress state-displacement diagram for the single flat jack test SFJ-HP.

Table 5.5: Compressive stress for the SFJ-HP test.

Compressive stress for the compensation of the displacements (reset)	
Sensor 1 (CH1)	0.18 N/mm^2
Sensor 2 (CH2)	0.36 N/mm^2
Sensor 3 (CH3)	0.46 N/mm^2
Sensor 4 (CH4)	0.42 N/mm^2
Sensor 5 (CH5)	0.28 N/mm^2
Mean lavue (σ local)	**0.34 N/mm^2**

Single flat jack test SFJ-A

The single flat jack test SFJ-A was conducted at the interior side of the perimeter wall at the south-west side. The cut was done at the height of 35cm from the ground level and it had a length of 35cm. A total of four displacement sensors were used for the measurement of the displacements. The average value of the stresses for the SFJ-A was found to be 0.23 N/mm^2. It has to be mentioned that this value matches very well with the SFJ-F which was also done on the perimeter wall of the church and had the value 0.21 N/mm^2.

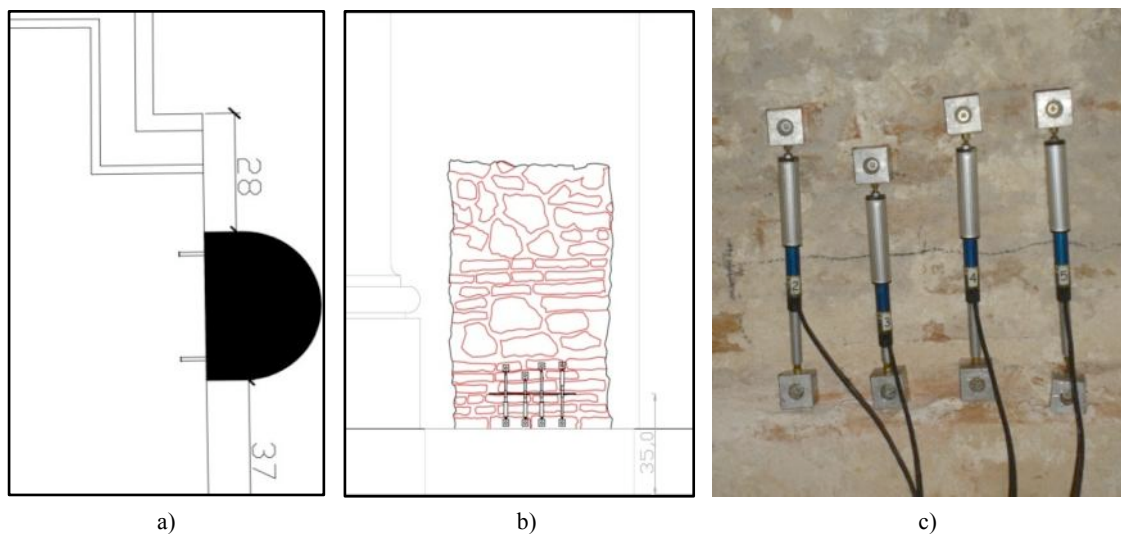a)   b)   c)

Figure 5.15: Single flat jack test SFJA; (a) localisation on the floor plan; (b) Identification of displacement sensors; (c) measurement of the initial distances (courtesy of EXPIN)..
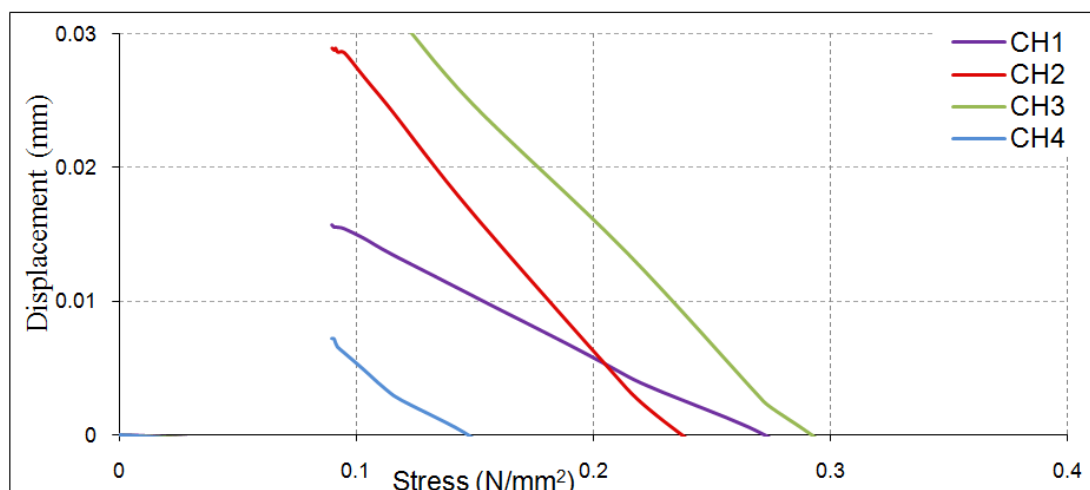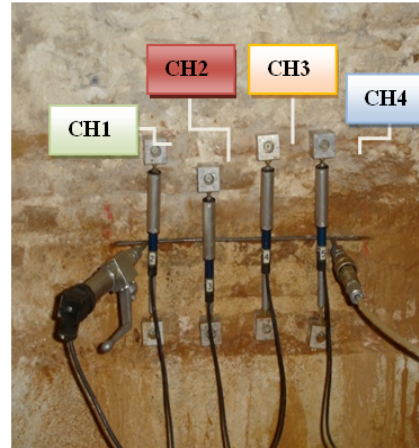

Figure 5.16: Stress state-displacement diagram for the single flat jack test SFJ-HP

122

Table 5.6: Compressive stress for the SFJ-A test.

Compressive stress for the compensation of the displacements (reset)	
Sensor 1 (CH1)	0.25 N/mm^2
Sensor 2 (CH2)	0.23 N/mm^2
Sensor 3 (CH3)	0.29 N/mm^2
Sensor 4 (CH4)	0.14 N/mm^2
Mean lavue (σ local)	**0.23 N/mm^2**

Single flat jack test SFJ-CFT

The cut was done at a height of 90cm measured from the ground level and the cutting was done in the middle of the buttress with the length of 35cm at the outer perimeter of the posterior wall of the apse. At this point, the masonry quality is believed to be quite good, made of regular stone with no light wells or voids near the point of testing. Four sensors were used in the vertical direction. The result of the local stress was found to be 1.54 N/mm^2 which is significantly higher than the other single flat jack tests.
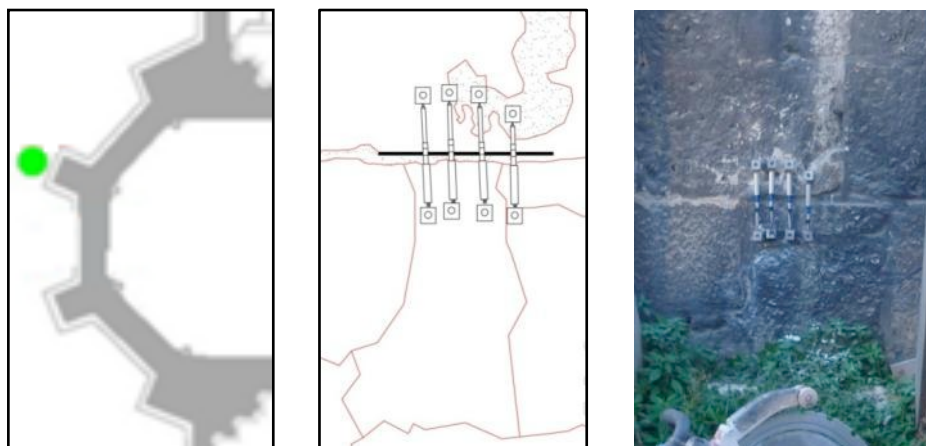
Figure 5.17: Single flat jack test SFJ-CFT (courtesy of EXPIN)..

123

Figure 5.18: Stress state-displacement diagram for the single flat jack test SFJ- CFT

Table 5.7: Compressive stress for the SFJ-CFT test.

Compressive stress for the compensation of the displacements (reset)	
Sensor 1 (CH1)	1.84 N/mm^2
Sensor 2 (CH2)	1.59 N/mm^2
Sensor 3 (CH3)	1.20 N/mm^2
Sensor 4 (CH4)	1.55 N/mm^2
Mean lavue (σ local)	**1.54 N/mm^2**

124

Double flat jack test DFJ-HP
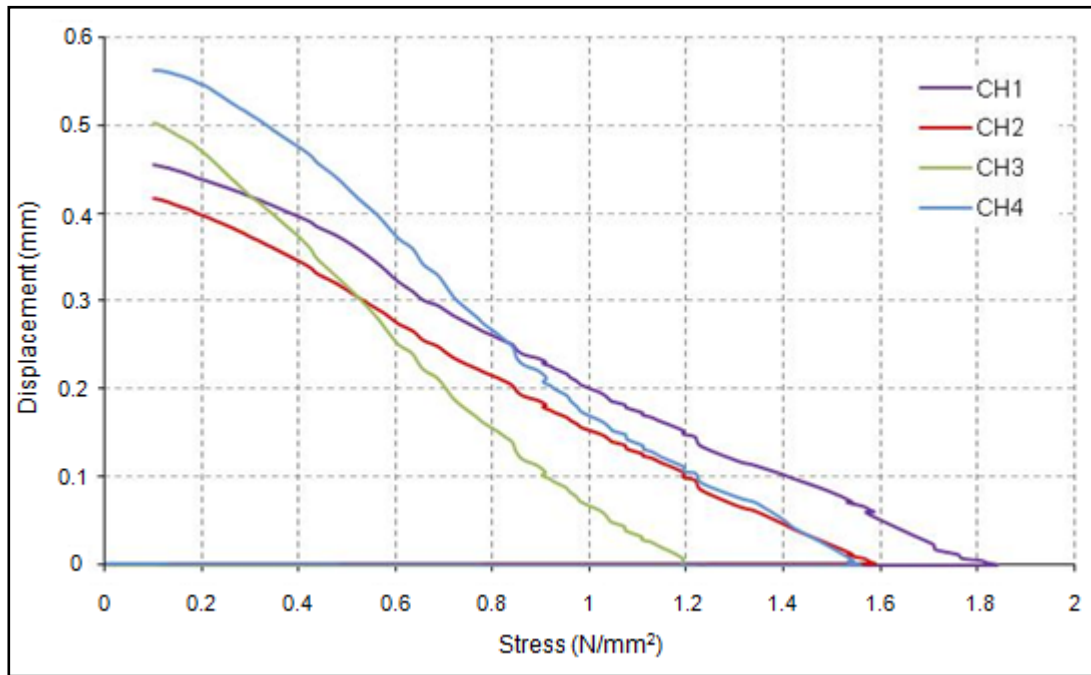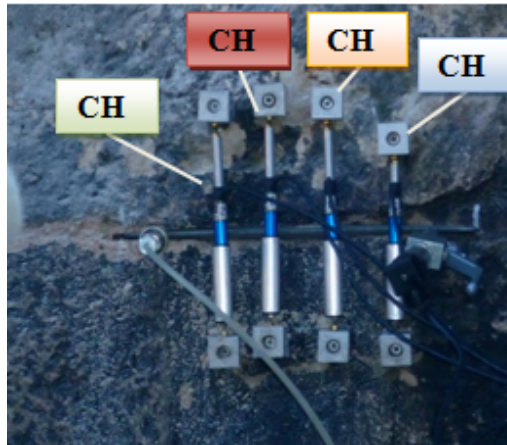
The double flat jack test DFJ-HP was done at the same are with the previous single flat jack test SFJ-HP in a position 58 cm higher than the other cut. Five vertical displacement sensors were also used in this case for the measurement of the displacements caused by cyclic loading.

a)   b)

Figure 5.18: Double flat jack test in position DFJ-HP (courtesy of EXPIN)..

Figure 5.19: Diagram of stress-deformation development for all the sensors of the double flat jack test DFJ-HP.

125
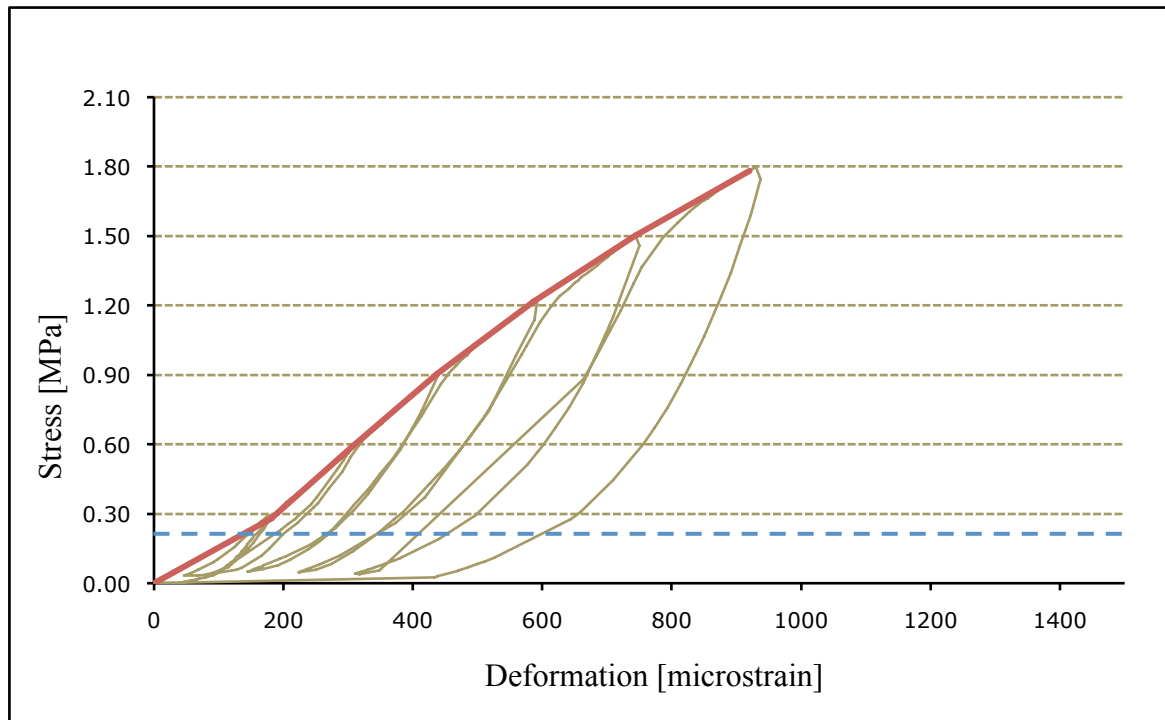
Figure 5.20: Mean diagram of stress-deformation development for the double flat jack test DFJ-HP.

Figure 5.21: Variation of unloading coefficient for the calculation of the Young's modulus of elasticity for the double flat jack test DFJ-HP.

Table 5.8: Calculation of the moduli of elasticity from the double flat jack test DFJ-HP.

Modulus of tangent elasticity E_{tan} [N/mm^2]	$\Delta (\sigma)$ [N/mm^2]	Modulus of elasticity from the unloading segment E_{sec} [N/mm^2]	$\Delta (\sigma)$ [N/mm^2]
1544	0.00-0.30		
2468	0.30-0.60	1544	0.60-0.30
2402	0.60-0.90	3517	0.90-0.30
2099	0.90-1.20	4547	1.20-0.30
1798	1.20-1.50	5014	1.50-0.30
1601	1.50-1.80	4871	1.80-0.30
1985	**Mean**	**3899**	**Mean**

Double flat jack test DFJ-A

The double flat jack test was done at the same are with the previous single flat jack test SFJ-A, SFJ-HP in a position 46 cm higher than the previous cut. Four displacement sensors were placed in the vertical direction and one in the horizontal for the measurement of the displacements caused by cyclic loading.

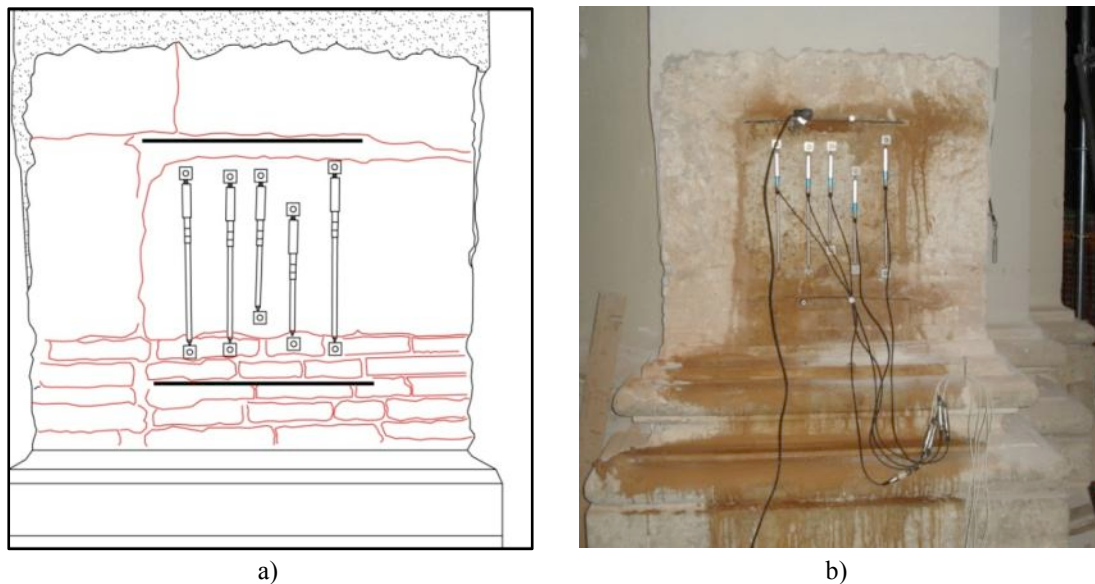a)   b)   c)

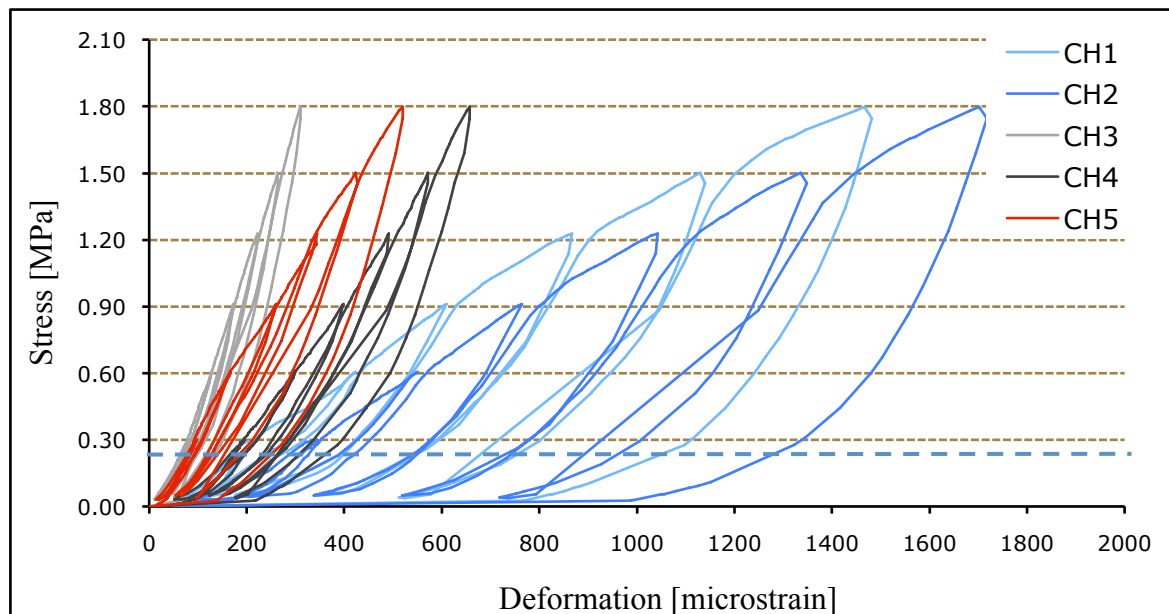Figure 5.22: Double flat jack test in position DFJ-A (courtesy of EXPIN)..

127
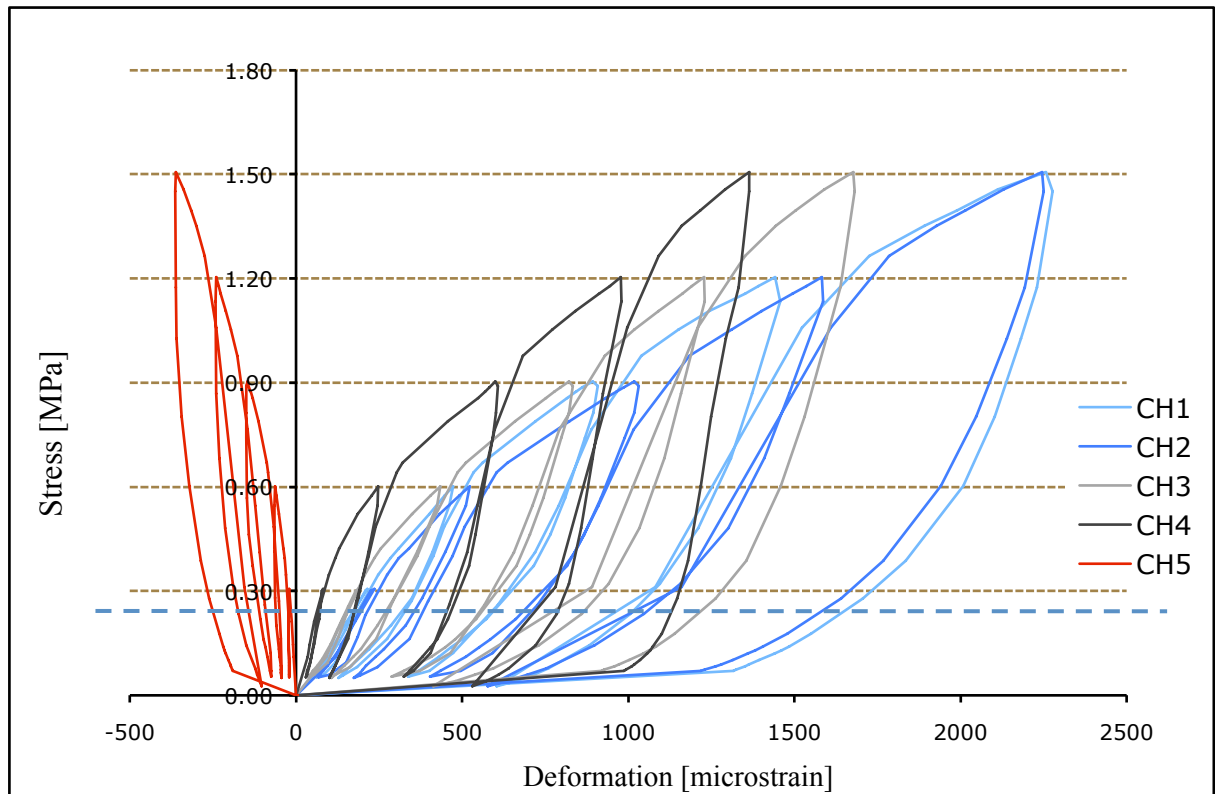
Figure 5.23: Diagram of stress-deformation development for all the sensors of the double flat jack test DFJ-A.

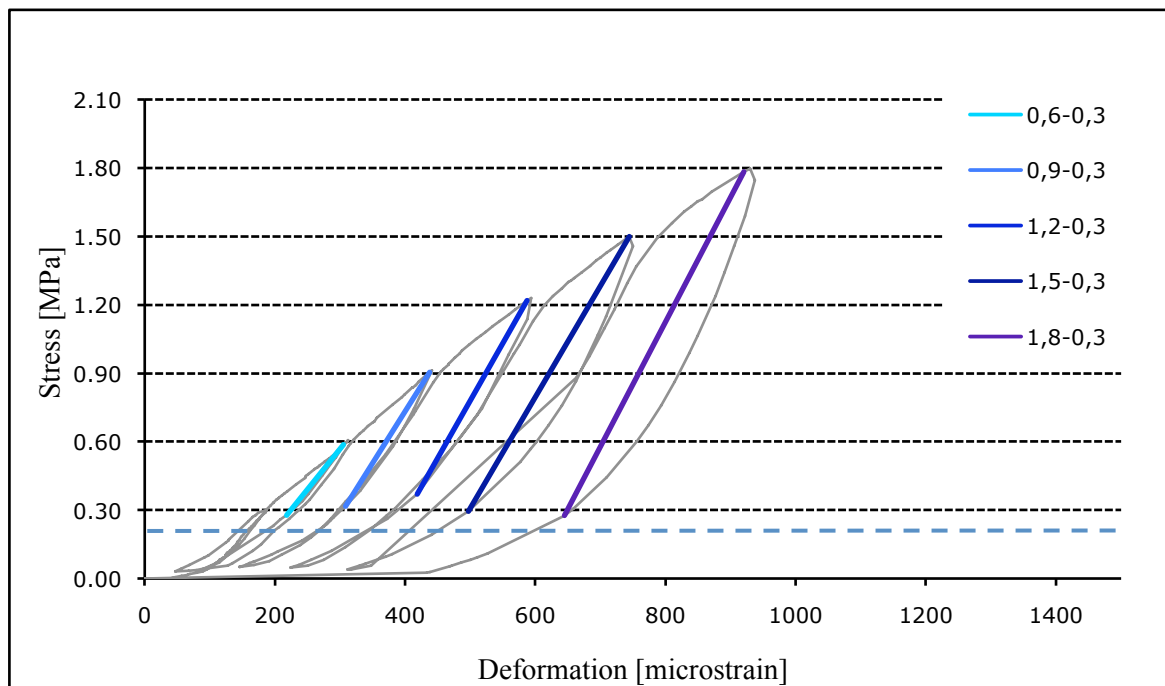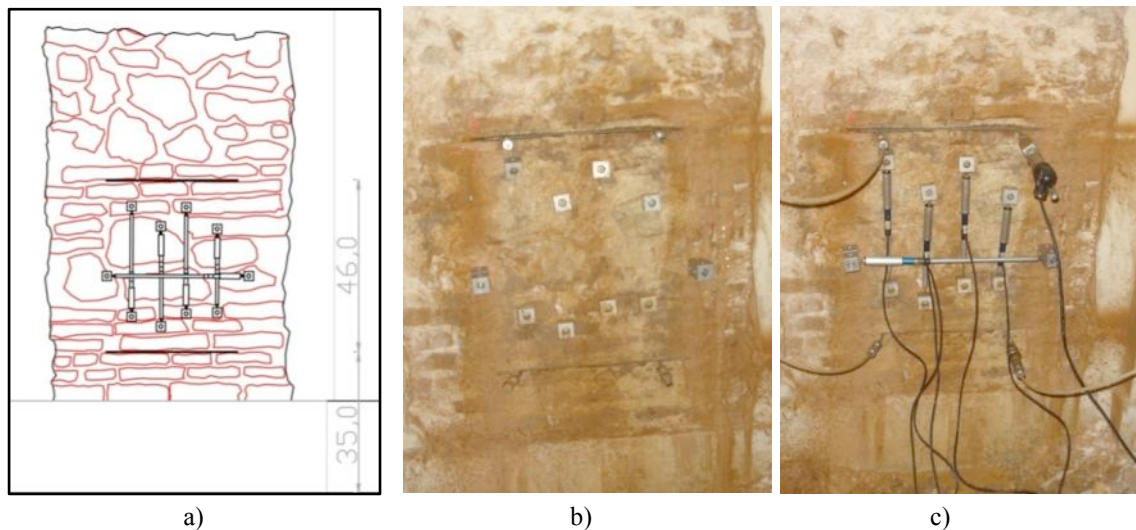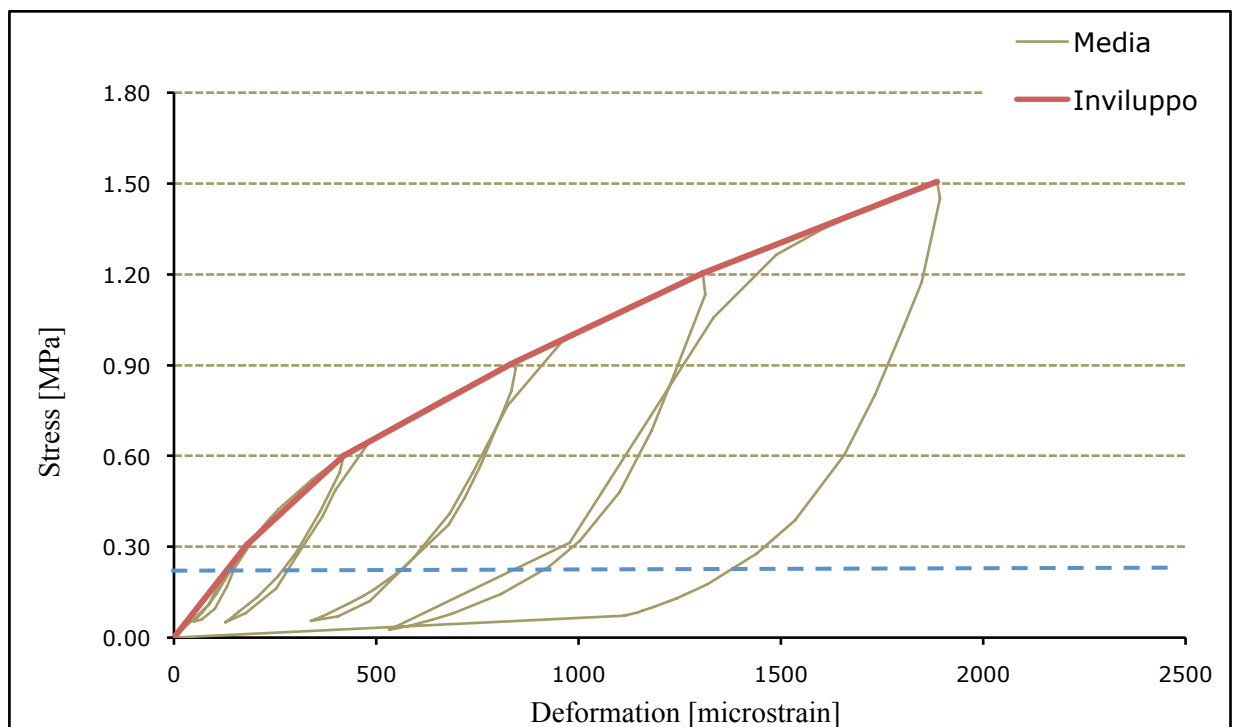Figure 5.24: Mean diagram of stress-deformation development for the double flat jack test DFJ-A.

128
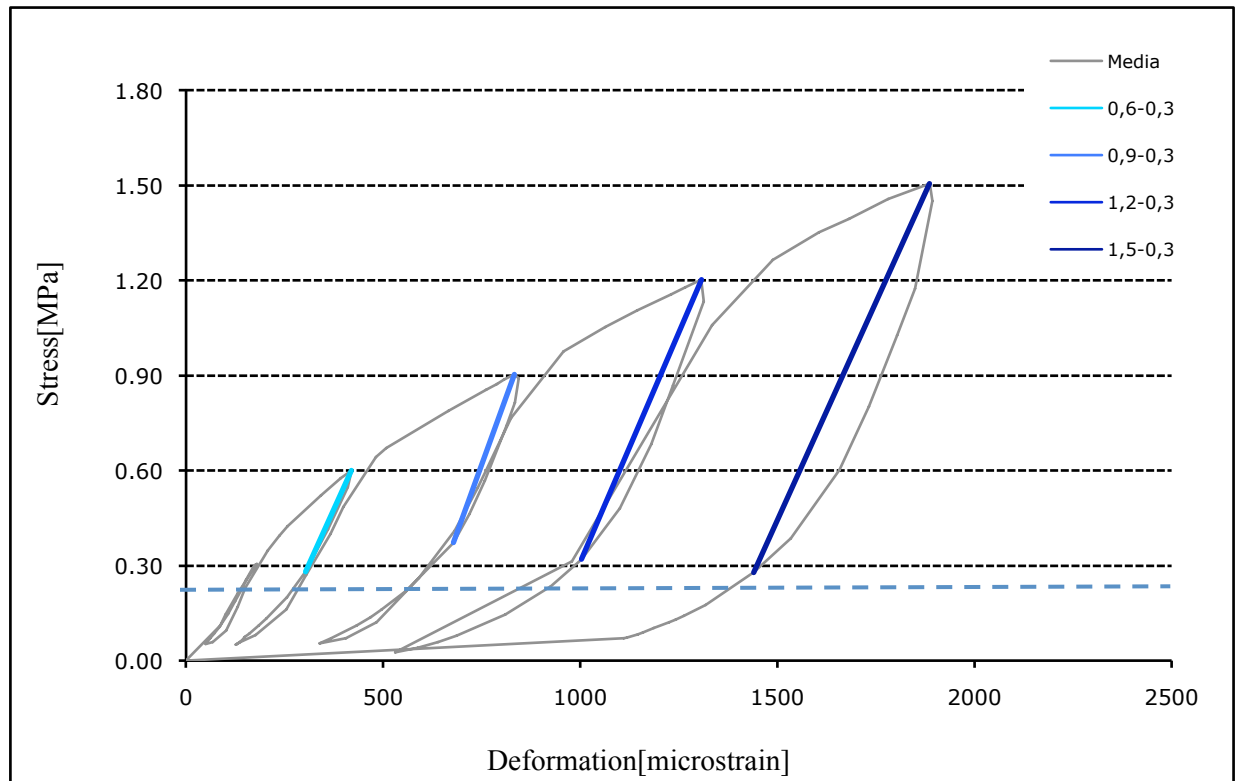
Figure 5.25: Variation of unloading coefficient for the calculation of the Young's modulus of elasticity for the double flat jack test DFJ-A.

Table 5.9: Calculation of the moduli of elasticity from the double flat jack test DFJ-A

Modulus of tangent elasticity E_{tan} [N/mm^2]	Δ (σ) [N/mm^2]	Modulus of elasticity from the unloading brunch E_{sec} [N/mm^2]	Δ (σ) [N/mm^2]
1703	0.00-0.30		
1230	0.30-0.60	2740	0.60-0.30
734	0.60-0.90	3446	0.90-0.30
630	0.90-1.20	2902	1.20-0.30
524	1.20-1.50	2751	1.50-0.30
964	**Mean**	**2960**	**Mean**

Summary of the flat jack tests

The results of all the flat jack tests are presented in the Table 5.10. All the values seem to be similar except from the one occurred by the test SFJ-F which are significantly higher.

129

Table 5.10: Summary of the results of the double flat jack test in the church of San Domenico

Test	σ_{local} [N/mm^2]	E_{tg} [N/mm^2]	$E_{unloading}$ [N/mm^2]
SFJ - L	0.42	-	-
SFJ/DFJ - HP	0.34	1985	4159
SFJ/DFJ - F	0.21	(4641)	(10215)
SFJ/DFJ - R	0.60	1511	3203
SFJ/DFJ - A	0.23	964	2960
SFJ/DFJ -1-2	0.55	1201	2672
SFJ/DFJ-1-4	0.41	1142	2449
SFJ - CFT	1.54	-	-
Mean value including F		1907	4276
Mean value excluding F		1361	3088

The average value of the tangent modulus of elasticity is 1907 N/mm^2 and of the modulus of elasticity from the unloading brunch 4276 N/mm^2. If the results of the test SFJ-CFT filtered out, the value of the tangent and unloading brunch modulus of elasticity are 1361 N/mm^2 and 3088 N/mm^2 respectively. Those last values will be is believed to represent better the reality and thus they will be adopted. Those values it can be compared with the Italian regulations [Istruzioni per l'applicazione delle "Nuove norme tecniche per le costruzioni", (2009)] which give a range values depending of the masonry typology. The under study masonry can be categorised as "cut-split stone masonry with good texture" for which the given value of the modulus of elasticity is between 1500 N/mm^2 and 1980 N/mm^2 (Table 5.11). The fact that the recommended values are close to the ones experimentally occurred validates the overall testing procedure.

Table 5.11: Part of the table C8A.2.1 of the italian regulation [Istruzioni per l'applicazione delle "Nuove norme tecniche per le costruzioni"(2009)].

Masonry typology	f_m	τ_0	E	G	w
	(N/cm^2)	(N/cm^2)	(N/mm^2)	(N/mm^2)	(kN/m^3)
Cut-split stone masonry with good texture	Min-Max	Min-Max	Min-Max	Min-Max	
(*Muratura in pietra a spacco con buona tessitura*)	260	5.6	1500	500	21
	380	7.4	1980	600	

130

5.5.3 Schmidt hammer tests

Description

The Schmidt hammer is non-destructive method used for the determination of the hardness of a concrete element. The penetration resistance of the Schmidt rebound hammer on the material surface can give determine indirectly the compressive strength of the concrete. Due to the fact that this is a localised method, it can also be used for identifying deterioration in the concrete. Areas of deterioration and interior cracking will produce a lower rebound when compared with other areas on the same concrete element with high consistency. The [ASTM C805] can be used for the standardisation of the process.

The impact of a spring loaded mass against the surface is measured taking into account the already defined energy that is released during the test. The rebound distance is dependent on the hardness of the material, the angle of the instrument to the material, the gravity and the moisture content of the material. A smooth and flat portion of the surface must be selected for the purpose of the testing. The inclination of the hammer in respect to the direction of the gravity is a highly affecting factor giving higher rebound for a vertical position of the hammer on the underside of the sample [FIB 17 (2002)]. In the conversion charts the correction of the results on respect of the angle is also possible. The results of the Schmidt hammer test are on an arbitrary scale from 10 to 100 and must be converted using the manufacturer's provided tables. Since the method gives results only for localised areas, an important number of samples is necessary for the proper estimation of the material strength in order to avoid the local variations of the material. Any outlying values must be filtered in the calculation of the average results. Finally, it needs to be mentioned that although the Schmidt hammer test is an easily applicable and non-destructive method and thus very useful for historical structures, its indirect results cannot substitute the direct results which can be given by compression test on core samples.

Schmidt hammer tests on San Domenico church

In the case of San Domenico Church, the Schmidt rebound hammer was used to determine the strength characteristics of the concrete trusses supporting the roof above the main transept of the church. Those trusses are part of a previous intervention and they replaced the original timber truss structures of the church. The strength of the concrete is not known and it had to be identified with the Schmidt hammer method. The tests were performed horizontally in order to avoid the necessary correction which otherwise would be needed due to the effect of the gravity. The results of the tests are shown in detail in the report by. The results indicate that the compressive strength of the concrete is between 25 N/mm^2 and 34 N/mm^2 with lower values for the truss structure over the nave. The locations of the Schmidt hammer test and the pacometer tests which also are going to be described are presented in the Figure 5.27.

Figure 5.26: Classification of concrete strength by Schmidt hammer on San Domenico roof trusses (courtesy of EXPIN).
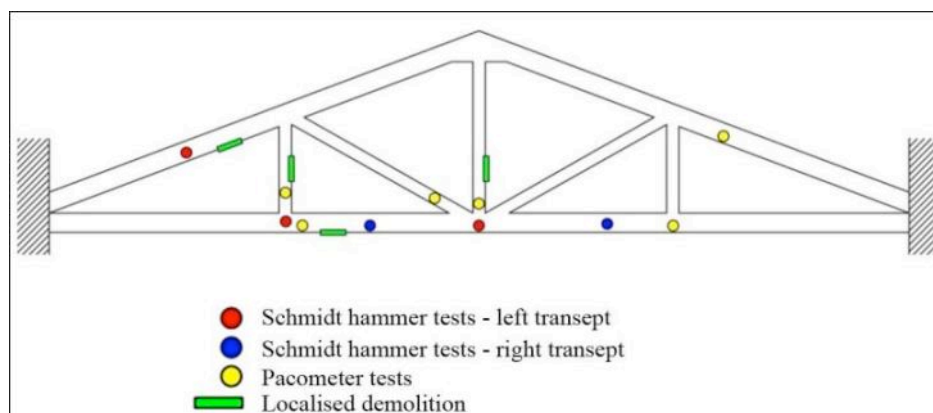

Figure 5.27: Test locations for the investigation of the concrete trusses supporting the roof over the transept (courtesy of EXPIN).

132

5.5.4 Pacometer tests

Description

The pacometer is a non-destructive testing device used to detect metals within complex elements. In investigation of historic structures this electromagnetic device can help in determining the presence and location of metals, such as reinforcement bars, iron cramps, ties, or other metal pieces, within the existing concrete or masonry.

Pacometer tests on San Domenico church

As it has already mentioned, the concrete trusses were built during a previous intervention for which the geometrical characteristics of the steel reinforcement were not known and thus they had to be identified. The pacometer tests were aimed at identifying the locations of the reinforcement bars within the truss members, the depth of the cover, and the reinforcement diameter. The mapping of the reinforcement was achieved moving the pacometer probe across the surface of the structure. The difference in the magnetic properties between the reinforcement and the concrete is detected, processed, displayed on the display screen, and stored in the receiver. Later on the stored images were analysed and sections and rebar locations were determined as it is shown in the Figure 5.28.

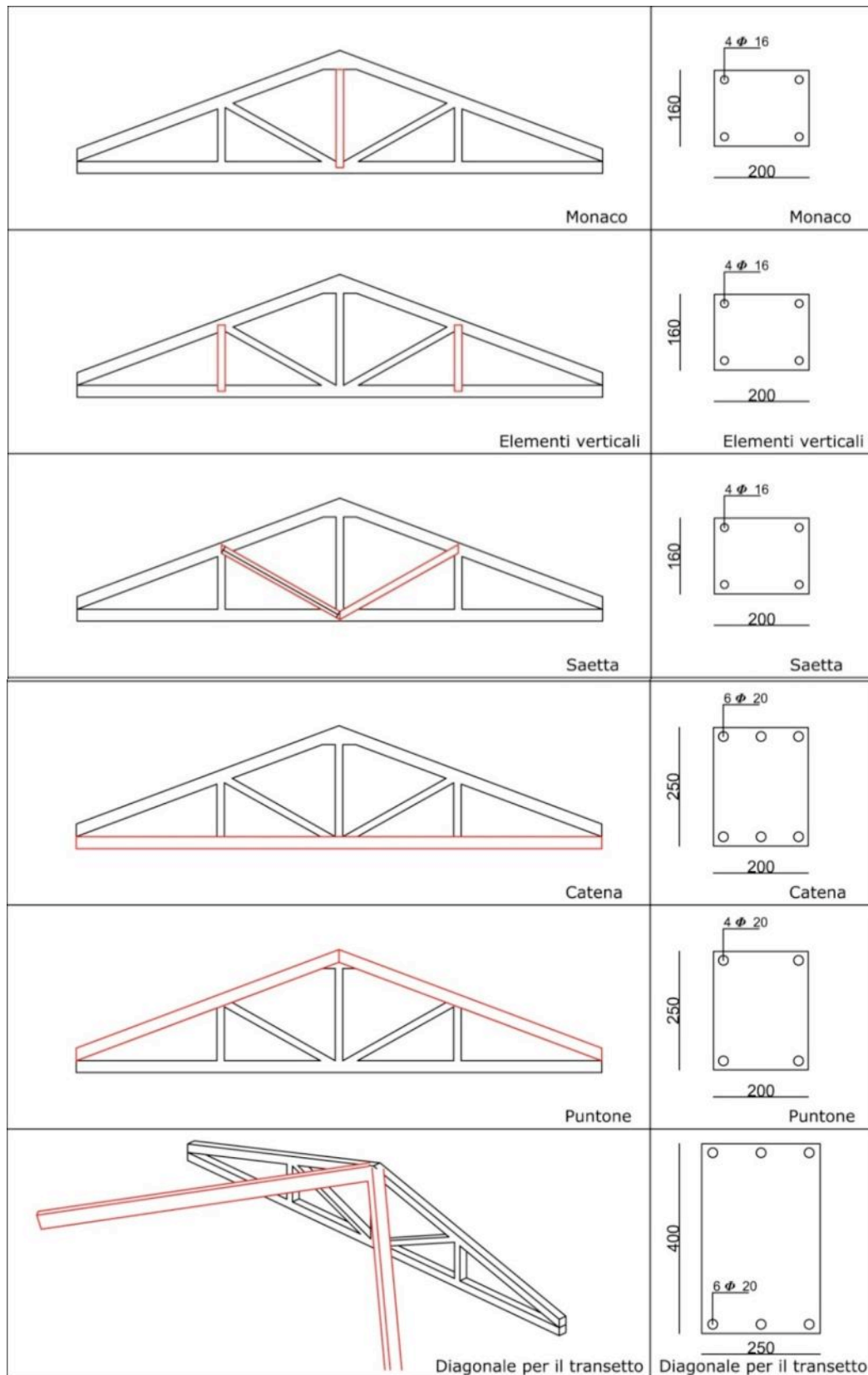Figure 5.29: Pacometer testing of truss beams in San Domenico Church (courtesy of EXPIN).

133

Figure 5.30: Locations of steel reinforcement in each truss element determined via pacometer testing (courtesy of EXPIN).

5.5.5 Dynamic identification tests

Description

The dynamic identification is a non destructive technique used for the investigation of the characteristics of a structure and of its global behaviour through a modal analysis. Being the only method which is able to experimentally identify the behaviour of a structure, its importance in combination with the other tests is high for the study of a structure and for the creation and the calibration of its model.

The first stage of this technique is the excitation of the structure. This can take place using different excitation mechanisms. The choice of the excitation function depends on the equipment available, the characteristics of the structure to be measured, measurement considerations, and the length of time for the proposed measurement. Shakers can be used to induce large forces in the structure but they are expensive and caution must be taken not to cause damage by inducing resonance. Lower energy excitation sources that are cheaper are impact hammers and drop weight systems. Random ambient vibrations caused by traffic, wind, people, and vibrations of the earth can also be used [Gentile (2007)].

The next stage contains the acquisition of the signal and later on the digitalisation. For the signal acquisition different response transducers can be selected in order to measure the accelerations of the structure considering the frequency range, dynamic range, operating frequency, and the ruggedness of the sensor for the environment it will be used in. In the case of the San Domenico Church investigation, piezoelectric accelerometers were used. These accelerometers have the advantage of not requiring external power (important for locations without power after damage from an earthquake), being stable, having a good signal to noise ratio, and having a wide frequency and dynamic range. The transducers measure the accelerations at different points of the structure and then transmit this data to the data acquisition system where it is recorded through a discrete time series. Finally a digital computer is used for the receiving the further process of the signal.

The last stage includes the modal analysis of the structure. Though this, the modal parameters that can be determined are the frequency, damping, and mode shapes.

135

These characteristics can then be related to such physical and mechanical characteristics of the building as the mass, stiffness, and energy dissipation has to be mentioned though that although during this method the linear structural characteristics are usually investigated but structural problems could be nonlinear. Moreover there is the possibility some of the modal frequencies which are close together not to be able to be detected.

Dynamic identification tests on San Domenico church

The dynamic investigation was carried on the San Domenico Church in order to determine the dynamic characteristics and level of damage following the April 6, 2009 earthquake. The high complexity of the geometry of the structure made necessary the use of this method in order to build a reliable model. The test campaign was also performed by the EXPIN Ltd. company.

Test Setup

The excitation method which was decided to be used was the "Output Only" technique which uses only ambient vibrations from the environment as the input signal. Those ambient vibrations, not having predominant frequencies, give the analyst the ability to identify the natural frequencies of the church only on the basis of its response.

In order to select the different positions for the realisation of the tests; a modal analysis of a preliminary finite element model was used. This modal analysis showed the areas with lower stiffness which were usually correlated with higher natural frequencies like the nave bending. The 28 different monitoring positions of the vibration on two different levels of the nave of the church were selected according to the information acquired from the modal analysis, the experience of other dynamic tests and from the observation of the damaged areas.

Eight sensors were used in the dynamic testing. For the achieving of a more comprehensive study of this section of the structure and in order to collect data from all 28 positions, five test configurations were used maintaining throughout all tests

two reference sensors in fixed positions in mutually perpendicular directions. The sensors on the lower level (Level A) were located on bearing walls at a height of 14 meters, corresponding to the height of the spring of the arches of the nave. The second level sensors (Level B) where placed at the level of the springing of the roof. The levels are shown in Figure 5.31.
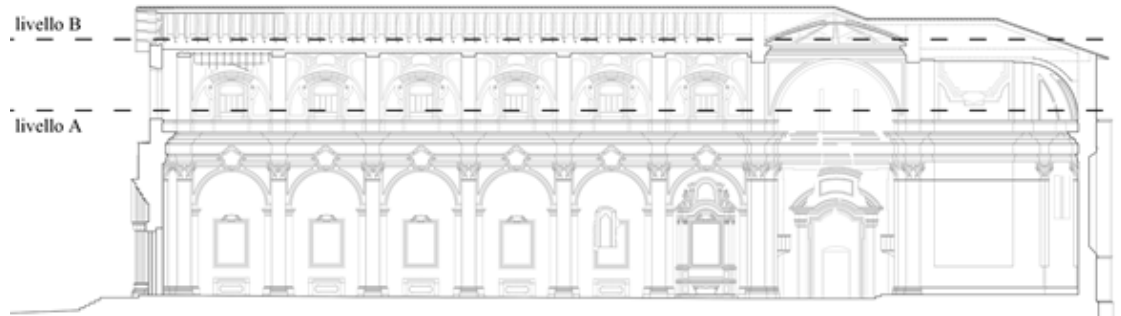
Figure 5.31: Levels of the dynamic identification sensors in the nave of San Domenico (courtesy of EXPIN).

Both uniaxial and dual-axis accelerometers for the measuring in one or two directions respectively were employed. In order to achieve high reliability of the tests, for each configuration three tests were performed and the results were averaged. The configuration of the accelerometers for the Level A is shown in Figure and of the accelerometers for the Level B is shown in Figure . In both of the figures, the location of the reference sensors is shown in red.

Figure 5.32: Sensor locations for the Level A (courtesy of EXPIN).

137

Figure 5.33: Sensor locations for the Level B (courtesy of EXPIN).

Results

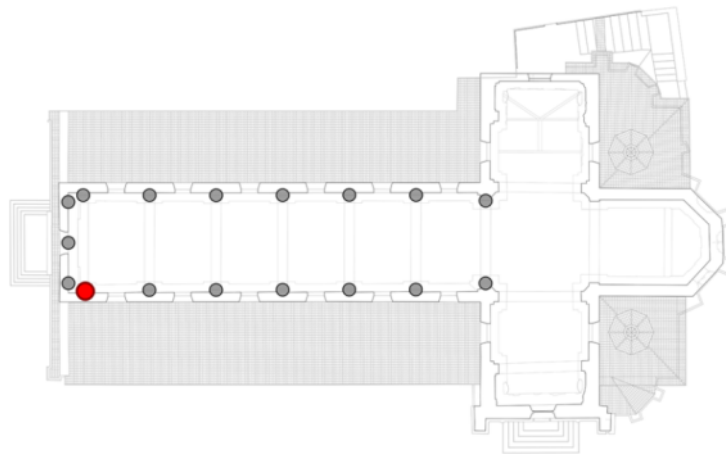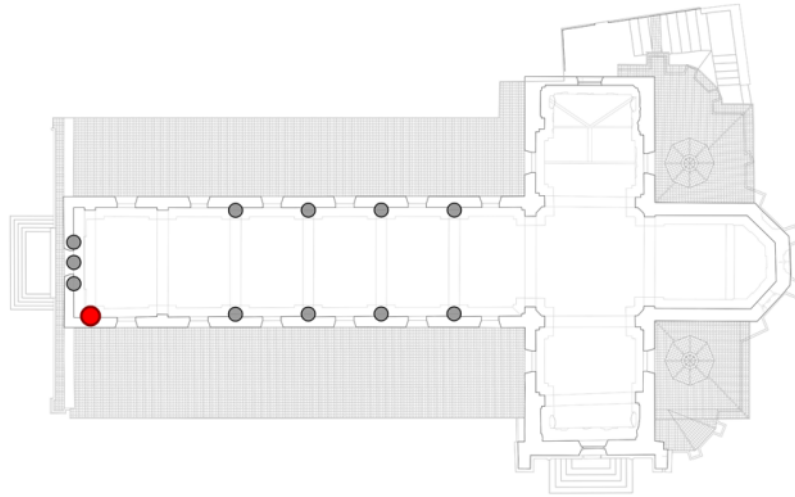Via the analysis of the results it was possible to identify the first four of five significant frequencies and to take the corresponding displacement shapes. In the two different configurations with the sensors positioned on the Level A on the east and west side, in the transverse direction, the resulted modes were different, giving for the second configuration the modes with higher frequency. This can possibly attributed to the higher stiffness on this side due to its connection with the adjacent monastery.

The out-of-plane behaviour of the façade was identified by sensors placed on it on the Level A. The analysis gave two main motion trends: a rigid rotation of the façade (Figure 5.34) and a flexural bowing of the façade (Figure 5.35). The displacement during the rigid rotation is smaller in the side which is attached to the monastery and this can also be explained by the effect of the connection between the two structures. Moreover, during the flexural bowing mechanism it is observed that the first columns move in the opposite direction from the façade.
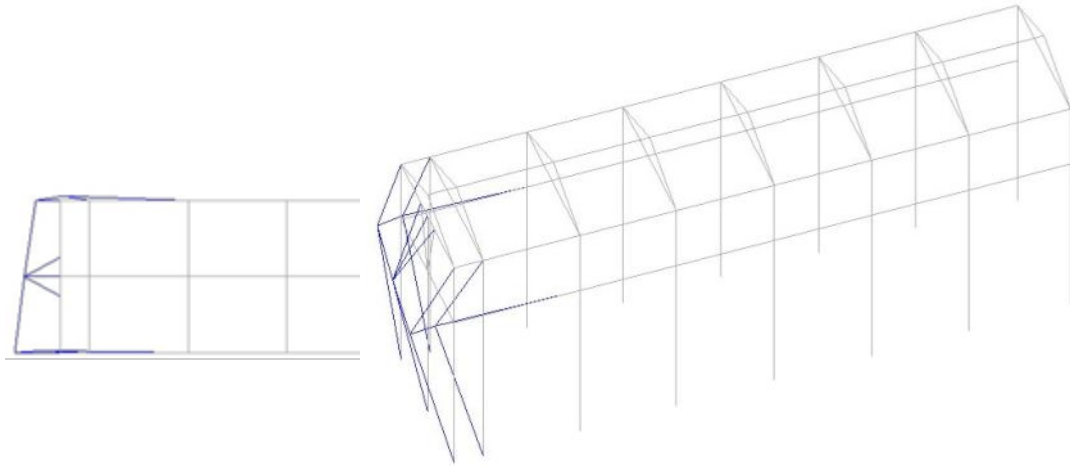
Figure 5.34: Rigid rotation of the façade (3.72Hz) and the influence of the constraint on the out-of-plane motion (courtesy of EXPIN).
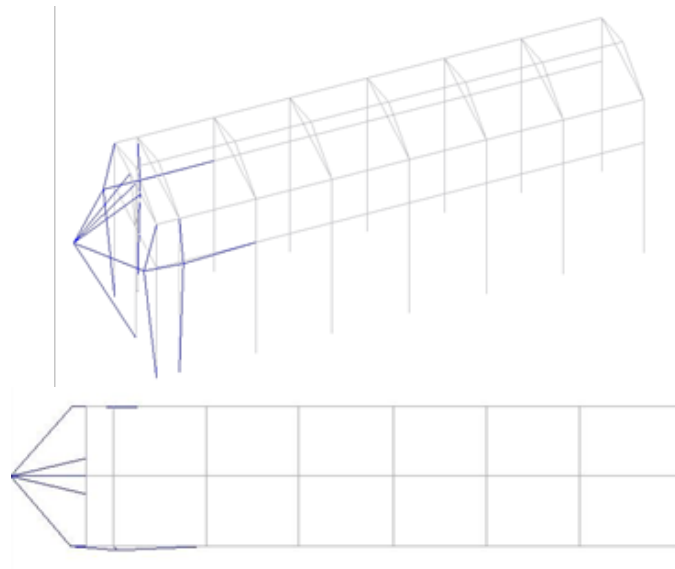
Figure 5.35: Flexural bowing of the façade (4.89Hz) and the opposing movement of the first interior columns (courtesy of EXPIN).

The opposing movement of the façade and the columns may testify the damage and the local lack of connections between the façade and the longitudinal walls. Indeed, such damages where observed during the visual inspection of the church on the upper portions of the façade (Figure 5.37).

139
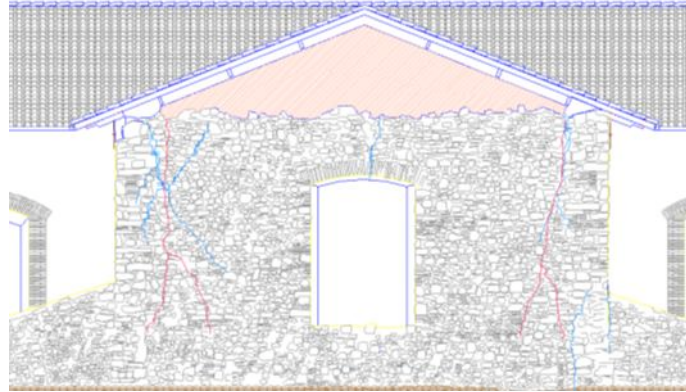
Figure 5.36: Damages corresponding to the results of rigid rotation of the façade. Crack pattern on upper part of facade (courtesy of EXPIN).

Figure 5.37: Damages corresponding to the results of the Flexural bowing of the façade. Diagonal crack on the west wall suggesting facade overturning (courtesy of EXPIN).

From a configuration with sensors on both of the sides of the nave at the Level B, at the springing of the roof, the three mode shapes showed in-phase motion while for both of the sides the fourth mode was an out-of-phase motion. One more configuration was implemented with sensors on the Level B on either side of the nave and on the upper wall part of the façade near the portion which collapsed during the earthquake. From this setup it was observed that the out-of-plane motion of the façade had much higher frequencies than the transverse motion of the nave walls. This could be due to the damage observed in the façade and its disconnection with the longitudinal walls.

Analysing all of the different sensor configurations, global movements of the façade can be identified showing that the majority of the modes corresponded to out-of-plane movement of the façade. In the lower frequencies the façade showed flexural motion and overall tilting while for slightly higher frequencies the motion was mainly focused on the main nave walls. Higher frequencies still showed further flexural motion of the upper part of the façade that is out-of-phase with the lateral portions of the nave. These findings correspond well with the damage observed in the survey of the church.

(a)   (b)
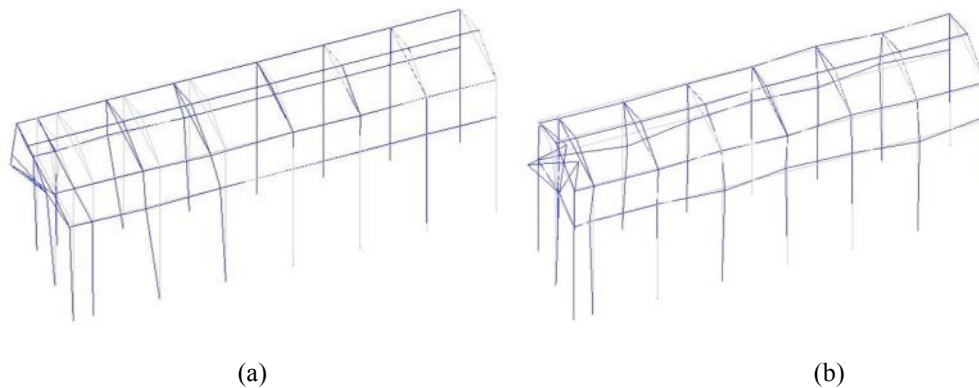
Figure 5.38: Combined modes of the central nave and façade: (a) First mode (2.64Hz) – flexure and overturning of the façade; b) Higher mode (13.33Hz) – flexural motion of the facade out-of-phase with the lateral walls (courtesy of EXPIN).

Finally, due to the fact that the magnitude of the nave wall motion was significantly lower in comparison to the motion of the façade, the configurations placed on those were considered separately from the others including the façade sensors. The analysis showed modes with low frequencies for these motions Moreover there were observed a local rotation of the nave wall close to the façade and an overall flexure of the whole nave wall (Figure 5.39). The initial hypothesis of low stiffness of global main nave bending as a primary mode were verified by the low frequency response of the nave wall in bending.

Figure 5.39 Bending of the Main Nave (2.78Hz) (courtesy of EXPIN).

141

5.6 Numerical finite element model of San Domenico church

For the needs of future structural analysis of the San Domenico church a numerical model was decided to be created and the Cast3m software was selected for this purpose. The main reason for the selection of the Cast3m was the fact that the structure consists of three leaf stone masonry walls and making possible the implementation of the numerical material behaviour parameters which occurred from the previous stage.
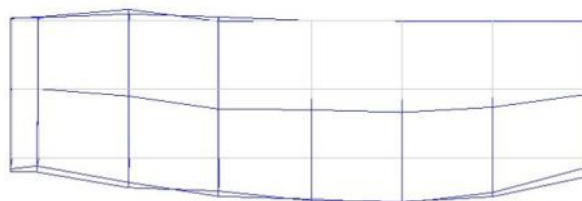
The creation geometry of the structure was done with the use of the detailed floor plans, sections and elevations along with photographic material which was available after the damage survey of the building due to the 2009 earthquake. Nevertheless, it was decided to proceed to simplifications over the geometry of the numerical model which however will not affect the results of the structural analysis.

For the creation of the geometry also the commercial software programs AutoCad (Autodesk, 2007) and GiD (CIMNE, 2007) were used in combination with some user developed applications. The numerical model of the church has volumic elements (CUB8) for the masonry and concrete parts, triangular shell elements (TRI3) for the vaults and domes and bar elements (SEG2) for the timber and concrete elements of the roof.
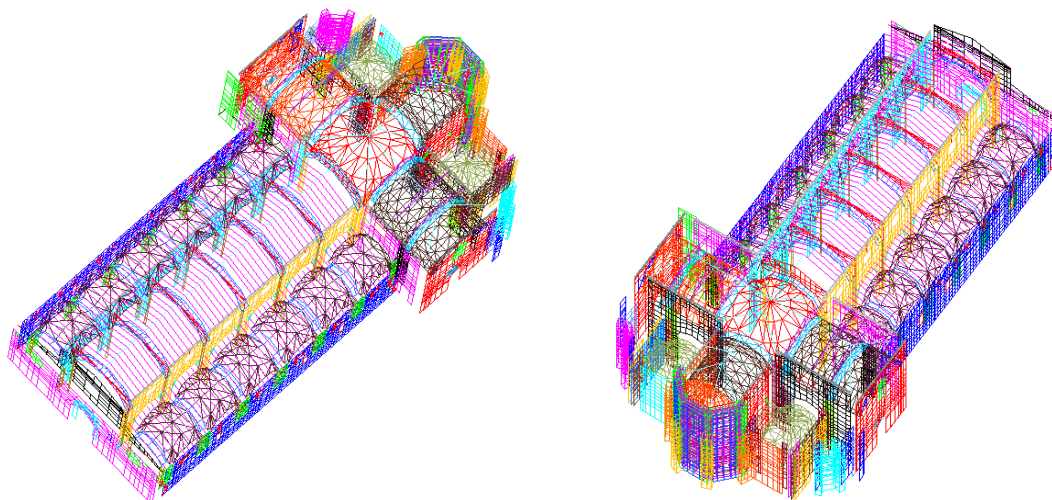

Figure 5.40: San Domenico church 3D model in AutoCad, compatibly designed for insertion in Cast3m.

142

The results non destructive (NDT) and minimum destructive tests (MDT) which are available and have already presented will be used for the further calibration of the numerical material behaviour parameters of the model. The results of the double flat jack tests can show the Young's modulus of elasticity that the masonry wall has in different areas. This value, using the experience acquired by the calibration for the experimental results can be used for further adjustment of those numerical behaviour parameters. Moreover, local stress levels that were found with the use of the single flat jack tests can be used for the verification and calibration of the numerical model during a self weight analysis. The results of the pacometer and Schmidt hammer tests are useful for the properties of the concrete beam which is located on the top of the masonry walls and of the concrete roof trusses. The sonic tomography can be used for identifying areas of the church with very deteriorated or altered properties and this can be taken into account giving modified material properties to the numerical model at the same area if this is believed to be important for the structural analysis. Finally, the results of the dynamic identification tests have highly important use in the calibration of the numerical model. The modal analysis which was the outcome of the dynamic tests can be compared with the modal analysis of the numerical model. From the comparison of the mode shapes and the frequencies it can be decided if the parameters like the stiffness of the numerical model need to be modified in some areas in order the model to behave like the real structure. Moreover, from the mode shapes occurred from the dynamic identification it is possible to identify areas with damages like loss of connection which can also be simulated in the numerical model by locally interrupting the continuous material in that part.

(a)   (b)
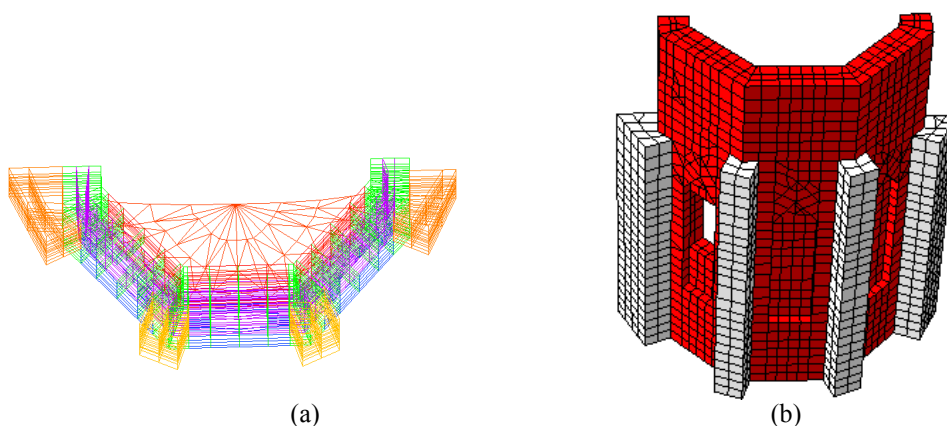
Figure 5.41: Three dimensional model of the apse in Autocad and with volumic finite elements in Cast3m.

143

(a)   (b)
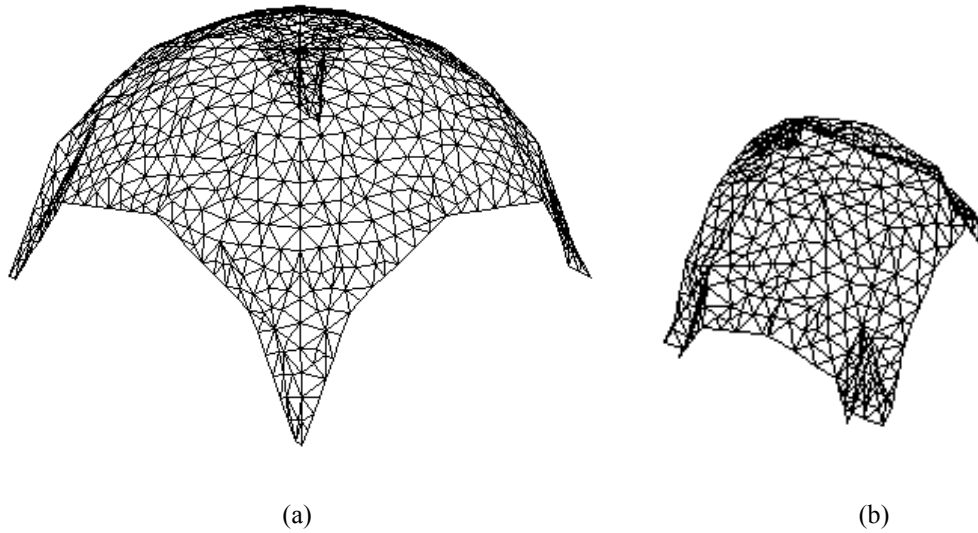
Figure 5.42: Surfaces in Cast3m with shell elements TRI3 of: (a) the main dome; (b) an aisle dome.

(a)   (b)
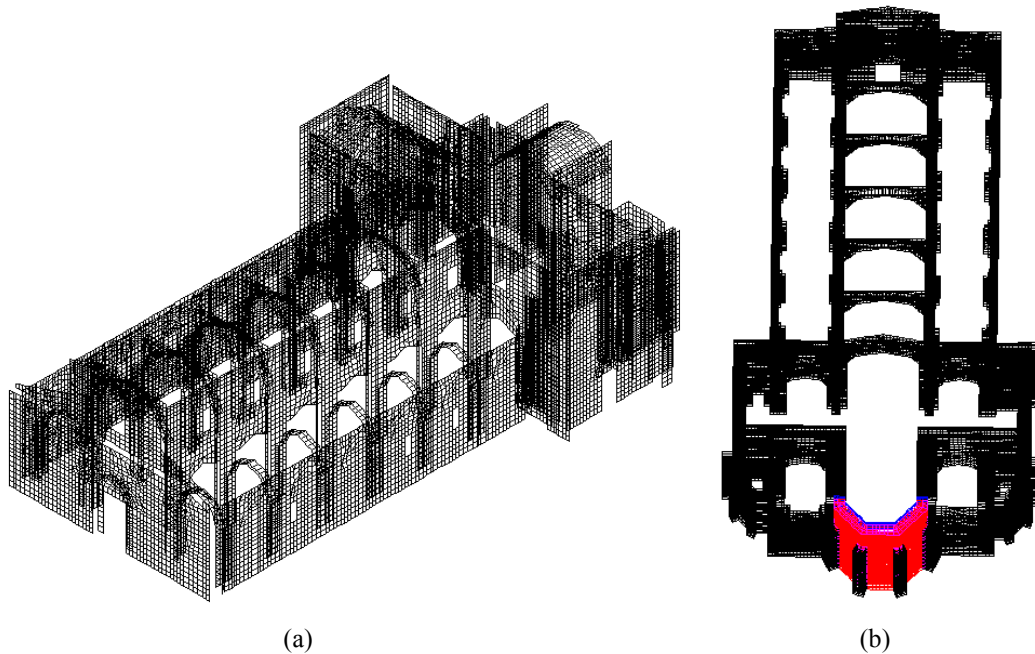
Figure 5.43: San Domenico church model in Cast3m: (a) before extruding the faces for the creation of volumic finite elements; (b) after the creation of the volumic elements, the apse is shown in red.

The numerical model that has been created, after the calibration which needs to be done as it has already been described, it can be used for the future structural analysis of the San Domenico church. A non linear time history analysis using the accelerograms of the 2009 Abruzzo earthquake is expected to be very useful results

144

for the understanding of the damages causes and of the structural deficiencies of the church. Moreover, the effect of a strengthening using lime grout injections can be studied if the numerical material behaviour parameters which occurred for the strengthened masonry walls adopted. The strengthening technique of ties can also be analysed only with minor additions in the geometry of the numerical model.

(a)   (b)
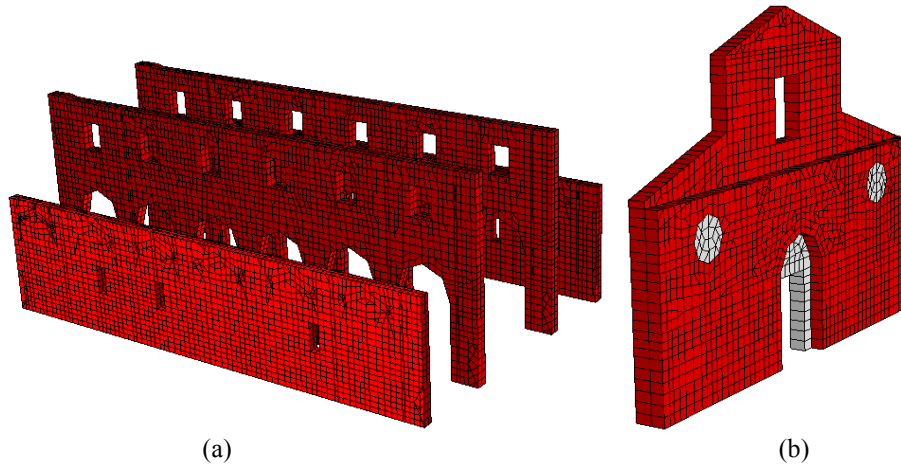
Figure 5.44: San Domenico church model in Cast3m: (a) the main nave with the two lateral aisles; (b) the main façade with main entrance.

Chapter 6

Conclusions and future works

The grout injection has proved to be a very efficient strengthening technique of multi leaf stone masonry walls. The consolidation and the binding that it creates between the internal and external leaves improve drastically the behaviour of the stone masonry walls under monotonic or cyclic loading. This has been shown also by the experimental campaign of UNIPD where three-leaf stone masonry walls were injected with natural hydraulic lime-based grouts for achieving compatibility with the traditional material. The results of the compression tests showed a different behaviour between the monotonic and cyclic compression test which was expectable. In both of the cases the total compressive strength of the injected walls was significantly higher than the unstrengthened ones approximating even an increase of 100% in some of the cases.

Based on those experimental results, numerical material behaviour curves where calibrated with the implementation of a continuous damage model. Homogeneous and isotropic material properties were assumed for the simulation of the tests. Different numerical material parameters were used for the simulation of the monotonic and cyclic tests in order to make possible the reproduction of the unloading-loading segments of the numerical material behaviour curve. For every wall typology two different behaviour curves were calibrated, one for the monotonic and one for the cyclic compression. The main difference between them is the Young's modulus of elasticity which was adopted imposing limitations in the application of those numerical material parameters regarding the type of analysis which is going to be carried out. The properties occurred from the calibration of the cyclic compression test, which can simulate well the unloading-loading behaviour but using a high Young's modulus, are applicable for use on time history analysis while the ones of the monotonic compression can be used for pushover or lateral force and modal analysis.

Regarding the simulation of the shear-compression tests, it was proved to be a more complex and demanding procedure. New numerical material behaviour parameters had to be found in order the numerical model to appear higher ductility and lower rigidity. The results of the analysis showed that the numerical model had the ability to dissipate energy during the loading cycles; however the hysteretic behaviour and energy dissipation of such a finite element model cannot fully reproduce the behaviour of the real stone masonry walls ruled in a great extent by non-linearities like the big crack opening.

Future research can be focused on the study of the masonry walls different material properties for the internal and external leaves with or without interaction between them. The interaction between the leaves can be simulated with the use of a joint which can have linear or non-linear properties. Taking into consideration the significantly higher computational cost, the worth of such a solution can be assessed.

Concerning the shear-compression tests, future research can be focused on seeking a more uniform of modifying the numerical material behaviour curves occurred from cyclic test in order the numerical model to be able to simulate satisfactorily the shear-compression tests. The modification could be linked with the compressive fracture energy and guidelines could be created on the modification of the numerical material parameters.

Moreover, the calibrated numerical material properties can be used for future analyses and reproduction of other experimental campaigns. It would be interesting to investigate the correlation of the numerical results with the damage pattern that was created during shaking table tests on similar typology scaled structures in both unstrengthened and strengthened conditions. Finally the numerical model of San Domenico church which was created can be used for a plethora of analyses with emphasis on the time history analysis using the accelerograms of the 2009 Abruzzo earthquake for a better understanding of the causes of the structural damages.

References

Acary V., Jean M. (1998). *"Numerical simulation of monuments by the contact dynamics method"*. Monument 98, Workshop on Seismic Performance of Monuments, LNEC, Lisboa, Portugal.

Adami C.E, (2011), "Πειραματική και αναλυτική διερεύνηση της συμπεριφοράς διεπιφανειών υδραυλικών ενεμάτων υψηλής διεισδυτικότητας και λίθινων ή πλίνθινων υποβάθρων", Phd Thesis, National Technological Institut of Athens, Greece. In Greek.

Alexandris, A. , Protopapa, E. and Psycharis, I. (2004) *"Collapse mechanisms of masonry buildings derived by the distinct element method"*. Proceedings of the 13th World Conference on Earthquake Engineering Vancouver — paper no. 548

Antonini O (2010), *"Architettura religiosa aquilana"*, Todi (Pg), Tau Editrice, In Italian

Azevedo J., Sincraian G. (2001). *"Modelling the Seismic Behaviour of Monumental Masonry Structures"*. Proceedings of the International Congress Archi2000, UNESCO,Bethlehem,Palestine

Baggio C., Trovalusci P. (1995). *"Stone assemblies under in-plane actions comparison between nonlinear discrete approaches"*. Computation Methods in Structural Masonry, Vol. 3, pp. 184-193.

Bazant Z.P., Oh B. (1983) *"Crack band theory for fracture of concrete"*. RILEM Materials and Structures,16, pp.155–177.

Berto L., Scotta R., Vitaliani R. Saetta, A. (2001). "*An orthotropic damage model for non-linear masonry walls analysis. Irreversible strain and friction effects"*. Historical Constructions, Guimarães, Portugal.

Bettio, C., Gelmi, A., Modena, C. and Rossi, P. P. (1993). *"Caratterizzazione meccanica e consolidamento statico delle murature dei centri abitati di antica origine della provincia di trento"*. In Murature, Sicurezza e Recupero, Trento, 154–184. In Italian.

148

Bicanic N., Ponniah D., Robinson J. (2001). *"Discontinuous deformation analysis of masonry bridges"*. Computational Modelling of Masonry, Brickwork and Blockwork Structures. Saxe-Coburg Publications, Stirling, UK, pp. 177-196.

Binda L, Tiraboschi C. (1999), *"Flat-jack test as a slightly destructive technique for the diagnosis of brick and stone masonry structures"*. Eighth International Conference and Exhibition, Structural faults and repair, Vol. 5, pp. 449–72, London (U.K).

Binda, L., Pina-Henriques, J., Anzani, A., Fontana, A. and Lourenço, P. (2006). *"A contribution for the understanding of load-transfer mechanisms in multi-leaf masonry walls: Testing and modelling"*. Engineering Structures, 28(8), 1132–1148.

Binda L., Cantini L., Cardani G., Saisi A., Tirabosch C., (2007), *"Use of flat jack and sonic tests for the qualification of historic masonry"*, The tenth North American masonry conference, St.Louis, Missouri (U.S.A.).

Block P. (2005). Equilibrium systems. Studies in masonry structure, MS dissertation, Department of Architecture, Massachusetts Institute of Technology.

Block P., Ciblac T., Ochsendorf J.A. (2006). *"Real-time limit analysis of vaulted masonry buildings"*. Computers and Structures, Vol. 84, pp.1841-1852.

Borri A., Avorio A., Cangi G. (1999a). *"Considerazioni sui cinematismi di collasso osservati per edifici in muratura"*. IX Convegno Nazionale "L'ingegneria Sismica in Italia", ANIDIS, Torino, Italy.

Borri A., Avorio A., Cangi G. (1999b). *"Riparazione e consolidamento degli edifici in muratura"*. Regione dell'Umbria, F. Gurrieri, Manuale per la riabilitazione e la ricostruzione postsismica degli edifici, DEI Tipografia del Genio Civile: Rome, Italy.

Braga F., Dolce M. (1982). *"Un metodo per l'analisi di edifici multipiano in muratura antisismici."* VI I.B.Ma.C., Roma, pp.1088-1099. In Italian

Braga F., Liberatore D. (1990). *"A finite element for the analysis of the response of masonry buildings"*. V North American masonry conference, Urbana, pp. 201-212.

Brencich A., Gambarotta G., Lagomarsino S., (1998). *"A macroelement approach to the three-dimensional seismic analysis of masonry buildings"*. XI European Conference on Earthquake Engineering, Paris, p. 602.

149

Caboche J. L, *"Continuum damage mechanics: Part I and II "*, J. of Appl. Mech., Trans. of the ASME, Vol. 55, Vol. 55, pp. 59-72, (1988)

Caleca L., De Vecchi A. (1990). *"Tecnologie di consolidamento delle strutture murarie"*, Ed. Flaccovio.

Casarin F. (2006), '*Structural assessment and aeismic vulnerability analysis of a complex historical building'*, Ph. Thesis, University of Trento (Italy)

Casolo S. (2004a). *"Macroscopic Modeling of structured materials: relationship between orthotropic Cosserat continuum and rigid elements"*. International Journal of Solids and Structures. Vol. 43, No. 3, pp. 475-496.

Casolo S. (2004b). *"Modeling in-plane micro-structure of masonry walls by rigid elements"*. International Journal of Solids and Structures, Vol. 41, No. 13.

Casolo S., Peña F. (2007). *"Rigid element model for in-plane dynamics of masonry walls considering hysteretic behavior and damage"*. Earthquake Engineering and Structural Dynamics, pp. 1029-1048.

Cervera M. , Pelá L., Clemente R., Roca P. (2010a), *"A crack-tracking technique for localized damage in quasi-brittle materials"*, Engineering Fracture Mechanics, 77, pp. 2431–2450

Cervera, M. , Chiumenti, M., Codina, R. (2010b*). "Mixed stabilized finite element methods in nonlinear solid mechanics. Part I: Formulation*", Computer methods in applied mechanics and engineering, 199, pp. 2559–2570

Cervera, M. , Chiumenti, M., Codina, R. (2010c*). "Mixed stabilized finite element methods in nonlinear solid mechanics. Part II: Strain localization*", Computer methods in applied mechanics and engineering, 199, pp. 2571–2589

Clemente R., Roca P., Cervera M. (2006). '*Damage model with crack localization - Application to historical buildings*". Structural V International Seminar on Structural analysis of historical constructions - SAHC06, New Delhi, India, pp 1125-1135.

Collepardi M. (1991). *"Scienza e tecnologia del calcestruzzo"*, Hoepli, Milano. In Italian

Collepardi M., Coppola L. (1991). *"Il risanamento degli edifici storici: situazione attuale e prospettive nella ricerca"*. L'Edilizia 9/9137-548. In Italian

Corradi, M., Borri, A. and Vignoli, A. (2003). *"Experimental study on the determination of strength of masonry walls"*. Construction and Building Materials, 17(5), 325–337.

Corradi, M., Tedeschi, C., Binda, L. and Borri, A. (2008). "*Experimental evaluation of shear and compression strength of masonry wall before and after reinforcement: Deep repointing*". Construction and Building Materials, 22(4), 463–472.

Croci G. (1995). "*The Colosseum: safety evaluation and preliminary criteria of intervention*". International Seminar on Structural Analysis of Historical Constructions - SAHC, Barcelona, Spain.

Croci G., Cerone M., Viskovic A. (1997). "*Analysis from a historical and structural point of view of the domes of Pantheon. Hagia Sophia and St Peter studies in ancient structures*". YTU Faculty of Architecture Publication, Istanbul, Turkey.

Cundall P.A., Hart P. (1971). "*A computer model for simulating progressive large scale movements in blocky rock systems"*. Symposium on Rock Fracture - ISRM, Nancy, France, Vol 1, No. II-8.

D'Asdia P., Viskovic A. (1994). "*L'analisi sismica degli elementi in muratura. Ingegneria sismica*", Anno XI, No. 1, pp. 32-42. In Italian.

D'Ayala D., Speranza E. (2002a). *"An integrated procedure for the assessment of seismic vulnerability of historic buildings"*. XII European Conference on Earthquake Engineering, paper no. 561.

D'Ayala D., Speranza E. (2002b). *"Definition of collapse mechanisms and seismic vulnerability of masonry structures"*. Earthquake Spectra, Vol. 19, No. 3, pp. 479–509.

da Porto, F. 2000. "*Indagini sperimentali sull'efficacia di tecniche di consolidamento di murature storiche in pietra*". Graduation thesis, Rel. Prof. C. Modena, Università degli Studi di Padova. In Italian

de Borst, R., Remmers, J. J, Needleman, A. y Abellan, M. A. (2004), "Discrete vs smeared crack models for concrete fracture: bridging the gap", International journal for numerical and analytical methods in geomechanics., vol. 28, pp. 583–607

de Luca A., Giordano A., Mele E. (2004). "*A simplified procedure for assessing the seismic capacity of masonry arches*". Engineering structures, Vol. 26, pp. 1915–1929.

151

Doglioni F., Moretti A., Petrini V. (1994). *"Le chiese ed il terremoto"*, LINT, Trieste, Italy. In Italian

Egermann, R. (1991). *"Experimental analysis of multiple leaf masonry wallets under vertical loading"*. Proccedings of the 2nd structural, repair and maintenance of historical buildings II, Spain, 197-208.

Egermann, R. (1993). *"Edifici in muratura in pietra: ricerca e applicazioni all'Università di Karlsruh"*. In Murature Sicurezza Recupero. Trento, 70–95. In Italian.

Fajfar P. (1999). *"Capacity spectrum method based on inelastic demand spectra"*. Earthquake Engineering and Structural Dynamics, Vol. 28, pp. 979-993

Faria R., Oliver X. (1993), *"A rate dependent plastic-damage constitutive model for large scale* computation in *concrete structures"*, Monografia CIMNE, n. 17, Barcelona, Spain.

Faria, R., Oliver, J. Cervera, M. (1998). *"A strain-based viscous-plastic-damage model for massive concrete structures"*, International journal of solids and structures, 35, pp. 1533-1558.

Galasco, A., Penna, A. and Magenes, G. (2009a). *"Caratterzzazione meccanica di muratura in pietra. parte prima: prove di compressione semplice e di compression diagonale"*. Technical report, Università degli Studi di Pavia. Allegato 4.2-UR01-1, in Italian.

Galasco, A., Penna, A. and Magenes, G. (2009b). *"Caratterzzazione meccanica di muratura in pietra. parte seconda: prove cicliche di taglio-compressione su pannelli di grandi dimensioni"*. Technical report, Università degli Studi di Pavia. Allegato 4.2-UR01-2, in Italian.

Gambarotta L, Lagomarsino S. (1997). *"Damage models for the seismic response of brick masonry shear walls. Part I: The mortar joint model and its applications"*. Earthquake Engineering and Structural Dynamics, Vol. 26, pp. 423-439.

Gentile C., Saisi A. (2006), *"Ambient vibration testing of historic masonry towers for structural identification and damage assessment"*, Construction and Building Materials, Vol. 21, pp. 1311–1321.

Giuffrè A. (1991). *"Lettura sulla meccanica delle murature storiche"*. Kappa, Roma. In Italian

Giuffrè A. (1993a). *"Sicurezza e conservazione dei centri storici in area sismica, il caso Ortigia"*. Laterza, Bari, Italy. In Italian

Giuffrè A., Carocci C (1993b). *Statica e dinamica delle costruzioni murarie storiche. Atti del Convegno internazionale CNR "Le pietre da costruzione: il tufo calcareo e la pietra leccese"*. Mario Adda Editore, Bari, pp 539–598. In Italian

Giuffrè A., Pagnoni T., Tocci C. (1994). *"In-plane seismic behaviour of historical masonry walls"*. X International Brick and Block Masonry Conference, Calgary, Canada.

Giuffrè A. (1995). *"Vulnerability of historical cities in seismic areas and conservation criteria"*. Congresso "Terremoti e civiltà abitative", Annali di Geofisica, Bologna.

Giuffrè A., Carocci C. (1996). *"Vulnerability and mitigation in historical centres in seismic areas"*. Criteria for the formulation of a Practice Code. XI World Conference on Earthquake Engineering, Acapulco, paper n. 2086.

Gregorczyk P., Lourenço P., (2000) . *"A review on flat jack testing"*, University of Minho (Portugal), Department of Civil Engineering, pp. 39-50.

Hillerborg A, Modeer M, Petersson PE. (1976). *"Analysis of crack formation and crack growth in concrete by means of fracture mechanics and finite elements"*. Cement and Concrete Research 6, pp. 773–782.

Jean M. (1995). *"Frictional contact in collections of rigid or deformable bodies: numerical simulation of geometrical motions"*. Mechanicals of Geomaterial Interfaces, pp. 463-486.

Kupfer H., Hilsdorf H., and Rusch H. (1969), *"Behaviour of concrete under biaxial stresses"*, Journal of the American Concrete Institute, 66 (8), pp. 656-666

La Borderie C., Berthaud Y., Pijaudier-Cabot G. (1990), *"Crack closure effects in continuum damage mechanics - Numerical implementation"*, Proc. of 2nd Int. Conf. on Comp. Aided Analysis and Design of Concrete Struct., Zell amm See, Austria, pp. 975-986

Lagomarsino S., (1998)," *Damage survey of ancient churches: the Umbria-Marche experience"*, Seismic Damage to Masonry Buildings: Proceedings of the International Workshop, Padova (Italy).

Lagomarsino S. (2006). *"On the vulnerability assessment of monumental buildings"*. Earthquake Engineering, Vol. 4, pp. 445-463. European Commission, Brussels.

Lourenço P. B. (1996). Computational strategies for masonry structures. Delft University of Technology.

Lemos J.V. (1995). *"Assessment of the ultimate load of a masonry arch using discrete elements"*. Computer Methods in Structural Masonry, pp. 294–302.

Lemos J.V. (1998). *"Discrete element modeling of the seismic behavior of stone masonry arches"*. Computer methods in structural masonry, London, pp 220–227.

Macchi G., Ruggeri M., Eusebio M., Moncecchi M. (1993).*" Structural assessment of the leaning tower of Pisa"*. Structural preservation of the architectural heritage, IABSE, Zürich, Switzerland, pp. 401–408.

Mazars J., Pijaudier-Cabot G. (1989), *"Continuum damage theory - Application to concrete"*, J. of Eng. Mech., ASCE, Vol. 115, n. 2, pp. 345-365

Mazzon, N., (2010), *"Influence of Grout Injection on the Dynamic Behaviour of Stone Masonry Buildings"*. Ph.D thesis, Sup. Prof.ssa Valluzzi, M.R., University of Padua.

Modena C., Valluzzi M.R., da Porto F., Casarin F. (2011): *"Structural aspects of the conservation of historic masonry constructions in seismic areas: remedial measures and emergency actions"*, IJCH International Journal of Architectural Heritage, Vol. 5, Issue 4-5, July 2011. Special Issue: In Honor of Professor Luigia Binda and Over 25 Years of Masonry Research and Education, pp. 539-558.

Modena, C. and Bettio, C. (1994). *"Experimental characterisation and modelling of injected and jacketed masonry walls"*. In Proceedings of Italian-French Symposium Strengthening and Repair of Structures in Seismic Area, Nizza, France, 273–282.

Molins C., Roca P. (1998). *"Capacity of masonry arches and spatial frames"*. Journal of Structural Engineering, Vol. 124, No. 6, pp. 653-663.

Ngo D, Scordelis AC. (1967)*"Finite element analysis of reinforced concrete beams"*. Journal of the American Concrete Institute, Vol.64, pp.152–163.

Oliveira, D. V. and Lourenço, P. B. (2006). *"Experimental behaviour of three-leaf stone masonry walls"*. In The construction aspects of built heritage protection, Dubrovnik, Croatia, 356–362.

Oliver J., Cervera M., Oller S., Lubliner J. (1990) *"Isotropic damage models and smeared cracked analysis of concrete"*, Proc. 2nd ICCAADS, vol. 2, pp. 945-958, Zee Am See, Pineridge Press

Orduña A., Lourenço P.B. (2001). *"Limit Analysis as a tool for the simplified assessment of ancient masonry structures"*. International Conference on Structural Analysis of Historical Constructions - SAHC01, Guimarães, Portugal, 7-9 November, pp. 511-520.

Orduña A., Lourenço P.B. (2003). *"Cap Model for Limit Analysis and Strengthening of Masonry Structures"*. Journal of structural engineering, Vol. 129, No. 10, pp. 1287-1430.

Orduña A., Lourenço P.B., (2005a). *"Three-dimensional limit analysis of rigid blocks assemblages. Part I: Torsion failure on frictional joints and limit analysis formulation"*. International Journal of Solids and Structures, Vol. 42, No. 18-19, pp. 5140-5160.

Orduña A., Lourenço P.B., (2005b). *"Three-dimensional limit analysis of rigid blocks assemblages. Part II: Load-path following solution procedure and validation."* International Journal of Solids and Structures, Vol. 42, No. 18-19, pp. 5161-5180.

Ochsendorf J. A. (2002). Collapse of masonry structures. University of Cambridge, Ph.D. Thesis.

Pagnoni T. (1994). *"Seismic analysis of masonry and block structures with the discrete element method"*. X European conference on earthquake engineering, Vol. 3, pp. 1674–169.

Pagnoni T., Vanzi I. (1995). *"Experimental and numerical study of the seismic response of block structures"*. Computer methods in structural masonry, pp. 213–222.

Papastamatiou D., Psycharis I. (1993). *"Seismic response of classical monuments-a numerical perspective developed at the Temple of Apollo Bassae, Greece"*. Terra Nova, No. 5, pp. 591–601.

Pelá L., Cervera M., Roca P., Benedetti A. (2008). *"An orthotropic damage model for the analysis of masonry structures"*. VIII International Seminar on Structural Masonry - ISSM 08, pp. 175–178.

155

Pelá L., Aprile A., Benedetti A. (2009). *"Seismic assessment of masonry arch bridges"*. Engineering Structures, Vol. 31, No. 8, pp. 1777-1788.

Pisano, F. (1999). Validità di modelli fisici nello studio della tecnica di iniezione di murature storiche a tre paramenti. Master's thesis, Politecnico di Milano. In Italian.

Potter C., Ademovic N., Manning E. (2011), *"Integrated Approach for the Characterization and Analysis of San Domenico Church in L'Aquila",* SA7 project of SAHC master program, University of Padova, Italy

Psycharis I., Lemos J.V., Papastamatiou D., Zambas C., Papantonopoulos C. (2003). *"Numerical study of the seismic behaviour of a part of the Partenón Pronaos"*. Earthquake Engineering & Structural Dynamics, Vol. 32, No. 13, pp. 2063–2084.

Rashid YR.(1968) " *Analysis of reinforced concrete pressure vessels*". Nuclear Engineering and Design 1968; Vol.7, pp.334–344.

Roca P., Molins C., Marí A.R. (2005). *"Strength capacity of masonry wall structures by the equivalent frame method"*. Journal of Structural Engineering, Vol. 131, No. 10, pp. 1601-1610.

Roca P., López-Almansa F., Miquel J, Hanganu A. (2007*). "Limit analysis of reinforced masonry vaults"*. Engineering Structures, Vol. 29, No. 3, pp. 431-439.

Rots J.G. (1992), "*Removal of finite elements* in smeared crack analysis". In Proc. Third Int. Conf. Computational Plasticity, Pineridge Press, Swansea,

Saetta A., Scotta R., Vitaliani R. (2000). *"An orthotropic fourth-rank damage model for masonry structures"*. European Congress on Computational Methods in Applied Sciences an Engineering - ECOMAS 2000, Barcelona, Spain.

Silva B., (2008a). Aplicação de um modelo de dano contínuo na modelação de estruturas de alvenaria de pedra. igreja de gondar - um caso de estudo. MSc Thesis, Faculdade de Engenharia da Universidade do Porto, Porto, Portugal. In Portuguse

Silva B., Costa A. A., Guedes J., Arêde A., Costa A. (2008b). *"In-Plane behavior of a stone masonry pier: Experimental test, numerical simulation and retrofitting efficiency evaluation"*. International seminar on seismic risk and rehabilitation of stone masonry housing, Azores, Portugal.

156

Simo J. C. and Ju J. W. (1987), *"Strain and stress based continuum damage models - part I: formulation"*, International journal of solids and structures, 23, n. 7, pp. 821-840

Sincraian G.E. (2001). Seismic behaviour of blocky masonry structures. A discrete element method approach. Ph.D. Dissertation, IST, Lisbon, Portugal

Stylianidis K., Sextos A. (2009). *"Back analysis of Thessaloniki Byzantine land walls as means to assess its seismic history",* International journal of architectural heritage, 3(4), pp.1-23.

Tomaževic M. (1978). The computer program POR. Report ZRMK.

Tomaževic M., Sheppard P. (1982). *"The strengthening of stone-masonry buildings for revitalization in seismic regions"*. Proceedings of the 7th European conference on earthquake engineering, Athens, vol. 5,. pp. 275–82.

Tomaževic M., Weiss P. (1990). *"A rational, experimentally based method for the verification of earthquake resistance of masonry buildings"*. IV U.S. National Conference on Earthquake Engineering, Palm Springs, Vol. 2, pp. 349-359.

Tomaževic M. (1992). *"Laboratory and in-situ tests of the efficacy of grouting and tying of stone masonry walls"*. In International workshop on the Effectiveness of injection techniques for retrofitting of stone and brick masonry walls in seismic areas, Politecnico di Milano, 95–116.

Toumbakari, E. E. and van Gemert, D. (1997). *"Lime pozzolana cement injection grouts for the repair and strengthening of three leaf masonry structures"*. In Proceedings of 4th International conference on the conservation of monuments in the Mediterranean Basin, Rodhes, Greece, 385–394

Toumbakari, E. E. (2002). Lime-pozzolan-cement grouts and their structural effects on composite masonry walls. Ph.D. thesis, Katholieke Universiteit Leuven.

Valluzzi, M. R. (2000). *"Comportamento meccanico di murature consolidate con materiali e tecniche a base base di calce"*. Ph.D. thesis, Università degli Studi di Padova. In Italian.

Valluzzi, M. R., da Porto, F., Modena, C. (2001). *"Behaviour of multi-leaf stone masonry walls strengthened by different intervention techniques"*. Historical Constructions, Guimarães, Portugal 1023-1032.

157

Vintzileou, E. and Tassios, T. P. (1995). "*Three-leaf stone masonry strengthened by injecting cement grouts*". Journal of Structural Engineering, 121(5), 848–856.

Vintzileou, E. (2007). *"Grouting of three-leaf masonry: experimental results and prediction of mechanical properties"*. In evoluzione nella sperimentazione per le costruzioni, Cyprus, CD–ROM.

Vintzileou, E. and Miltiadou-Fezans, A. (2008). *"Mechanical properties of three-leaf stone masonry grouted with ternary or hydraulic lime-based grouts"*. Engineering Structures, 30(8), 2265–2276. Seismic reliability, analysis and protection of historic buildings and heritage sites.

Modello A-DC PCM-DPC MiBAC (2006), Ministero per i beni e le attivitá culturali d' Italia.

Istruzioni per l'applicazione delle "Nuove norme tecniche per le costruzioni", Ministero delle Infrastrutture e dei Trasporti, Gazzetta Ufficiale n. 47, Ordinario n.27, (26 February 2009).

Standards

ASTM 1991a: ASTM C 1196 (1991), "Standard test method for in-situ compressive stress within solid unit masonry estimated using the flat-jack method", (U.S.A.).

ASTM 1991b: ASTM C 1197 (1991), "Standard test method for in-situ measurement of masonry deformability properties using the flat jack method", (U.S.A.).

ASTM C939 (2010), "Standard Test Method for Flow of Grout for Preplaced-Aggregate Concrete (Flow Cone Method)", (U.S.A.).

ASTM C940 (2010), "Standard Test Method for Expansion and Bleeding of Freshly Mixed Grouts for Preplaced-Aggregate Concrete in the Laboratory", (U.S.A.).

ASTM C805 / C805M (2008), "Standard Test Method for Rebound Number of Hardened Concrete", (U.S.A.).

ASTM C 1196-91 (1991), "In-situ compressive stress within solid unit masonry estimated using flat-jack measurements", (U.S.A.).

ASTM C 1197-91 (1991), In-situ measurement of masonry deformability properties using flat-jack method", (U.S.A.).

CIRCOLARE (2009), n. 617 "Istruzioni per l'applicazione delle 'Nuove Norme Tecniche per le Costruzioni' di cui al decreto ministeriale 14 gennaio 2008". (GU n. 47 del 26-2-2009 - Suppl. Ordinario n.27). In Italian.

DELIVERABLE D11.1 (2004). "Tecnical guidelines for an appropriate use of the suggested equipment", ONSITEFORMASONRY, Project n° EVK4-2001-00091, Contract n° EVK4-CT-2001-00060, August 2004.

EMS (1998), European Macroseismic Scale, European seismological commission, (Luxemburg).

FIB 17 (2002), "*Management, maintenance and strengthening of concrete structures",* Technical report prepared by former FIP Commission 10.

PCM, Presidenza del Consiglio dei Ministri (2005), Ulteriori modifiche ed integrazioni all'Ordinanza n .3274 del 20/3/2003, recante "Primi elementi in materia di criteri generali per la classificazione sismica del territorio nazionale e di normative tecniche per le costruzioni in zona sismica". OPCM, n. 3431, 3 May 2005. Official Bulletin No. 107, 10 May 2005. In Italian

RILEM 1990a: RILEM Lum 90/2 Lum D.2 (1990) – In-situ stress based on the flat jack.

RILEM 1990b: RILEM Lum 90/2 Lum D3 (1990) - In-situ strength and elasticity tests based on the flat jack.